POLITECNICO DI TORINO

Master of Science in Mechanical Engineering

Department of Mechanical and Aerospace Engineering

Master's Degree Thesis

Development of a Pressure Sensitive Paint (PSP) Measurement Technique for High-Speed Turbine Testing

Supervisors

Politecnico di Torino
Prof. Daniela MISUL
Prof. Simone SALVADORI

Politecnico di Milano
Prof. Paolo GAETANI

Von Karman Institute for Fluid Dynamics
Prof. Sergio LAVAGNOLI
Ph.D. Gustavo LOPES

Candidate:
Giorgio SCALA

December 2021

Abstract

In the recent years, aircraft engine manufacturers have set ambitious goals concerning the maximization of efficiency and the reduction of noise and fuel consumption. The design of the next-generation propulsion units plays a key role in addressing this challenge. The development of innovative and green engine architectures introduces challenging operating conditions for the low-pressure turbine such as transonic Mach and low-Reynolds numbers. In the frame of the EU-funded project SPLEEN commissioned by Safran Aircraft Engines, aimed at investigating the combined effect of secondary and leakage flows under modern engine-scaled flow conditions, the development of an advanced technique of surface pressure measurement applied in the linear cascade of the S-1/C wind tunnel at the von Karman Institute is of major importance for understanding the aerodynamic performance. Based on the oxygen quenching kinematics of luminescence, the optical measurement technique of Pressure Sensitive Paint aims at measuring the 2D surface pressure field on complex geometries, offering incredible advantages in terms of non-intrusivity, high spatial resolution and low application costs compared to conventional measurement techniques. Nevertheless, the technique presents high complexity in the design and preparation of the setup, measurement testing and data-processing. The scope of the work, is the development of the measurement chain for the implementation of PSP in the S-1/C facility. In particular, the main objective of the thesis is the optimization of the setup for the achievement of the final calibration curve which relates the acquired images by a photodetector to a 2D steady-state static pressure distribution over the model surface. The reduction of the final uncertainty in the calibration parameters, which is directly related to the measurement uncertainty, goes through a detailed attention of the setup design for the implementation in the turbine test rig, the realization of the calibration setup, the development of various experimental tests including data-processing and evaluation of results for each intermediate analysis.

Acknowledgments

The experience I had working at the von Karman Institute in collaboration with Politecnico di Torino has been an opportunity for my personal and professional growth. Living every day in an international and prestigious environment such as the VKI, I have never stopped learning new things applying the deep knowledge Politecnico di Torino provided me on an experimental thesis. Before proceeding with my work, I would like to dedicate a few words to all those who have been of help to me during these months.

First of all, I would like to thank deeply my supervisor at VKI, Professor Sergio Lavagnoli, who gave me the opportunity to work in a stimulating project and guided me throughout the development of the thesis. I learned from him the importance of planning the actions necessary to achieve an objective, the attention to detail and investigate things from a critical point of view. I am also extremely thankful to my co-supervisor at VKI, PhD Gustavo Lopes, who has constantly supported me during the whole project, providing me tips and corrections that increased my curiosity and motivation. He helped me for the preparation and realization of the experiments, thanks to his deep knowledge in the turbomachinery field. I want to express my gratitude to PhD Loris Simonassi, PhD Federico Maria la Torre, PhD Mizuki Okada, PhD Lorenzo Da Valle and PhD Tommaso Carlesi and the research engineers who were essential for the preparation of the experimental setups.

Special thanks to my supervisors at Politecnico di Torino, Professor Daniela Misul and Professor Simone Salvadori, who accepted with pleasure the responsibility of putting me in contact with VKI at first and gladly followed me throughout the project despite the distance. I thank my co-supervisor at Politecnico di Milano, Professor Paolo Gaetani, he accepted with enthusiasm to collaborate with Alta Scuola Politecnica within the Double Degree Program.

My gratitude also goes to Andrea, Gianclaudio, Jorge, Mariana, Berke, Nicola, Davide and all the STP students at VKI with whom I spent an unforgettable experience during these six months in Belgium and made me feel at home.

Finally, a heartfelt thanks to my family who has supported me in every moment of my academic career.

Contents

List of symbols and units

Dimensional Quantities

h	Planck constant (6.626×10^{-34})	$[\mathrm{J\,s}]$
ν	Frequency of excitation light	$[1/\mathrm{s}]$
ν_f	Frequency of fluorescent emission	$[1/\mathrm{s}]$
ν_p	Frequency of phosphorescent emission	$[1/\mathrm{s}]$
ν_l	Frequency of luminescent emission	$[1/\mathrm{s}]$
k_{S_1}	Rate constant of excitation	$[1/\mathrm{s}]$
k_f	Rate constant for fluorescence	$[1/\mathrm{s}]$
k_p	Rate constant for phosphorescence	$[1/\mathrm{s}]$
k_{ic}	Rate constant for the internal conversion	$[1/\mathrm{s}]$
k_{isc}	Rate constant for the intersystem crossing	$[1/\mathrm{s}]$
k_r	Rate constant for radiative processes	$[1/\mathrm{s}]$
k_{nr}	Rate constant for non-radiative processes	$[1/\mathrm{s}]$
k_q	Rate constant for oxygen quenching	$[\mathrm{m}^3/(\mathrm{mol\,s})]$
$[O_2]$	Unexcited oxygen population	$[\mathrm{mol}/\mathrm{m}^3]$
$[O_2^*]$	Excited oxygen population	$[\mathrm{mol}/\mathrm{m}^3]$
I_a	Rate of excitation	$[1/\mathrm{s}]$
I	Rate of luminescence	$[1/\mathrm{s}]$
I_0	Rate of excitation without quenching	$[1/\mathrm{s}]$
τ	Luminescent lifetime	$[\mathrm{s}]$
τ_0	Luminescent lifetime without quenching	$[\mathrm{s}]$
E_{nr}	Activation energy for non-radiative processes	$[\mathrm{J}/\mathrm{mol}]$
E_D	Activation energy for oxygen diffusion process	$[\mathrm{J}/\mathrm{mol}]$
R	Universal gas constant (8.315)	$[\mathrm{J}/\mathrm{K\,mol}]$
R_{AB}	Interaction distance luminophore-oxygen	$[\mathrm{m}]$
N_0	Avogadro's number (6.022×10^23)	$[1/\mathrm{mol}]$
D	Diffusivity	$[\mathrm{m}^2/\mathrm{s}]$
S	Oxygen solubility in the binder	$[\mathrm{mol}/\mathrm{m}^3\,\mathrm{Pa}]$
K_{SV}	Stern-Volmer constant	$[1/\mathrm{Pa}]$
I	Wind-on luminescent intensity	$[\mathrm{W}/(\mathrm{m}^2\,\mathrm{sr})$ or a.u.$]$
I_{ref}	Wind-off luminescent intensity	$[\mathrm{W}/(\mathrm{m}^2\,\mathrm{sr})$ or a.u.$]$
I_λ	Spectral luminescent intensity	$[\mathrm{W}/(\mathrm{m}^2\,\mathrm{sr\,nm})$ or a.u.$]$
(x, y)	Wind-off coordinates	$[\mathrm{m}]$
(x', y')	Deformed wind-on coordinates	$[\mathrm{m}]$
x	Reference quantity of the axial direction	$[\mathrm{mm}]$
y	Reference quantity of the pitchwise direction	$[\mathrm{mm}]$
l	Reference quantity of the curvilinear suction side direction	$[\mathrm{mm}]$
z	Reference quantity of the spanwise direction	$[\mathrm{mm}]$

C	True chord	[mm]
C_{ax}	Axial chord	[mm]
L	hspace-0.6cm Suction side curvilinear length	[mm]
H	Blade span	[mm]

Dimensionless Quantities

$[S_0]$	Singlet ground state population
$[S_1]$	Excited singlet state population
$[S_2]$	Second excited singlet state population
$[T_1]$	Excited triplet state population
$[L_0]$	Ground state population
$[L^*]$	Excited state population
Φ	Yield of luminescence
Φ_0	Yield of luminescence without quenching
ϕ_{O_2}	Mole fraction of oxygen in the testing gas
A	Stern-Volmer coefficient
B	Stern-Volmer coefficient
R	Wind-on color intensity ratio
R_0	Wind-off color intensity ratio
$M_{out,is}$	Isentropic exit Mach number
$Re_{out,is}$	Isentropic exit Reynolds number

List of abbreviations

CO2	Carbon Dioxide
NOX	Nitrogen Oxides
GTF	Geared TurboFan
LPT	Low-Pressure
BPR	By-Pass Ratio
SFC	Specific Fuel Consumption
VKI	Von Karman Institute
SPLEEN	Secondary and Leakage Flow Effects in High-SPeed Low-PrEssurE TurbiNes
BL	Boundary Layer
PS	Pressure Side
SS	Suction Side
RANS	Reynolds-Averaged Navier-Stokes
URANS	Unsteady Reynolds-Averaged Navier-Stokes
CFD	Computational Fluid Dynamics
CAD	Computer Aided Design
2D	Two Dimensional
3D	Three Dimensional
PSP	Pressure Sensitive Paint
TSP	Temperature Sensitive Paint
PIV	Particle Image Velocimetry
ROI	Region Of Interest
F	Fluorescence
P	Phosphorescence
IC	Internal Conversion
EC	External Conversion
ISC	InterSystem Crossing
MPP	Macro Porous Polymer
PtTFPP	Platinum meso-Tetra (PentaFluorophenyl) Porphine
TLC	Thin-Layer Chromatography
AA	Anodized Aluminum
PC	Polymer/Ceramic
LED	Light Emitting Diode
CCD	Charged-Coupled Device
CMOS	Complementary Metal Oxide Semiconductors
PMT	PhotoMultiplier Tube
PD	PhotoDiode
SNR	Signal-to-Noise Ratio
FFC	Flat-Field Correction
IR	InfraRed
UV	Ultraviolet

RGB	Red Green Blue
OD	Optical Density
A/D	Analog to Digital
NASA	National Aeronautics and Space Administration
AEDC	Arnold Engineering Development COmplex
ONERA	Office National d'Etudes et de Recherches Aérospatiales
DLR	Deutsches Zentrum für Luft- und Raumfahrt
ISSI	Innovative Scientific Solutions Incorporated
KTH	Kungliga Techniska Högskolan
FSTI	FreeStream Turbulence Intensity
WG	Wake Generator
LE	Leading Edge
TE	Trailing Edge
OS	Object Signal
PSD	Power Spectral Density
FS	Full Scale
RSS	Root-sum squared

List of Figures

List of Tables

Chapter 1

Introduction

1.1 Problem overview and motivations

The design of the next-generation civil aircraft has been an issue of major importance recently. Air traffic is expected to increase in the upcoming years and engine manufacturers have set ambitious goals raising new social, environmental and governmental challenges. The target is to achieve 75% reduction in CO2 emissions, 90% reduction in NOX and 65% in perceived noise by 2050, compared to 2000 values [8]. To face this challenge, the design of modern aircraft engines have been studied in detail, aimed at maximizing efficiency and reducing noise and fuel consumption. Among the innovative propulsion unit architectures, the Ultra High By-Pass Ratio (BPR) Geared TurboFan (GTF) has been identified as a key concept for greener and efficient engines. Using a gearbox to decouple the fan and low-pressure turbine (LPT) speeds, the GTF allows the increase in rotational speed of the LPT. This engine architecture becomes even more actractive for BPR>10 since it reduces specific fuel consumption (SFC), weights and stage counts. Nevertheless, the increase in rotational speed of the LPT generates new challenges in terms of aerodynamic and structural design because of the larger centrifugal stresses. The LPT operates at challenging operating flow conditions difficult to reproduce, characterized by transonic exit Mach numbers ($M_2 > 0.9$) and low-Reynolds numbers.

The S-1/C wind tunnel of the von Karman Institute is world-class turbine rig for testing large-scale, transonic, low-Reynolds number linear cascades. In the frame of the large EU-funded project SPLEEN [6] (Secondary and Leakage Flow Effects in High-SPeed Low-PrEssurE TurbiNes) commissioned by Safran Aircraft Engines, the S-1/C transonic linear cascade has been adapted to investigate the combined effect of secondary, cavity purge/leakage and unsteady flows with the mainstream under representative engine-scaled flow conditions. Quantitative measurements of surface pressure are essential to understanding of the aerodynamic performance. The current linear cascade has been instrumented by a large number of pneumatic and fast-response pressure taps, and surface mounted hot-films to study the flow interactions, boundary layer (BL) transition, flow separations, horseshoe vortices and unsteady shocks. The sensor locations have been selected strategically using computational fluid dynamics (CFD) tools such as traditional quasi-2D URANS and fully turbulent RANS analyses, positioned in the most critical regions of the central blade's pressure side (PS) and suction side (SS), and on the two endwall passages adjacent to the central blade. Nevertheless, pressure taps shows limitations in terms of intrusiveness and spatial resolution of measurements, allowing possible blockage from dust and/or particles, additional interactions with the flow, and giving as output only discrete values of pressure. Moreover, manufacturing, tubing and preparing a model with a large number of pressure taps for wind tunnel testing is very labor-intensive and costly [30].

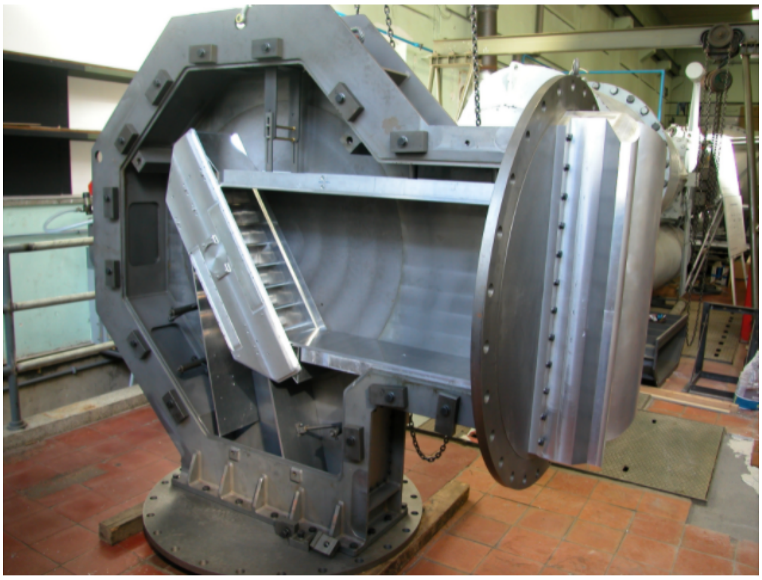

Figure 1.1: View of the test section of the VKI S-1/C high-speed low-Reynolds linear cascade

New optical sensors based on the quenching mechanisms of luminescence have been developed since 1980s. Those sensors constitute the so-called 'Pressure Sensitive Paint' (PSP). This advanced technique offers incredible advantages compared to conventional measurement techniques. PSP provides optic, non-contact, full-field measurements of 2D surface pressure on complex geometries with much higher spatial resolution and lower cost. The paint, constituted by luminescent molecules reactive to the partial pressure of oxygen present in the air, can be easily sprayed over any complex surface. Therefore, the design of a S-1/C optimized setup and the realization of the PSP experimental measurments was considered to be ideal for future pressure mapping in the facility. Nonetheless, PSP measurement techniques shows some limitations in the complexity of the setup design, measurement procedure and post-processing. The paint must be excited by a proper light source with a specific wavelength and an optical acquisition system has to capture the field of view of the region of interest (ROI). In a final stage, the processed images are translated into surface pressure variations through a previous ex-situ calibration of the PSP. For this reasons the implementation of an optimal pressure sensitive paint setup represents a tough challenge of major importance. No previous research on the application of a PSP measurement technique in S-1/C has ever been carried out, therefore the adaptation of PSP to the test rig needs to be fully designed, increasing the difficulty and the motivation behind the work.

1.2 Purpose

The ultimate purpose of this thesis is to help gaining a deeper understanding of the aerodynamic performance of the S-1/C linear cascade of the von Karman Institute, aimed at reproducing representative transonic Mach and low-Reynolds numbers to simulate the performance of the next-generation aircraft engine architectures. More specifically, providing reliable 2D full-field steady-state pressure data on the airfoils' SS and on the endwall passages between two adjacent blades through the experimental measurement technique of PSP. The work will contribute in the investigation of secondary and leakage flow effects in the frame of the project SPLEEN [6] addressed to Safran Aircraft Engines.

1.3 Goals

The project focuses on achieving the following main objectives:

- Design of the setup of the calibration and rig measurement chains of PSP measurements
- Preparation, mounting/dismounting process of instrumentation in the calibration test section
- Calibration of the test articles (setup and control, acquisition, data storage, etc.)
- Data post-processing of the PSP images

1.4 Outline

The text of the thesis is articulated in several chapters. The first chapter presents a general introduction to the problem, highlighting the motivations behind the work and the final goals. Chapter 2 aims to provide a theoretical background to PSP, describing the basic physical principles behind the technique and the specific methodology adopted. Chapter 3 devotes the attention to the test facility, the existing flow conditions, the mechanical constraints and the requirements related to the experiment. Chapter 4 highlights the decisions taken into consideration for designing the setup in the measurement and calibration test sections compared to the setups available in the state of the art. It also describe the procedures for the preparation, mounting/dismounting process of instrumentation for the the calibration of the test articles. Chapter 5 focuses on the experimental testing procedures for the intermediate components' calibrations, for the spectrometer analyses and for the calibrations of the samples, describing the experimental flowcharts for preparation, data acquisition and storage. Chapter 6 shows the data-processing procedures, the results obtained and it provides a reliability assessment. Finally, Chapter 7 summarizes the overall work highlighting the final achievements and discussing the limitations, with some insights on the future perspectives.

Chapter 2

PSP: Theoretical background and State of the art

In this chapter, a theoretical background on the principles of pressure sensitive paint is presented. These information are of great importance to a deeper understanding of the PSP technique, the methodology applied and the choices taken into consideration during the design phase. The chapter has been divided into several smaller sections. In a fist stage, the pros and cons of PSP compared to conventional pressure measurement techniques are presented. Then, the attention is focused on the physical concepts of luminescence involved in PSP. The following section is devoted to the methodology and data-processing. Afterwards, a description of the typical PSP structure and its components is shown, in combination with the desirable properties of pressure sensitive paints its application technique. Subsequently, a general overview of the typical basic instrumentation is provided, combined to a final explanation of the existing solutions in the literature.

2.1 Advantages and limitations

Pressure sensitive paint is an optical technique developed since the 1980s used in the aerodynamic field able to provide quantitative pressure data of a model subjected to a complex flow. Compared to conventional measurement techniques such as pressure transducers or taps, PSP has several advantages, listed below [30], [29]:

- Non-intrusive
- Much higher spatial resolution (2D full-field surface measurements, no longer discrete predetermined locations) comparable to that of numerical simulations
- Inexpensive application costs
- Applicable on complex model geometries

On the other hand, pressure sensitive paint technique presents also drawbacks such as:

- Resolution limited by detection system
- Lower accuracy
- Limited to optical access applications
- Relatively expensive initial costs (for the preparation of the setup)
- Higher complexity in the setup, testing phase and data-processing

Most of the limitations in the PSP application come from the setup dependency. The design of the experiment and the procedure to follow depend largely on the test section. In addition, toxicity of the paint and photo-degradation to light make the implementation even more complex and hazardous. Nevertheless, its use represents a cost-effective strategies on large models for wind tunnel testing applications, that otherwise would require hundreds of discrete pressure points to have an acceptable pressure field. PSP is also a smart choice for turbomachinery applications, especially to detect the pressure field on small highly-instrumented blades or inserts of various geometries subjected to complex aerodynamic flows. Data acquisition is performed through the optical accesses present in the facility, and its non-intrusiveness represents a strong advantage for research purposes since the model can be subjected to additional measurement techniques at the same time without influence from PSP. M.Bitter et al [17] have carried out a research study on a LPT blade, by means of the simultaneous application of optical PSP and PIV measurement techniques with no interference between the two.

2.2 Physical principles

2.2.1 Kinematics of luminescence

The physical concepts regard the excitation/emission properties of the luminophore molecules contained in a binder permeable to oxygen, typically a polymer. The Jablonski energy-level diagram in Figure 2.1 shows the different energy levels and the typical photophysical processes of luminescence for a luminophore. When a luminophore absorbs a photon of radiation from a light source with a certain wavelength, it gets excited from the ground electronic singlet state S_0 to the excited electronic singlet states S_1, S_2 and triple state T_1 (based on the electron spin orientation) as described by

$$S_0 + h\,\nu \rightarrow S_1 \tag{2.1}$$

where h is the Planck constant and ν is the frequency of the excitation light. The excited electron returns to the unexcited ground state through both radiative and radiationless processes. In the radiative process, called luminescence (a general term that involves both the fluorescence and the phosphorescence processes), the luminescent molecule emits radiation with a higher wavelength compared to the excitation one due to the Stokes shift (from energy conservation). The following equations describe the fluorescence and the phosphorescence processes respectively.

$$S_1 \rightarrow S_0 + h\,\nu_f \tag{2.2}$$

and

$$T_1 \rightarrow S_0 + h\,\nu_p \tag{2.3}$$

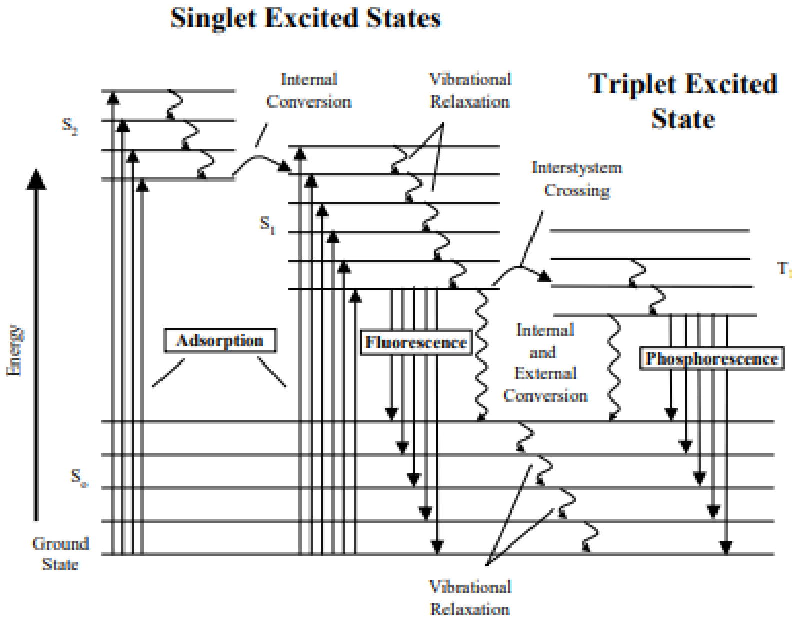

Figure 2.1: Jablonski energy-level diagram

Those emissions are filtered out from the excitation wavelengths and captured as images by a proper detection system, as shown in Figure 2.2. Oxygen quenching is the most relevant radiationless process for PSP, for which the excited state can be deactivated by the interaction with the oxygen molecules present in the binder that quenches the radiative emission. Additional radiationless processes deactivate the excited electronic states. The main processes are internal conversion (IC) $S_2 \rightarrow S_1 + heat$ and $S_1 \rightarrow S_0 + heat$, intersystem crossing (ISC) $S_1 \rightarrow T_1 + heat$ and $T_1 \rightarrow S_0 + heat$, and external conversion (EC) when the energy tranfer is between the excited molecules and the external environment. Luminescence deactivation by EC increases with higher temperatures because of the increased frequency of collisions. This process is the thermal quenching, which is the major photophysical mechanism for temperature sensitive paint (TSP). Table 2.1 summarizes the photophysical processes involving electronically excited states. Further details concerning the kinematics of luminescence can be found in [30] and [26].

Step	Process	Rate
Excitation	$S_0 + h\,\nu \rightarrow S_1$	$k_{S_1}[S_0]$
Fluorescence (F)	$S_1 \rightarrow S_0 + h\,\nu_f$	$k_f[S_1]$
Internal Conversion (IC)	$S_1 \rightarrow S_0 + heat$	$k_{ic}[S_1]$
Intersystem Crossing (ISC)	$S_1 \rightarrow T_1 + heat$	$k_{isc(s_1-t_1)}[S_1]$
Phosphorescence (P)	$T_1 \rightarrow S_0 + h\,\nu_p$	$k_p[T_1]$
Intersystem Crossing (ISC)	$T_1 \rightarrow S_0 + heat$	$k_{isc(t_1-s_0)}[T_1]$

Table 2.1: Photophysical processes involving electronically excited states

For engineering applications is not necessary to analyze all the photophysical processes. Therefore a simplified lumped model considers only the core processes involved in PSP, listed below.

- Luminescent emission (radiative process)
  $L^* \rightarrow L_0 + h\,\nu_l$, rate constant k_r
- Oxygen quenching (radiationless process)
  $L^* + O_2 \rightarrow L_0 + O_2^*$, rate constant k_q
- Temperature-dependent deactivation (radiationless process)
  $L^* \rightarrow L_0 + heat$, rate constant k_{nr} which is temperature-dependent

The rate of change of the population of the excited state $[L^*]$ is obtained from the following first-order differential equation

$$\frac{d\,[L^*]}{dt} = I_a - (k_r + k_{nr} + k_q\,[O_2])\,[L^*] \tag{2.4}$$

where $I_a = k_{s1}[L_0]$ is the rate of excitation (k_{s1} is the constant rate of excitation and $[L_0]$ the population of the ground state. At steady state $\frac{d\,[L^*]}{dt} = 0$ and with no oxygen quenching $[O_2] = 0$ equation 2.4 becomes

$$I_a = (k_r + k_{nr})\,[L^*] \tag{2.5}$$

The quantity yield of luminescence Φ describes the amount of luminophores in a given excited state, defines as

$$\Phi = \frac{rate\,of\,luminescence}{rate\,of\,excitation} \tag{2.6}$$

Therefore it can be expressed as

$$\Phi = \frac{k_r\,[L^*]}{I_a} = \frac{k_r}{k_r + k_{nr} + k_q\,[O_2]} = \frac{I}{I_a} \tag{2.7}$$

where I is the luminescent intensity. Without oxygen quenching the yield of luminescence can be expressed as

$$\Phi_0 = \frac{k_r\,[L^*]}{I_a} = \frac{k_r}{k_r + k_{nr}} = \frac{I_0}{I_a} \tag{2.8}$$

where I_0 denotes the luminescent intensity without quenching. Dividing equation 2.8 by equation 2.7, is it possible to obtained the Stern-Volmer relation

$$\frac{\Phi_0}{\Phi} = \frac{I_0}{I} = 1 + \frac{k_q}{k_r + k_{nr}}\,[O_2] = 1 + k_q\,\tau_0\,[O_2] \tag{2.9}$$

where $\tau_0 = \frac{1}{k_r + k_{nr}}$ represents the luminescent lifetime without oxygen quenching. The luminescent lifetime with the oxygen is $\tau_0 = \frac{1}{k_r + k_{nr} + k_q\,[O_2]}$. Therefore τ, Φ and I are related according by

$$\frac{\Phi_0}{\Phi} = \frac{\tau_0}{\tau} = \frac{I_0}{I} = 1 + k_q\,\tau_0\,[O_2] \tag{2.10}$$

Rate constants k_{nr} and k_q are generally temperature-dependent. This dependency can be divided in two terms for the rate constant of the non-radiative processes: a temperature independent term and a temperature-dependent term described by the Arrhenius relation

$$k_{nr} = k_{nr0} + k_{nr1}\,\exp(-\frac{E_{nr}}{RT}) \tag{2.11}$$

where $k_{nr0} = k_{nr}\,(T = 0)$ and k_{nr1} are the rate constants of the two terms, E_{nr} denotes the activation energy for the non-radiative process, R is the universal gas constant and T is the absolute temperature in Kelvin.

The temperature-dependency of the quenching rate constant is due to oxygen diffusion in the polymer, which is considered homogeneous. Smoluchowski relation describes the phenomenon as

$$k_q = 4\,\pi\,R_{AB}\,N_0\,D \tag{2.12}$$

where R_{AB} is the interaction distance between the luminophore and the oxygen, N_0 denotes the Avogadro's number and D describes the diffusivity which is temperature-dependent and can be modelled by the Arrhenius relation as

$$D = D_0\,\exp(-\frac{E_D}{RT}) \tag{2.13}$$

where $D_0 = D\,(T = 0)$ and E_D is the activation energy for the oxygen diffusion process.
According to Henry's law, the concentration of oxygen in the polymer binder is proportional to the partial pressure of oxygen in gas above the polymer. In case of air, the oxygen partial pressure is proportional to the pressure p that acts on the PSP surface (Dalton's law of partial pressures).

$$[O_2]_{polymer} = S\,p_{O_2} = S\,\phi_{O_2}\,p \tag{2.14}$$

where S represents the oxygen solubility in a polymer binder layer and ϕ_{O_2} is the mole fraction of oxygen in the testing gas (it corresponds to 21% in the atmosphere, but it varies according to

the testing facilities).
Accordingly, the higher is air pressure above the PSP model, the higher is oxygen concentration in the PSP polymer which leads to a larger number of quenched molecules and therefore to a decreased luminescent intensity in the detected images. Substituting all the terms in equation 2.9 and introducing additional coefficients, the Stern-Volmer relation can be rewrite as

$$\frac{I_{ref}}{I} = A_{polymer}\left(T\right) + B_{polymer}\left(T\right)\frac{p}{p_{ref}} \tag{2.15}$$

where the luminescent intensity is inversely proportional to local air pressure. In most wind tunnel applications air is containing 25% oxygen. Therefore it is quite difficul to obtain the zero-oxygen condition denoted as I_0. Typically it is used the zero-speed (wind-off) condition as a reference. I_{ref} and p_{ref} are the luminescent intensity and air pressure at a reference condition, respectively. A and B are the Stern-Volmer coefficient which are temperature-dependent and are experimentally determined by calibration. The intensity ratio $\frac{I_{ref}}{I}$ compensates the effects of non-uniform illumination, uneven coating and non-homogenous luminophore concentration in the paint. Tipically, in wind tunnel testing applications, I_{ref} and I are called wind-off intensity when the tunnel is turned off and wind-on intensity when it is turned on, respectively. Once the Stern-Volmer coefficients are determined, the pressure field can be calculated from the luminescent intensity via equation 2.15.

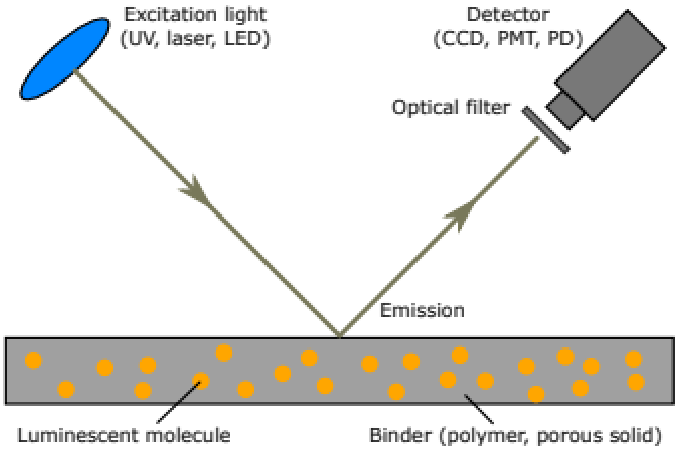

Figure 2.2: Excitation and emission properties of PSP

For aerodynamic application, the empirical non-linear Stern-Volmer equation can be also computed by a polynomial relation.

$$\frac{I_{ref}}{I} = A\left(T\right) + B\left(T\right)\frac{p}{p_{ref}} + C\left(T\right)\left(\frac{p}{p_{ref}}\right)^2 \tag{2.16}$$

2.2.2 Temperature sensitivity effect

Temperature sensitivity represents the most relevant error in PSP measurements. Two different strategies can be adopted to compensate for this effect.

- Low-temperature-sensitive PSP.

  As described by equations 2.12 and 2.13, temperature sensitivity of PSP mainly depends upon the oxygen diffusion process. When designing a low-temperature-sensitive PSP, the polymer binder should have small activation energy for oxygen diffusion E_D so that $B_{polymer}$ is a weak function of temperature. In the 'ideal PSP' case where $E_D \approx E_{nr}$ over a certain range of temperature, the Stern-Volmer coefficients $A_{polymer}(T)$ and $B_{polymer}(T)$ have the same temperature dependency, therefore their ratio is temperature independent. If rewriting equation 2.15 as follows

$$\frac{I_0(T)}{I(p,T)} = 1 + K_{SV}(T)\,p \tag{2.17}$$

  where $I_0(T) = I(p=0,T)$ is the intensity at zero pressure (vacuum) and K_{SV} is a coefficient described by the following formula

$$K_{SV}(T) = \left(\frac{B_{polymer}(T)}{A_{polymer}(T)}\right) / \, p_{ref} \tag{2.18}$$

  for 'ideal PSP', the Stern-Volmer equation becomes temperature independent.

  An example of 'ideal PSP' is depicted by the bichromophic molecule Ru-Pyrene immersed into a MPP(macro porous polymer) acrylate polymer binder. Figure 2.3 shows the Stern-Volmer calibration curves for Ru-Pyrene/MPP PSP as functions of different temperatures in the span 25-55 °C. Due to its temperature independency, the curves are collapsed onto a single one.

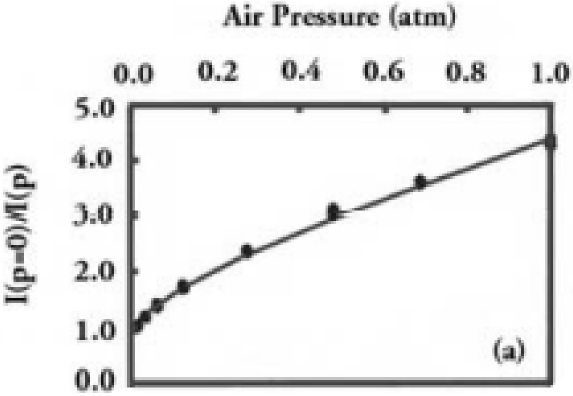

Figure 2.3: The Stern-Volmer plots for Ru-Pyrene/MPP PSP at eight pressures ranging from 0.005 to 1 atm and four temperatures from 25 to 55 °C

- Multi-luminophore PSP.

  An efficient way of correcting temperature dependency in PSP measurements is considering multi-luminophore paints. This strategy is typically used in test sections where temperature varies considerably during the experiment without ways of controlling that variation. A two-luminophore PSP (also called 'Binary PSP'), consists of two luminophores immersed in the same binder. The two luminescent molecules must have the same temperature dependency so that their ratio shows a very weak temperature dependency and the same excitation properties such that only one illumination source is necessary. One luminophore is pressure-sensitive whereas the second luminophore is pressure-insensitive. Therefore the former, used as a probe, reacts to oxygen quenching to evaluate the pressure, the latter is only used as a reference for temperature dependency in order to compensate for this effect. The two emission spectra do not overlap, thus they can be separately acquired using two different optical filters. Since the two luminophores cannot be perfectly mixed, the simple two-color intensity ratio $\frac{I_{\lambda 1}}{I_{\lambda 2}}$ is not sufficient to compensate the effect of non-uniform dye concentration and paint thickness variation, but it can only eliminate the effect on spatially non-uniform illumination. Accordingly, a ratio of ratios $(\frac{I_{\lambda 1}}{I_{\lambda 2}})\,/\,(\frac{I_{\lambda 1}}{I_{\lambda 2}})_0$ should be considered. Figure 2.4 shows an example of the ratio of ratios of a binary PSP (PtTFPP in fluoroacrylic polymer FIB with a reference luminophore) as function of pressure at different temperatures. $R = (\frac{I_{\lambda 1}}{I_{\lambda 2}})$ and $R_0 = (\frac{I_{\lambda 1}}{I_{\lambda 2}})_0$ are the two-color intensity ratios between the probe and reference luminophores at the run and reference conditions, respectively. The five curves at different temperatures overlap, so that the ratio of ratios results independent from temperature sensitivity in the range 5-45 °C.

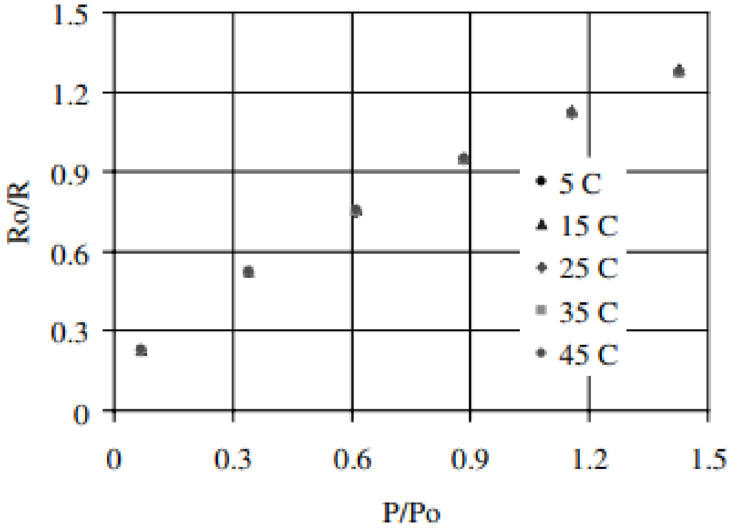

Figure 2.4: Ratio of ratios of a two-luminophore PSP (PtTFPP in FIB with a reference luminophore) as a function of pressure at different temperatures

2.3 Methodology

2.3.1 Radiometric notation

The luminescent intensity 'I' cited in paragraph 2.2.1 physically represents the luminescent radiance (denoted by 'L' according to radiometric notation) defined as the radiant energy flux per unit solid angle and per unit projected area of an elemental surface of PSP (units: $W\,m^{-2}\,sr^{-1}$). Therefore, the radiance is function of position and direction. The direction of the radiance is given by the local polar coordinated θ (polar angle) and ϕ (azimuthal angle), shown in Figure 2.5. In the literature of radiative heat transfer, the radiant intensity is typically denoted by the letter 'I', representing the radiant flux per unit solid angle (units: $W\,sr^{-1}$), which is different from the radiance. To avoid confusion, in the PSP literature it is typical to identify the luminescent intensity by the letter 'I', which represents the radiance as physical quantity. The spectral luminescent intensity is denoted by 'I_λ' (units: $W\,m^{-2}\,sr^{-1}\,nm^{-1}$). For a simplified model, a plausible assumption is to consider as isotropic the radiation from a luminophore, hence the radiance is independent of the azimuthal angle.

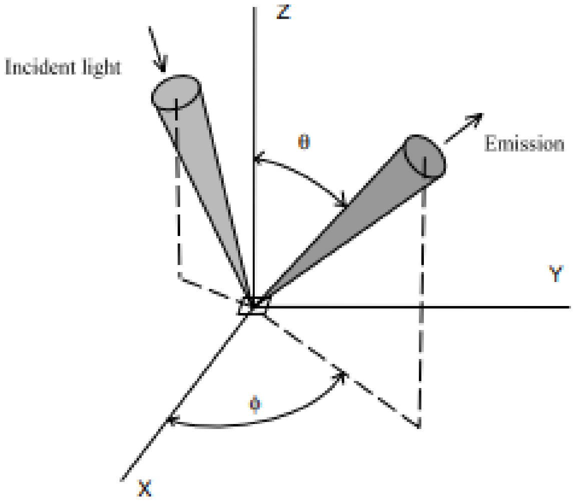

Figure 2.5: Incident excitation light and luminescent emission in a local polar coordinate system

2.3.2 Intensity-based method

There are mainly three method applications of PSP. The intensity-based method is the most used and it has been selected as the best method to achieve the goals of this thesis thanks to the advantages it provides. It is the simplest and most pressure-sensitive method for PSP, especially in case of steady state pressure measurements, where there is no need of high-speed image acquisition. It considers the intensity ratio to eliminate the effects of spatial variations in illumination, paint thickness, and molecule concentration. The method uses the Stern-Volmer equation (2.15) to obtain the local air pressure from the ratio of the wind-off and wind-on output images. Therefore, the intensity-based method requires two readings (reference wind-off and wind-on images). It is also necessary a spectral separation between the excitation and the emission peaks. The intensity-based method requires the use of a continuous light source among LEDs, Filtered lamps (Halogen, Xenon), Lasers and a photodetector such as cooled scientific grade charged-coupled device (CCD) and complementary metal oxide semiconductors (COMS) cameras (slow scan, low noise), photomultiplier tube (PMT), photodiode (PD).

2.3.3 Basic data processing for intensity-based method

The core and simpler data processing procedure in the intensity-based method is taking the ratio between the reference wind-off and the wind-on images. As described in paragraph 2.3.2, the intensity ratio between those images corrects the effects of non-homogenous illumination, uneven paint thickness and non-uniform luminophore concentration. Nevertheless, the data-processing procedure must include further complex techniques for error compensation. Aerodynamic loads induces model deformations, which results in misalignment between the wind-on and the wind-off images. In additions, post-processing techniques must consider background and camera noises, variations in illumination, temperature-dependency effect and self-illumination.

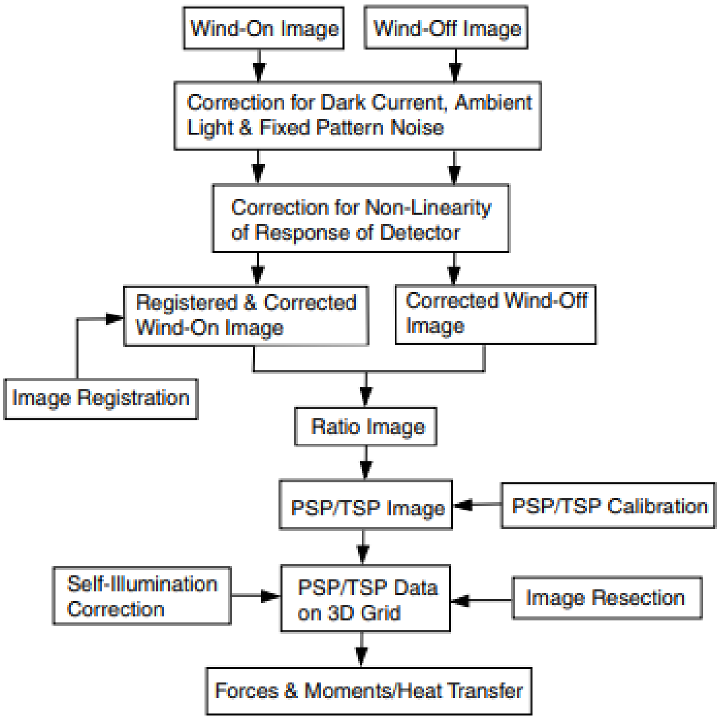

Figure 2.6: Generic data processing flowchart for intensity-based PSP and TSP measurements

Figure 2.6 shows a generic data-processing flowchart that is typically considered for intensity-based PSP with a CCD camera system. The signal-to-noise ratio (SNR) of the CCD camera can be increased by averaging a sequence of acquired frames. To compensate from background noises, a dark current image and the averaged ambient light frame are subtracted from both the averaged wind-on and wind-off images. The dark current image is acquired when the camera shutter is closed; whereas the ambient lighting images are captured when the camera shutter is open while all controllable light sources are turned off, since in wind tunnel testing sections there is always a weak ambient light that may cause errors in the measurements. To correct the fixed pattern noise, a flat-field image has to be acquired from an ideally uniform illumination field. Afterwards, The images will be divided by the normalized flat-field image to compensate the variations in illumination detected by the camera. This procedure is called flat-field correction (FFC). Moreover, the scientific grade CCD camera should be radiometrically calibrated to correct the non-linearity. Although CCD cameras has generally a good linear response of the camera output to the incident irradiance of light, sometimes they show a non-linear response, therefore a radiometric camera calibration technique may be necessary to increase the images quality. Before taking the intensity ratio, the wind-off and wind-on images must be realigned through the image registration technique to compensate for a possible model deformation caused by aerodynamics loads. This correction procedure is critical to obtain good results in the measured pressure field, especially to distinct flow features such as BL transition, flow separation and shock. This compensation technique, based on a mathematical transformation $(x', y') \mapsto (x, y)$, maps the deformed wind-on image coordinates (x', y') onto the wind-off image coordinates (x, y). The image registration geometric correction method is not able to compensate for variations in illumination level due to a model movement in non-homogenous illumination field. Nonetheless, this error can be neglected if the illumination field is almost homogeneous and the model movement is small. Afterwards, the corrected averaged wind-off and wind-on images can be divided to compute the intensity ratio and the Stern-Volmer coefficients $A(T)$ and $B(T)$ obtained from the ex-situ calibration can be applied to obtain the pressure field. However, $\frac{I_{ref}}{I}$ depends on both pressure and temperature and the model surface temperature must be known. The temperature variations can be compensated by multi-luminophore PSP and tandem use of PSP with TSP. TSP, infrared (IR) cameras and numerical simulations could also be used. Nevertheless, these methods, determined 'a priori' as ex-situ calibration generate a systematic error in the derived pressure field due to certain uncontrollable factors in wind tunnel environment. In-situ calibration is therefore fundamental to compensate for this systematic error. The intensity-ratio values are correlated to the pressure tap data. The accuracy of in-situ calibration depends upon the number and the discrete locations of the pressure taps in relation to the pressure gradients and the temperature field on the model surface. At this point, PSP data can be mapped onto a 3D grid according to the image resection technique. The mapping is necessary for computation of aerodynamic loads and for comparison with CFD simulation results. In order to map the pressure data onto the grid, firstly the camera interior and exterior orientation parameters and lens distortion parameters must be known by solving the perspective geometrical collinearity equations. Due to aeroelastic deformation in wind tunnel test, the rigid CFD or the CAD surface grids must be changed into deformed surface grids to obtain good-quality mapped pressure fields. Finally, the mapped pressure distribution can be integrated to compute the aerodynamic forces and moments on the surface. After image resection, the self-illumination correction can be implemented. Self-illumination is a distortion effect due to the luminescent illumination of a part of the model from another illuminated surface of the same model, thus it results in an increased output illumination of the self-illuminated surface. It depends on the geometrical surfaces (typically it occurs on convex surfaces) and the reflecting properties of a paint layer. Both analytical and numerical correction schemes can be implemented for solving this issue.

Multi-luminophore PSP represents a strategy for both temperature-sensitivity compensation and for a simplified data post-processing. The two color intensity ratios $\frac{I_{\lambda 1}}{I_{\lambda 2}} = f(p, T)$ can eliminate the effect of spatially non-uniform illumination on a surface. Nevertheless, this intensity ratio cannot fully compensate the non-homogeneous dye concentration and paint thickness variation effects, since the two luminophores cannot be perfectly mixed. Hence, this errors can be eliminated only considering the ratio of ratios $(\frac{I_{\lambda 1}}{I_{\lambda 2}})/(\frac{I_{\lambda 1}}{I_{\lambda 2}})_0$. Anyway, the image registration procedure still needs to be implemented.

2.3.4 Additional methods for PSP

The lifetime method is a time-based method that considers the lifetime decay of the luminophores in PSP after excitation light is turned off. It uses equation 2.15 with the luminescent lifetime ratio $\frac{\tau_{ref}}{\tau}$, which is dependent of pressure and temperature. It is insensitive to excitation intensity distribution, image registration error and camera pixel sensitivity. However, this method requires a more complex setup since it needs a pulsed excitation source and a fast shutter camera such as PMT, PD [19].

Finally, the frequency-based method relies on the phase shift from excitation. Using a fixed modulation frequency, the phase angle is a function of the luminescent lifetime τ, which in turn depends upon pressure and temperature [29].

2.4 Pressure sensitive paints

2.4.1 Typical pressure sensitive paints and substrates

PSP is mainly composed of two components: the luminophore molecules and a binder material. A first distinction is made according to the type of binder. There are two conventional methods of allowing oxygen quenching in pressure sensitive paints, listed below

- Oxygen-permeable polymer binder.
  As illustrated in paragraph 2.2.1, the oxygen present in the local environment permeates into the binder containing the luminophores to quench the radiative emissions. Oxygen quenching is controlled by the combineation of Henry's law, which takes into consideration the oxygen solubility of the polymer, and Dalton's law of partial pressure, correlating the local air pressure to the concentration of oxygen present in the test section.

- Porous binder.
  In this configuration, the binder is a porous material with large macroscopic pores (much larger than the oxygen molecule size). Therefore porous-based PSP presents much larger open surfaces where the luminophores are present and where oxygen can directly quench the luminescent emission. Figure 2.7 shows clearly the different structure of the two PSP models. The two advantages of having a porous binder in PSP are the following. Because of the much larger open surface area, PSP shows a very fast time response, which is fundamental for unsteady measurements). In addition, PSP measurements are also possible at cryogenic temperatures since oxygen diffusion is not prevented through a conventional homogeneous polymer binder. As a drawback, porous PSP is not easy to attach to wind tunnel model surfaces. The physical principles that controls oxygen quenching in porous materials are also different from polymer-based PSP, since the oxygen molecules do not permeate anymore into the binder according to its solubility. There are two models for oxygen quenching in porous-based PSP: the absorption controlled model and the collision controlled model. In the first model oxygen quenching occurs because of the absorption and diffusion of the oxygen molecule into the luminophore. In the collision-controlled model, instead, the oxygen molecule quenches the luminophore molecule after it collides to the luminophore.

The typical process to prepare a conventional polymer-based PSP is dissolving a luminescent dye and a polymer binder in a solvent solution. After the solvent evaporates, the luminescent molecules

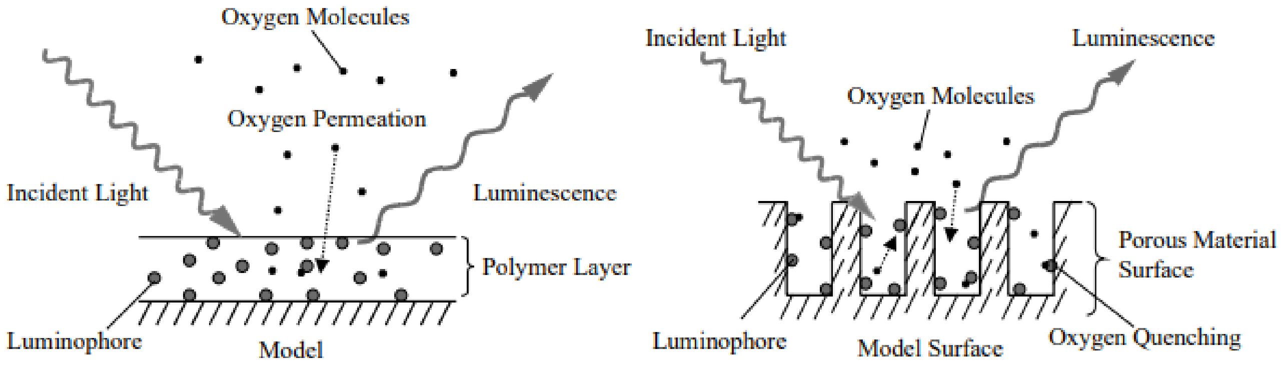

(a) Polymer-based PSP **(b)** Porous-based PSP

Figure 2.7: Schematic comparison of conventional polymer PSP (a) and porous PSP (b)

are immobilized in the polymer matrix. The selection of the proper binder can change completely the final properties of the paint (paragraph 2.4.2). Typical PSP binders include Silicone rubbers, GP-197, fluoropolymers (FIB, FEM), silica gel and sol-gel-derived coatings [30]. Polymer binders are generally commercially available, easy to apply on the model surface, soluble in common solvents (even though some of them are toxic), show good mechanical strength and optical properties. Porous material are used for fast-response pressure measurements and cryogenic temperature applications. The PSP properties depend also on the interaction between the binder and the luminescent molecules. There are mainly three families of luminescent dyes [31]. Polycyclic aromatic compounds (Pyrene und Perylene derivatives) are cheap and commercially available, they offer a wide variety of synthetic transformations and have a low-sensibility to temperature. Anyway, they suffer from photo-degradation and sublimation. Porphyrine derivatives (Platinum Porphyrins) are stable compounds with very high oxygen sensibility. On the contrary, they shows numerous limitations such as low luminescent intensity at atmospheric pressure, long lifetime, difficulties during the preparation (difficult synthesis and purification, use of toxic solvents) which make them expensive and not all commercially available. Finally, Ruthenum derivatives (Ru Polypyridyls) are very photo-stable compounds, with low temperature sensitivity and good for cryogenic wind tunnel applications. However, they are generally expensive, of difficult synthesis, purification, suffer from photo-degradation and sublimation and they are difficult to incorporate into the binder.
Typical properties of common PSPs are presented in Figure 2.8.

The most widely used porous binder materials for unsteady flow PSP measurements are thin-layer chromatography (TLC) plate, anodized aluminum (AA) and polymer/ceramic (PC) [13] [21]. Commonly used halogenated solvents for the preparation of PSP are chlorinated organic and fluoro-based solvents such as dichloromethane, trichloroethane, chloroform and benzotrifluoride. All of them are highly toxic and require a systematic safety working procedure. Additives for PSPs include aluminum oxyde, titanium dioxide and silica gel.

A PSP structure is mainly composed of three layers, depicted in Figure 2.9, [27].

- Screen layer.
  Directly attached to the model surface, the screen layer, or basecoat, is a special white paint applied under the PSP active layer to provide optical homogeneity on the model surface.

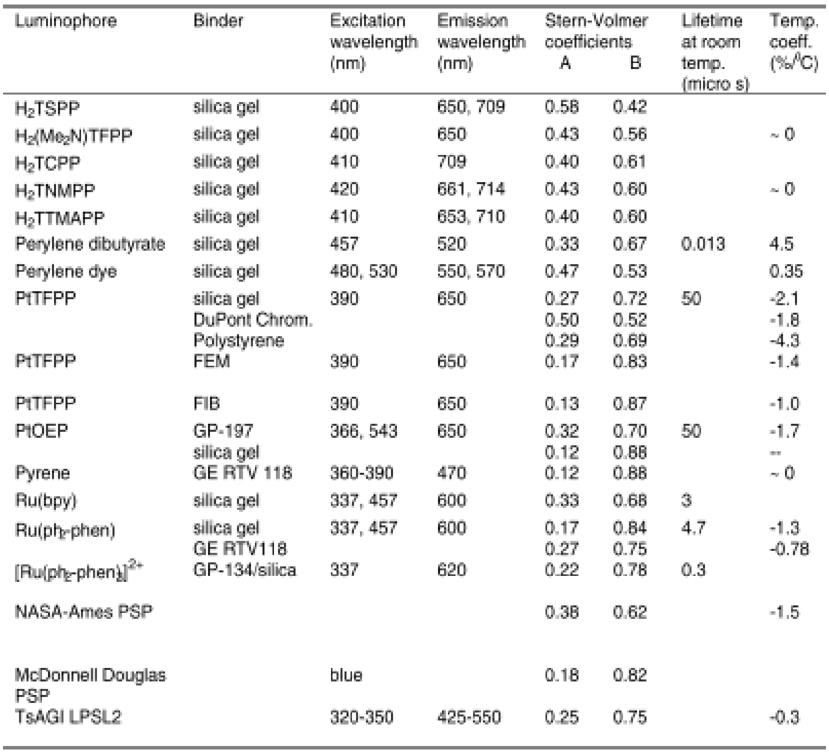

Luminophore	Binder	Excitation wavelength (nm)	Emission wavelength (nm)	Stern-Volmer coefficients		Lifetime at room temp. (micro s)	Temp. coeff. (%/°C)
				A	B		
H_2TSPP	silica gel	400	650, 709	0.58	0.42		
$H_2(Me_2N)TFPP$	silica gel	400	650	0.43	0.56		~ 0
H_2TCPP	silica gel	410	709	0.40	0.61		
H_2TNMPP	silica gel	420	661, 714	0.43	0.60		~ 0
$H_2TTMAPP$	silica gel	410	653, 710	0.40	0.60		
Perylene dibutyrate	silica gel	457	520	0.33	0.67	0.013	4.5
Perylene dye	silica gel	480, 530	550, 570	0.47	0.53		0.35
PtTFPP	silica gel	390	650	0.27	0.72	50	-2.1
	DuPont Chrom.			0.50	0.52		-1.8
	Polystyrene			0.29	0.69		-4.3
PtTFPP	FEM	390	650	0.17	0.83		-1.4
PtTFPP	FIB	390	650	0.13	0.87		-1.0
PtOEP	GP-197	366, 543	650	0.32	0.70	50	-1.7
	silica gel			0.12	0.88		--
Pyrene	GE RTV 118	360-390	470	0.12	0.88		~ 0
Ru(bpy)	silica gel	337, 457	600	0.33	0.68	3	
$Ru(ph_2\text{-}phen)$	silica gel	337, 457	600	0.17	0.84	4.7	-1.3
	GE RTV118			0.27	0.75		-0.78
$[Ru(ph_2\text{-}phen)_3]^{2+}$	GP-134/silica	337	620	0.22	0.78	0.3	
NASA-Ames PSP				0.38	0.62		-1.5
McDonnell Douglas PSP		blue		0.18	0.82		
TsAGI LPSL2		320-350	425-550	0.25	0.75		-0.3

Figure 2.8: Typical pressure sensitive paints

Thanks to this substrate, the reflected excitation light is enhanced, contributing to the increase of the output emission intensity. In addition, it provides independency from the model surface material.

- Contact layer.
  The contact layer is a very thin substrate applied between the screen layer and the active layer to ensure the proper adhesion. It is rarely present since typically included in the basecoat, which is specific in terms of desirable properties and adhesion for the chosen active layer.

- Active layer.
  The upper layer represents the core of PSP. Conventionally depicted as a polymer binder with high oxygen permeability (porous binder in case of porous-based PSP), with the luminescent probe molecules. In case of Binary PSP, it includes two different luminescent molecules.

2.4.2 Desirable properties of PSP

A good pressure sensitive paint should present the following properties:

- Pressure sensibility.
  Pressure sensitivity is one of the most relevant characteristics of a PSP. It is a major contributor of accuracy for pressure measurements. It allows to recognize and distinguish the flow phenomena especially in small pressure gradient environments. However, for experiments at high pressure, it may cause unwanted sever oxygen quenching, thus reducing the SNR of the photodetector.

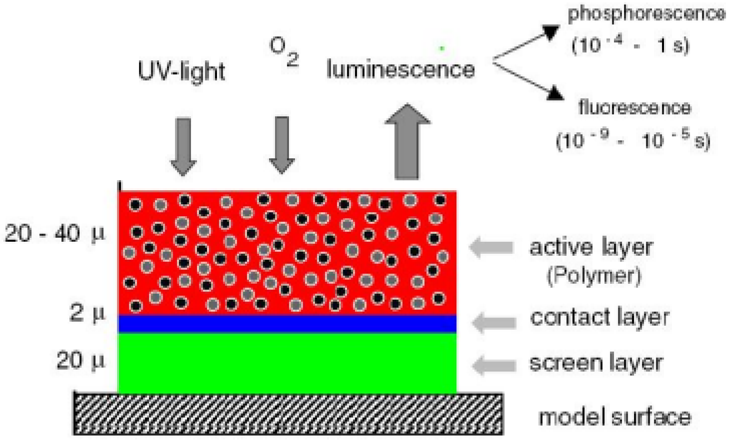

Figure 2.9: Structure of PSP

- Luminescent intensity output.
  The luminescent intensity is proportional to the concentration of luminophores present in the binder. High luminescent output increases the SNR of the photodetector. Nonetheless, if the luminophore concentration is too high, it may cause self-quenching.

- Paint stability.
  Due to photodegradation of the luminophores when exposed to an excitation light source, the luminescent intensity of a PSP decreases with time. A stable paint reduce this phenomenon. Moreover, a good PSP should ensure a stable emitting illumination.

- Response time.
  The response time of PSP mainly depends on the oxygen diffusion through the active layer. A porous binder and a small paint thickness increase the response time. This offers an advantage for fast-response unsteady measurements, but it results in low SNR for steady-state PSP applications.

- Temperature sensitivity.
  It produces the greatest errors in PSP measurements if neglected. A good paint must have a weak temperature dependency (typically involving two-luminophores). It does not represent a severe condition in wind tunnel testing applications under temperature-controlled environments.

- Physical characteristics.
  Required physical properties of PSP include a strong adhesion to sustain surface skin friction in high-speed flows. Hardness depends mainly on the polymer binder. According to N. Zerelli [24], a brittle paint increases the risk of spalling when subjected to high-speed, pressure or temperature, especially in turbomachinery applications. Coating smoothness and layer thickness strongly depend on the application techniques, described in paragraph 2.4.3. It is generally desirable to minimize the coating roughness and thickness. Typical maximum values for thickness are 20-40 μm ([30] [16] [18]). In addition, viscosity takes a key role in

the application of PSP. If it is too low (less that 10 cP), it leads to splattering and thus it increases the surface roughness [24].

- Chemical characteristics.
  As regards safety, toxicity of PSP is a relevant issue. A typical safety procedure can be found in paragraph 2.4.3. Chemical features include the possibility of easily spraying and removing of the painted layer on the test articles and the solvent evaporation rate which must be controlled under different conditions of temperature and humidity.

2.4.3 Application technique

The best application technique is through spraying. In this way is possible to homogeneously deposit the painted layer on the test article, with reduced values for roughness, in order to decrease the refracted emission light and enhance reflection. Therefore, a spray gun which controls the spraying pressure is necessary. Before applying the paint, the model surface must be brushed with grade abrasive paper ([21]), cleaned with acetone ([14] [2]) and degreased, reducing as much as possible the unevenness and the dust particles (especially if no basecoat is applied). Indeed, basecoat provides optical uniformity and proper adhesion regardless the surface material for the application of the above PSP layer. Typical values for working pressure of the spray gun are around 1.5 bar ([3] [2] [24]). Viscosity below 10 cP should be avoid because of their high risk of splattering, which leads to increase the surface roughness. On the other hand, too high viscosity needs to be sprayed at lower working pressure (0.8 bar is a good compromise). N. Zerelli [24] suggests a viscosity range of 10-25 cP. Thickness of the paint is another issue. A small number of paint layers will increase the response time (which is not relevant for steady-state measurements), but it will reduce the SNR, hence the luminescent intensity. Otherwise, too many layers may induce paint separation from the metal during testing. T. Liu and J.P. Sullivan [30] recommend a PSP thickness in the span 20-40 $\mathrm{\mu m}$. The paint application should be carried out by moving the spray gun slowly. The hand and arm movement should remain constant along each application passage. Typical range for the number of paint layers are from 10 to 20. If the model surface is sufficiently large, each layer consists of several (very light) cross-coats working from left to right or right to left while moving down the model, then work back up left to right or right to left. Additional recommendations for best results include to allow painted coats to dry for a few seconds and to stop when having a good coverage over the whole surface. The drying time depends on several conditions, such as the paint thickness, the air humidity and the ventilation. A covered and well ventilated area is recommended, and the painted surface must not be exposed to ambient light while drying. Many hours may need for drying. In addition, heat curing in a oven at 60-75°C (if more than 100°C it may lead to non-uniformity [30]) for around 2 hours may be useful for strengthen the paint ([26] [17] [21]).

Since most of the PSPs are toxic, working operators must wear a proper safety equipment (protective eyewear, protective glasses, filtered mask and safety suit). According to C. Martin [2], it is important to follow a precise safety procedure. Beakers, balances and stirrers and any surface in contact with the paint have to be cleaned after each use with acetone. During paint spraying, a plastic sheeting should be used to create a division between the operator and the spray gun emission, guiding the fumes towards a ventilation hood (a suitable painting lab is necessary). After drying, the painted samples should be handled with gloves, protecting them from any possible touch and transferred to a dark plastic box avoiding the ambient light. Finally, most of the paint can easily be removed by acetone.

2.5 Instrumentation setup

There are two mainly systems for acquiring the PSP images: CCD camera system and laser scanning system, as shown in Figure 2.10. A CCD camera system is most commonly used for PSP. It requires the application of the paint on the model surface, which is excited by a proper illumination source (LED array, UV lamp or laser). The output luminescent emission is filtered by optical filters, and the resulting images are digitized and transferred to a computer for data post-processing. Scientific grade CCD cameras are able to provide high intensity resolution (from 12 to 16 bits), and high spatial resolution (typical values are: 512x512, 1024x1024, 2048x2048 pixels). Larger pixel size determines a larger CCD sensor, which is effective to enhance the SNR but may reduce the spatial resolution. In addition, CCD cameras show a good linear response and a high SNR. On the contrary they are expensive and with a slow frame rate (not relevant for steady-state measurements). When multi-luminophore PSPs are considered for temperature compensation, two possibilities of image acquisition and setup exist. A binary paint emits light into two different-color peaks. Those signals can be either detected by a simple RGB CCD camera, or using two grayscale CCD cameras with proper optical filters to separate the signal. Setup design and preparation, image acquisition and data processing are much simpler if using only one camera. Anyway the high cost and unavailability of an RGB camera often leads to the second option. Optical mirrors are typically useful to orientate the images to the camera, which can be placed in a simple and safe location, especially when the optical accesses in the facility are limited. A proper camera lens must be mounted on the CCD camera. F-mount and C-mount are the most common lens type. The right focal distance and aperture values are fundamental for the maximisation of resolution in the images, related also to the working distance between the CCD sensor and the painted model surface.

The choice of the illumination source depends upon the excitation properties of the paint (typically in the range of UV rays) and the optical access of the facility (window's size and material). Moreover, a good excitation source should provide a uniform illumination field to reduce the measurement uncertainty associated with the model deformation. In case of steady-state pressure measurements, a stable continuous light source is needed. UV/blue LED arrays are very stable, light in weight, producing little heat. Their modular size is an advantage for small and various optical accesses. Other light sources include xenon arc, incandescent tungsten or halogen lamps with blue filters, collimated LED tubes, and fluorescent UV lamps.

In case of multi-luminophore PSP, it is necessary the separation between the excitation and the two emission peaks. Band-pass and long-pass filters are typically used to acquire as much and precise as possible the different luminescent signals. The dimension of the filter have to match the camera lens aperture. Optical density (OD) is a key feature for filters. This values is in the range 2.0-6.0 and it is related to the optical filter quality (i.e., high transmission percentage).

In the laser scannning system, a low-power laser beam is oriented towards a small point and scanned over the model surface by means of a computer-controlled mirror responsible for the paint excitation on the model. A low-noise photodetector PMT detects the luminescent emission transmitting the signal to a high resolution A/D converter in a computer. A lock-in amplifier is used to reduce the noise when the laser beam is modulated. The laser is synchronized to data acquisition and the laser spot position on the model is known. A laser scanning system can improve the measurement accuracy, providing uniform illumination and easy access when only limited optical windows are present in the test section. However, it requires a more complex setup.

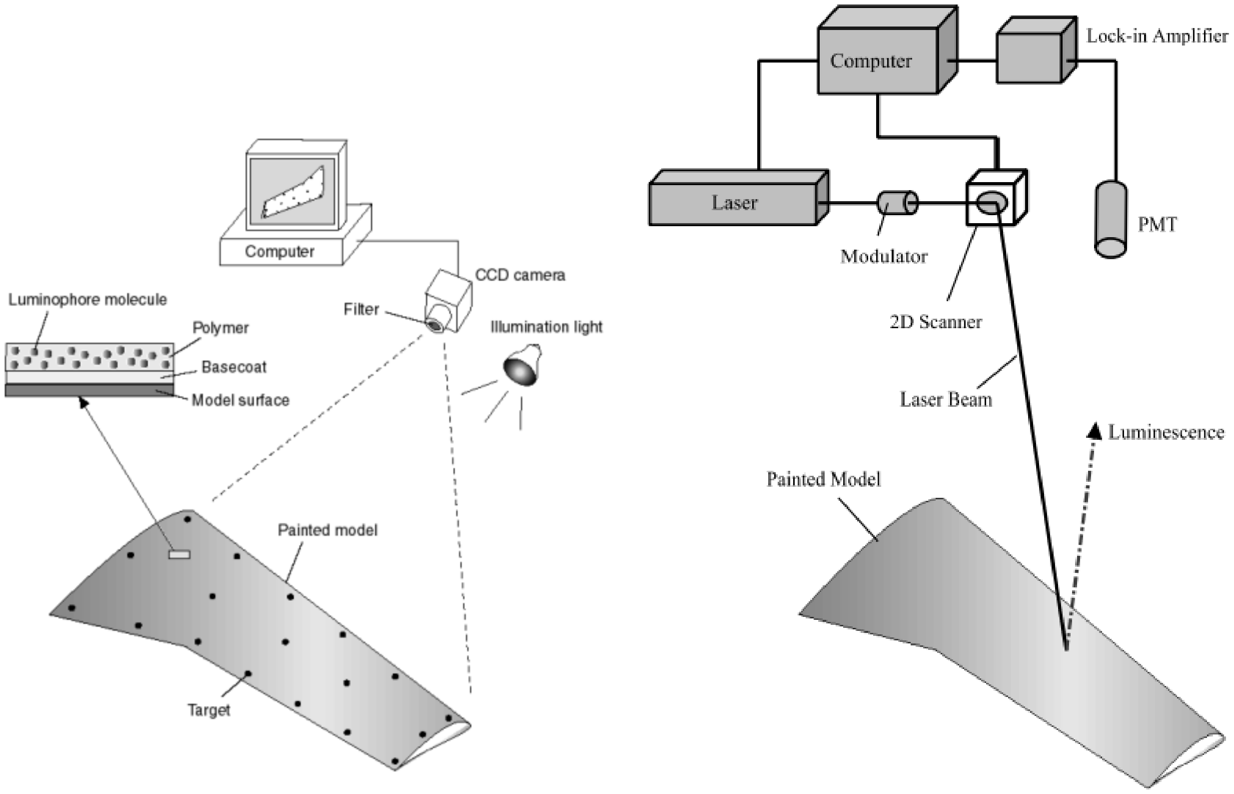

(a) CCD-PSP system **(b)** PMT-PSP system

Figure 2.10: Schematic comparison of a generic CCD camera system (a) and a PMT laser scanning system for PSP (b)

2.6 State of the art

The concept of oxygen quenching of luminescence was first discovered in 1935 by H. Kautsky and H. Hirsch [9]. However, the PSP working principles was used then only for medical and analytical chemistry. The critical step was the utility of PSP as an optical sensor for measuring surface pressure as a significant transition from conventional point-based pressure measurement to global pressure mapping. The first studies on full-field pressure measurements was developed in the 1980s by J. Peterson and V. Fitzgerald [11]. The Central Aero Hydrodynamic Institute (TsAGI) in Russia, the University of Washington, the Boeing Company and the NASA Ames Research Center were in collaboration for the application of PSP in aerodynamic experiments. In the early 1990s, at TsAGI, a large number of PSP formulations have been applied to various subsonic, transonic, supersonic, shock, dynamic tunnels, and rotating machinery detecting the images by both photographic film and TV cameras, scientific grade CCD cameras and PMT laser scanning systems. Pressure sensitive paint measurements are in productive use in a large number of worldwide laboratories. Its effectiveness was significantly investigated in the USA at Purdue, AEDC and University of Florida, at ONERA in France, at DLR in Germany and at the National Aerospace Laboratory of Japan. PSP technique is being commercialized by Innovative Scientific Solutions Inc. (ISSI) [10] of Dayton, Ohio and by OPTROD Ltd. of Moscow, Russia.

This technique has been adopted for a large variety of experiments. In 1997, K. R. Navarra [14] implemented PSP in a first-stage transonic rotor at Virginia Polytechnic Institute. N. Tillmark et al. (2000) [23] investigated on shock-BL interaction in the transonic wind-tunnel of the Royal Institute of Technology KTH in Stockholm. In 2001, L. J. Zhang and R. S. Jaiswal [15] studied the endwall surface film cooling effectiveness by means of PSP in a high-speed four passage linear turbine nozzle cascade, simulating engine-operating conditions. The scientific paper of M. K. Quinn et al. (2011) [21] in the University of Manchester reported interesting insights on the effect of various substrates. Unsteady pressure measurements were conducted in 2014 by M. Hilfer et al. [19] and J. W. Gregory et al. [13] and in 2020 by M. Bitter et al [18], using fast-response PSP instead of fast-response pressure taps for the purpose of studying shock wave and BL separation in unsteady flows. In 2016, M. Bitter at al. [17] [16] investigated the combined use of binary PSP and PIV measurements in the high-speed transonic linear cascade wind tunnel (HGK) operated by the Institute of Jet Propulsion at the Bundeswehr University Munich, simulating the 2D aerodynamic performance of a LPT at engine-scaled conditions. From 2016 to 2019, film cooling effectiveness of high-pressure low-speed rotating rig and linear cascade was studied by S. Li et al. (2016) [28], A. F. Chen et al. (2017) [1] and M. Wilhelm and H. Schiffer (2019) [22].

The von Karman Institute has enormously contributed in the research of advanced optical measurement techniques such as PSP, TSP and PIV in the recent couple of decades. Because of the numerous facilities present in VKI, these techniques have been applied for different purposes in different wind-tunnel test rigs. The implementation of a PSP technique in the H-3 longshot hypersonic wind tunnel for pressure measurements on a flat plate model was carried out by P. Giraud [25] in 2000 and by D. Munday [4] in 2003. A similar study was conducted by C. Martin [3] [2] in 2019 and 2020, analyzing the 2D surface temperature distribution by means of TSP on a flat model under hypersonic flow conditions. Experiments on pressure optical measurements were conducted in the transient compressor tube facilities CT-2 and CT-3 by N. Zerelli [24] and J. Michàek [12] in 2007. In 2011, P. Schreivogel [26] implemented a binary PSP measurement technique in CT-2 for the study of roughness-induced laminar-turbulent transition on a flat plate model in high speed flows.

No previous research at VKI has ever been carried out in the S-1/C transonic linear cascade. This makes the implementation of the PSP measurement technique more challenging since the test rig must be adapted for the application of PSP and a full design of the technique needs to be designed.

Chapter 3

Test Facility

This chapter is aimed at presenting the VKI S-1/C wind tunnel test rig, its adaptation to project purposes and the operating flow conditions. Afterwards, the chapter illustrates the experiment objective. Further, the instrumentation for conventional pressure measurements is described. An insight on the constraints and requirements for the implementation of the PSP technique is finally provided.

3.1 Continuous High Speed Cascade Wind Tunnel S-1

A continuous closed-circuit facility powered by a 615 kW axial flow compressor powers the world-class turbine rig for testing large-scale, transonic, low-Reynolds number linear cascades. A water/air cooler allows to keep the flow temperature close to ambient while keeping the air dry at all conditions. The mass flow is controlled by adjusting the rotating speed of the compressor and using a by-pass valve. The tunnel absolute pressure can be reduced to 8 kPa using a vacuum pump (Figure 3.1) [5].

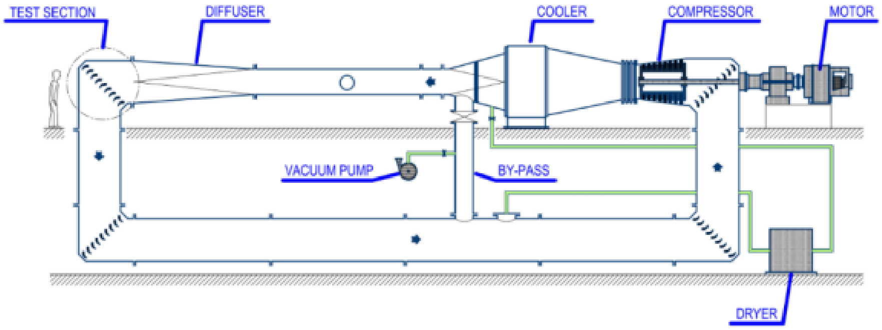

Figure 3.1: Schematic of the S-1/C closed-circuit facility

The facility is used to simulate and investigate the aerodynamic performance of a high-speed low-pressure LPT model for geared turbofan engines at representative engine conditions (Mach and Reynolds numbers, freestream turbulence levels and wake reduced frequency). A passive turbulence grid, depicted in Figure 3.2, made of an array of steel parallel rods with circular cross-section is used to control the freestream turbulence intensity (FSTI), by varying the axial distance to the leading edge (LE) of the central blade. A wake generator (WG) used to recreate upstream unsteady wakes consists of a set of cylindrical molybdenum bars mounted on a rotating disk of 625 mm diameter, which can rotate up to 3500 rpm by means of an electric motor of 30 kW (Figure 3.2).

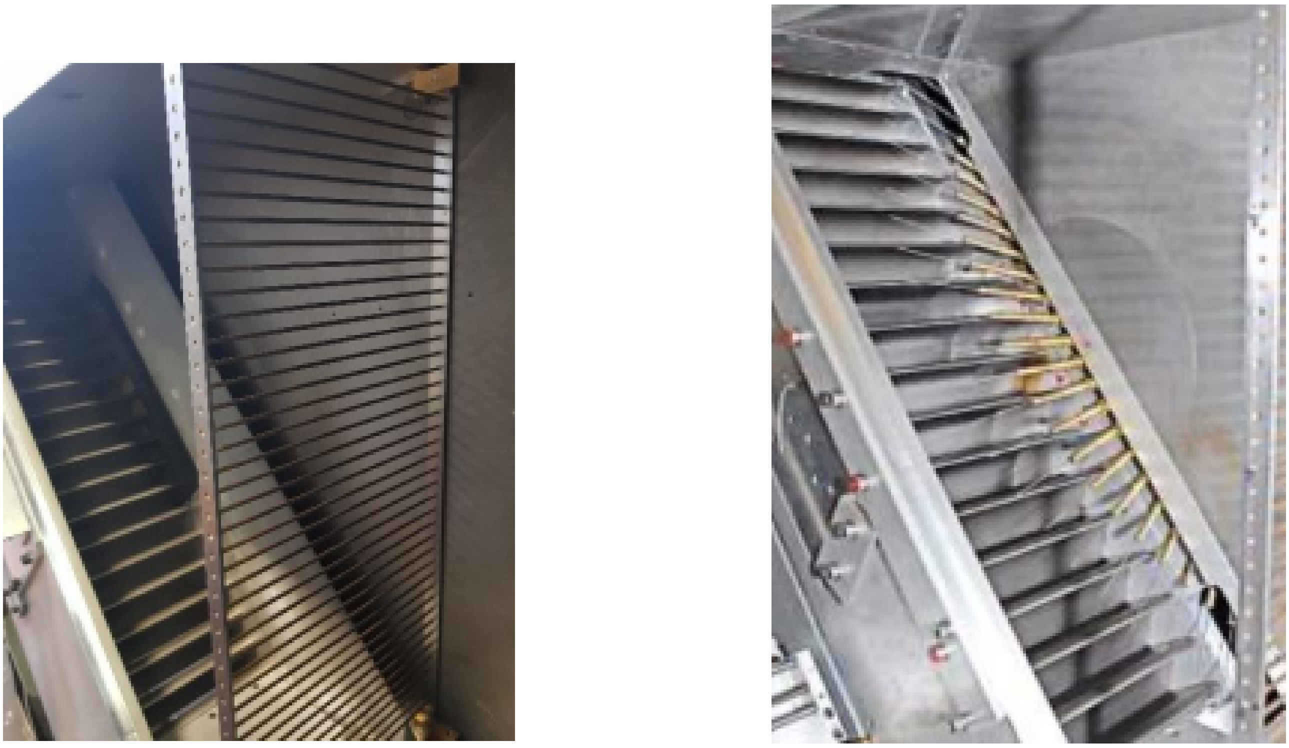

(a) passive turbulence grid **(b)** wake generator

Figure 3.2: View of the passive turbulence grid (a) and of the wake generator (b)

3.2 Adaptation of S-1/C to SPLEEN

In combination with Safran Aircraft Engines, the von Karman Institute is currently involved in the SPLEEN Project for the research of the 3D unsteady aerodynamics of the next-generation LPTs. One of the goal is the adaptation of the S-1/C facility for the study of the interaction between cavity purge, leakage and secondary flows. Three cavity-airfoil configurations have been presented by G. Lopes et al. (2021) [8] to investigate different flow interaction phenomena such as stator-rotor hub cavity purge, rotor shroud tip-casing leakage and stator shroud tip-casing purge.

The passive turbulence grid has been integrated to the test section. From a comparison between the Roach's turbulence decay law and experimental data in S-1/C, the grid as been placed 400 mm far from the central blade LE to match the required FSTI level of 2.5%.

As regards the WG design, the rotational speed of the disk, the number of bars, their length and diameter depend on several factors such as the reduced frequency and the flow coefficient to match, aerodynamic and mechanical constraints. Therefore, the choice of these parameters is the consequence of the trade-off between wake representability and mechanical robustness. A modal analysis is performed to avoid bar resonance which leads to the mechanical failure of the bars. The excitation frequencies of the facility and the bar natural frequencies determined the critical speed regions and the optimal bar length, by means of the Campbell diagram. Finally, a non-linear static analysis assessed the state of stress of the bars under centrifugal and aerodynamic loads. The final results showed the following design characteristics: 96 bars with a bar length of 130 mm and a design disk rotational speed of 3300 rpm which corresponds to a wake frequency of 5280 Hz. Figure 3.3 shows the bar-support-disk assembly. Note that a bar length of 130 mm covers approximately 70% of the blade full-span. A minimum bar length of 55% of the test section span is needed to avoid any undesired effect on the region between the endwall to mid-span.

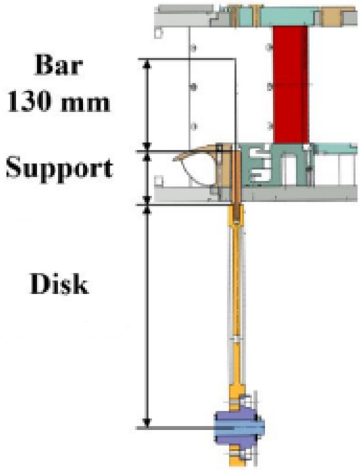

Figure 3.3: Full rotating WG assembly (disk, support and bar)

Table 3.1 displays the relevant geometric characteristics of the airfoil for the PSP experiment.

True chord, C $[\mathrm{mm}]$	52.280
Axial chord, C_{ax} $[\mathrm{mm}]$	47.610
Suction side curvilinear length, L $[\mathrm{mm}]$	66.092
Blade span, H $[\mathrm{mm}]$	165.00

Table 3.1: Airfoil geometric characteristics

The nominal operating conditions of the facility are summarized in Table 3.2.

Isentropic exit Mach number, $M_{out,is}$ [-]	0.90
Isentropic exit Reynolds number, $Re_{out,is}$ [-]	70000
FSTI [%]	2.50
Wake frequency from the WG $[\mathrm{Hz}]$	5580
Range of temperature at nominal conditions $[\mathrm{K}]$	299 - 315
Maximum temperature rate $[\mathrm{K/hour}]$	10

Table 3.2: Nominal operating conditions, and additional data of the temperature variations within the facility

3.3 Objective of the PSP experiment

The final aim of the experiment is the measurement of steady-state static pressure at nominal conditions (Table 3.2) by pressure sensitive paint on the full-span rear (29.20 - 100 %L) SS surface of the central blade of the cascade, and on the bottom endwall passage between two adjacent blades. Although a bar length of 130 mm allows allows uniformity of the WG effect only in the range endwall-mid blade span, PSP measurements of static pressure have no complications in detecting full-blade span images in the facility, therefore 100% span is considered as ROI for completeness. Moreover the spraying of the paint on a model surface can not be limited in space with very high precision, consequently, the PSP should be homogeneously applied over the whole blade surface. As described in the paragraph 3.5.2, the optical *Access 2* represents the best choice for the study of the BL in the transonic region over the blade SS, allowing a larger view of the rear suction side.

3.4 Existing steady-state static pressure measurement instrumentation

In order to study the steady-state static pressure variation on the blade SS and bottom endwall surfaces, a series of conventional pneumatic pressure taps were located on the surfaces of interest. A total of 1128 taps were placed along the central blade SS, covering the surface from bottom endwall to mid-span. Their locations were selected using the results of numerical RANS simulations. The taps have an increasing diameter close to the TE, maximizing the spatial resolution in the ROI of the rear SS transonic region, detecting possible separation phenomena.

Similarly, the two bottom endwall passages adjacent to the central blade are instrumented. Two smooth brass inserts, shown in Figure 3.4, were produced to reduce their intrusiveness to the secondary flows. They contains a total of 65 pneumatic pressure taps, whose location was selected based on the results of the steady-state numerical analyses.

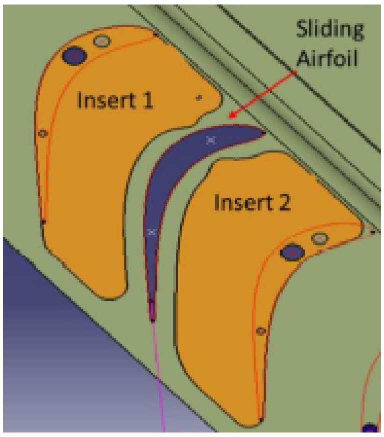

Figure 3.4: Schematic of the endwall inserts

3.5 Constraints and requirements for PSP implementation

3.5.1 Temperature variation

In order to match the nominal flow parameters, temperature in the facility reaches a value between 299 K and 315 K, depending on the period of the year and the previous use, in a time interval of approximately 30 min after powering on the wind-tunnel. At nominal operating condition (see Table 3.2), after approximately 60 min after switching on, the temperature varies around 0.5 $\mathrm{K/hour}$. In addition, the temperature variations can not be reduced or controlled in any way, and no instrumentation is present to measure the blade surface temperature. The temperature variation effect forces to choose a binary PSP, which involves a more complex setup, discussed in detail in Chapter 4.

3.5.2 Optical accesses

Three optical accesses, shown in Figure 3.5 are present in the VKI S-1/C for the purpose of the experiment. While *Access 3* has no impact on the detected field of view since it includes the entire bottom endwall passages adjacent to the central blade, *Access 1* and *Access 2* do not allow a full axial/streamwise view of the SS blade. Table 3.3 presents the captural regions of *Access 1* and *Access 2*.

	Access 1	*Access 2*
x/C_{ax} [-]	0.6848 - 1	0.3217 - 1
l/L [-]	0.6141 - 1	0.2920 - 1

Table 3.3: Captural field of view on the blade SS from *Access 1* and *Access 2*

To study the BL, the flow interactions with the cavity purge flow and the whole transonic region, *Access 2* has been chosen as the best candidate to acquire the pressure distribution images on the blade SS. Nevertheless, the possibility of the inclination of the LED light and of the cameras relative to the model surfaces must be checked since it can include relevant errors in the acquired images. This analysis has been carried out and reported in Chapter 4.

Further limitations include the distances between the optical accesses and the model surfaces (data provided in Table 3.4). The higher the distance, the more difficult is to obtain high-resolution images, because of the lower emission intensity of the PSP when excited by a far illumination source (which needs to be more powerful), and the lower magnification factor required between the camera sensor and the image. The material of the windows should be in glass or cast acrylic with approximately 93% or higher transmission in the UV spectrum [10]. The current material is in plexiglass, absorbing the UV light and fluoresce green which will interfere with the signals from the PSP. Finally, the geometrical size of *Access 1* and *Access 2* (199x172 mm) can limit the choices of large high-power LED sources or large cameras. All of these issues are discussed in Chapter 4.

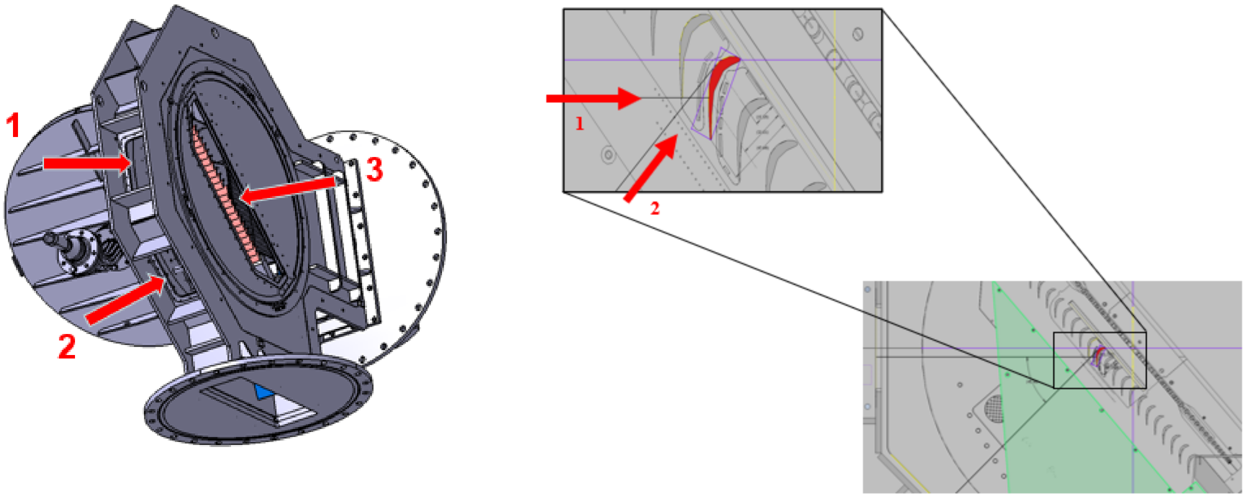

(a) 3D view of the optical accesses **(b)** Detail of the optical accesses location to the blades

Figure 3.5: 3D view of the optical accesses in S-1/C (a). 2D detailed view of the two optical accesses towards the blade SS. Image not to scale (b)

Access 1	*Access 2*	*Access 3*
571.325 [mm]	565.74 [mm]	205.00 [mm]

Table 3.4: Distance of the model surface from *Access 1*, *Access 2* and *Access 3*

Chapter 4

Setup Design

The current chapter focuses on the system specification and concept selection concerning the design of the experimental apparatus for the development of the binary PSP technique; combined with a feasibility analysis with respect to aspects such performance, cost and availability, easiness of the integration in the setup. A first section resumes the work for the literature setup analysis. Then, a list of the most relevant instrumentation is presented, with an explanation of the requirements and design choices for the implementation in the test rig. In conclusion, the design and assembly of the ex-situ calibration setup is described in detail.

4.1 Literature analysis of setups for similar applications

In order to proceed with the design of the setup for the implementation of the PSP measurement technique within the facility, first, a comparison of the existing setups in the literature for a similar application is necessary. Figures D.1 - D.6 highlight the different choices in terms of paints, illumination sources, cameras, lenses, filters, windows, and application techniques, that authors have taken into consideration for different purposes and test sections. The excel data sheet will be analyzed in detail for every choice of the setup design.

4.2 Experimental setup in S-1/C

4.2.1 Paint

The selection of the paint was made in agree with the following requirements:

- Easy and fast to use.
  Instead of preparing a in-house made PSP, which requires time for the preparation, mixing and assessment of its properties, the paint has been selected among the available PSPs on the market. The choice of a certified paint was also essential for this specific experiment, since the low-pressure condition typically leads to a very low intensity emission of the paint. In addition, further complications for the preparation of a uniform two-luminophore PSP should be avoid

(the temperature variation in the test rig requires the selection of a binary PSP, as discussed in section 3.5.1). Finally, the paint (and the basecoat) should be easy to remove from the model surface during several tests, since only a limited number of test articles is present. A low photo-degradation rate when exposed to an excitation source, and a high shelf life, are two more aspects to be taken into consideration.

- Maximize pressure sensitivity.
  The low-pressure conditions, the intrusiveness of materials that reduce the transmissivity of the excitation and emission light such as mirrors and optical accesses, and the large distance between the light source and the painted surface can strongly influence the pressure sensitivity of the PSP, thus reducing the SNR of a detecting system. For these reasons, it is fundamental to select a paint which maximizes its pressure sensitivity. The distribution of static pressure on the SS 0-50% span blade at nominal conditions, experimentally determined by pressure taps, covers the range of 5-8 kPa. Hence, the PSP must be adequate to operate in the aforementioned pressure range.

- Minimize temperature sensitivity.
  The uncontrollable temperature variation within the facility (see section 3.5.1) leads to the selection of a binary PSP, with a very weak temperature-sensitivity. This choice is fundamental since the temperature-dependency effect represents one of the largest sources of error in PSP measurements. A variation of $1\ \mathrm{K}$ in the facility can produce a dominant error in the determination of the pressure field if not compensated. Nevertheless the use of a multi-luminophore paint typically requires a more complex setup with a detecting system composed of two cameras. In addition, the temperature range of the PSP must match the operation temperature range in the test section.

PSP time response does not represent a requirement because the objective of the experiment is the pressure measurement at steady-state, and the facility can work continuously for several hours at the same flow conditions (Mach and Reynolds number).

Several authors have considered to buy pressure sensitive paints from ISSI [10] because of their high-quality performance. A comparison of two single-component PSPs and two binary PSPs from ISSI portfolio was analyzed (Figures D.7 - D.10). Binary FIB was finally selected, because of its lower temperature sensitivity (and similar pressure sensitivity) with respect to the others. Its emission properties and its calibration curve at different temperatures are summarized in Figure 4.1.

M. Bitter et al. (2016) [17] [16], and P. Schreivogel (2010) [26] consider the implementation of Binary PSP in their setups.

The selection of the can size among the available quantities was made considering the number of layers required (from both the literature review and the data instruction sheet by ISSI), the dimensions of the SS blade surface, the bottom endwall insert and the calibration samples, a prediction on the number of tests, and the cost of the PSP.

Similar considerations were made for the basecoat. FIB Basecoat from ISSI was bought because of its high-quality reflection properties when applied in combination with Binary FIB, which increases

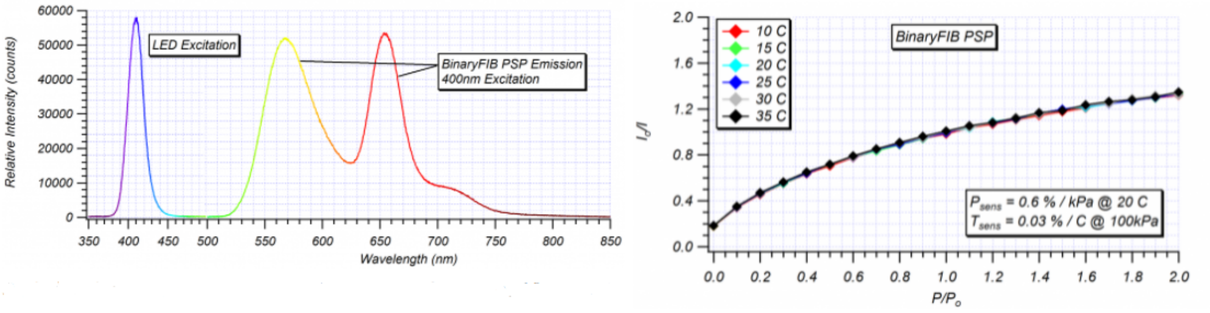

(a) **(b)**

Figure 4.1: Scaled emission spectrum of BinaryFIB PSP excited by a 400 nm LED source (a). Calibration of BinaryFIB PSP (b)

the optical uniformity of the metal surface and maximizes the luminescent intensity of the excited paint. Moreover, it is easy to remove from the model with acetone. The basecoat eliminates also the problem of spraying the paint on different metal surfaces (endwall in brass, blade in low-carbon steel, calibration samples in aluminum), giving a higher uniformity during PSP measurements.

(a) **(b)**

Figure 4.2: Can of Binary FIB PSP (a). FIB Basecoat applied on a model surface (b)

4.2.2 Photo-detection system

A CCD camera system is typically used in the literature concerning PSP, especially for steady-state measurements since no fast response is needed. The use of CCD cameras results in a simpler setup, combined with their good linear response and high SNR. As shown in Figure 4.1a, Binary FIB emits two luminescent peaks: a reference green light signal and a pressure red signal. An RGB camera solves the issue by acquiring contemporary both the signals separately, simplifying the post-processing of the images. Nonetheless, this camera is typically not available in the laboratories because of its limited use and high cost. For this reason, two grayscale cameras, which must be identical each other, were considered. Two black and white LaVision CCD Cameras were used in [17], [16] and in [26]. Among the cameras available at VKI, the selection was based upon the following requirements:

- The two cameras must be identical
- Maximize image resolution

The frame rate does not represent a constraint for the choice of the camera because of steady-state measurements. Based on the aforementioned requirements, the SpeedSense M310 Camera, 1280 px x 800 px, pixel size of 20 $\mu\mathrm{m}$, by Dantec Dynamics was selected (Figure 4.3). The image acquisition is performed via the software Phantom PCC.

Figure 4.3: Image of two SpeedSense M310 Cameras at VKI

4.2.3 Illumination source

UV LEDs represent the most common light source for PSP because of their ability in producing uniform and stable illumination, increasing the SNR of the photodetector and reducing the uncertainty related to the model deformation. LEDs are also light in weight and they produce little heat, which is good for having a simpler setup. Continuous LED sources are used for steady-state measurements. Many researchers adopted high-performance compact air-/water-cooled UV LEDs commercialized by ISSI or HardSoft ([17], [22], [1], [19]), which can be easily integrated in the setup with small optical accesses. However, their high cost leads several authors using cheaper high-power LED chip arrays ([21], [26], [27], [23]). All of these LED sources have a wavelength output around 400 nm, which represents the most typical excitation range for PSPs. The requirements for the selection of the light source are listed below.

- Target excitation wavelength (recommended by ISSI): 400 nm
- Maximize power output (limited by the availability of the power supply at VKI, which can supply at maximum 30 V DC / 3 A)
- LED dimensions should not overcome the size of the optical accesses (the most critical ones are the 60 x 60 mm side windows of the calibration chamber)

Two high-power UV LED chip arrays by Chanzon, each with a power of 100 W and a layout of 10 x 10 LED chips, were considered since available at VKI. These light sources were used by C. Martin (2019) [3], (2020) [2], for exciting a TSP. Specifications are reported in Table 4.1.

Power $[\mathrm{W}]$	100
Emission wavelength $[\mathrm{nm}]$	395
Input voltage (DC) $[\mathrm{V}]$	30 - 34
Input current (DC) $[\mathrm{A}]$	3
Max working temperature $[^{\circ}\mathrm{C}]$	60
LED size $[\mathrm{mm}]$	40 x 40

Table 4.1: Technical specifications of the high-power LED chip arrays by Chanzon

The LED chip arrays, depicted in Figure 4.4a, will be water-cooled by a heat sink system composed of two 40 x 40 mm aluminum water cooling blocks (4.4b), protecting them from overheating.

(a) **(b)**

Figure 4.4: High power LED chip array (a). Aluminum water cooling block (b)

4.2.4 Lenses

The camera lens should be chosen based on the following requirements.

- Maximize image resolution.
  The sensor size of the SpeedSense M310 Camera can be determined according to the following relation.

$$(1280\ \times\ 800)\,\mathrm{px}\cdot 20\,\mathrm{\mu m/px} = (25.6\ \times\ 16)\,\mathrm{\mu m} \tag{4.1}$$

  Recalling the overall blade suction side dimension (165 x 66.092) mm, the magnification factor (M), representing the scale of the image into the camera sensor, can be computed.

$$M_{max,l} = \frac{25.6}{165} = 0.1551 \tag{4.2}$$

  and

$$M_{max,h} = \frac{16}{66.092} = 0.2421 \tag{4.3}$$

The most stringent condition is the horizontal length (which corresponds to the blade span). For simplicity $M = 0.15$ were chosen. In that case, the field of view ideally acquired by the camera is determined as follows.

$$l_{max} = \frac{25.6}{M} = 170.6\mathrm{mm} \tag{4.4}$$

and

$$h_{max} = \frac{16}{M} = 106.7\mathrm{mm} \tag{4.5}$$

Therefore, a magnification factor of 0.15 will determine a camera field of view slightly larger than the blade size. The resolution of the acquired images is maximized since almost the total number of available pixels in the sensor is used to represent the images.

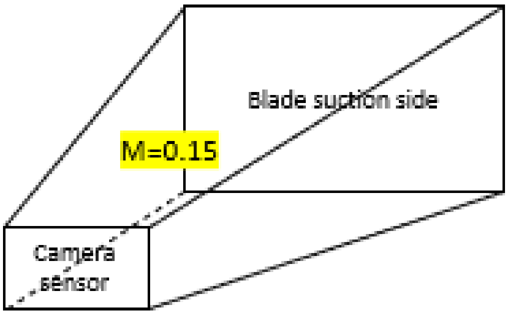

Figure 4.5: Magnification factor

- Minimum geometrical distance from the painted model.
  Table 3.4 shows the distances between the model surface and the available optical accesses in the facility. It represents a constraint for the choice of the lens focal distance. In addition, the minimum working distance between the camera sensor and the model should also consider the size of the lens, which is mounted on it. Figure 4.6 illustrates in a matrix the relation between the working distance $[\mathrm{mm}]$, the focal distance $[\mathrm{mm}]$ and the magnification factor. It is typically used in optics for the best selection of the setup. Nevertheless, this method aims to provide only a rough estimation of the correct values, which depend on several other factors. In this case it is used to select the right focal distance of the lens. The relation is described below.

$$M = \frac{focal\, distance}{working\, distance} \tag{4.6}$$

From the matrix results, a focal distance of 90mm should ideally represent the best for high resolution images for the setup in S-1/C.

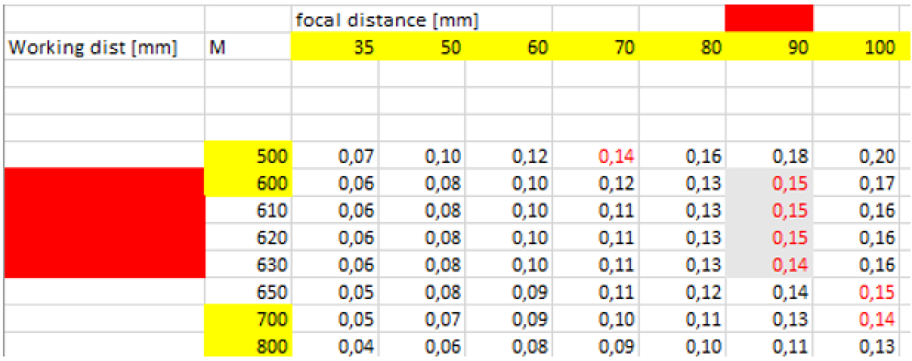

		focal distance [mm]						
Working dist [mm]	M	35	50	60	70	80	90	100
	500	0,07	0,10	0,12	0,14	0,16	0,18	0,20
	600	0,06	0,08	0,10	0,12	0,13	0,15	0,17
	610	0,06	0,08	0,10	0,11	0,13	0,15	0,16
	620	0,06	0,08	0,10	0,11	0,13	0,15	0,16
	630	0,06	0,08	0,10	0,11	0,13	0,14	0,16
	650	0,05	0,08	0,09	0,11	0,12	0,14	0,15
	700	0,05	0,07	0,09	0,10	0,11	0,13	0,14
	800	0,04	0,06	0,08	0,09	0,10	0,11	0,13

Figure 4.6: Matrix of the M factor, relation between the the working distance and focal distance

- Lens mount type.
  The SpeedSense camera allows only the combination with f-mount lenses.

- Minimum focusing distance.
  A further consideration must be made about the minimum focusing distance of the lens. Table 4.2 shows am empirical relation with the focal distance of the lens. According to these results, it does not represent an issue for the setup in the facility, however it must be considered for the calibration setup since the distance between camera and model surface is typically much lower.

Lens focal distance $[\mathrm{mm}]$	70	50	35
Minimum focusing distance (approx) $[\mathrm{mm}]$	350	370	400

Table 4.2: Minimum focusing distance in relation to the lens focal distance

- Maximum covering area for the filter placement.
  Since the use of optical filters is necessary in the PSP technique, the size of the filter must cover the total field of view of the interested image. Typically, optical filters do not overcome a diameter size of 25 mm. Among the camera lenses available at VKI, lenses with an optical distance higher than 70 mm do not cover the entire area for the filter placement.

The last point represents a more stringent requirement than the maximization of the image resolution. For this reason, and in combination to the availability at VKI, a Nikkor f-mount zoom lens 35-70 mm were selected (Figure 4.7). Anyway, the focal distance were set to 70 mm.

4.2.5 Optical filters

The application of binary PSP requires an important choice for the selection of the proper filters.

- Emission wavelength intervals.
  They must filter the light in order to both avoid the excitation UV wavelength interval and one of the two emission peaks (green or red). According to the Binary FIB emission features

Figure 4.7: Nikkor f-mount zoom lens 35-70

of Figure 4.1a, the reference and the probe emission peaks are in the range around 530-610 nm and 635+ nm, respectively. M. Bitter (2016) [16] used for Binary FIB a bandpass filter 550+/-40 nm for the green emission and a longpass filter 640+ nm to isolate the red emission. G. Barigozzi (2018) [7] adopted two bandpass filters for the two cameras in a Binary FIB study to assess the film cooling effectiveness on a nozzle vane cascade: a 550+/-50 nm and a 650+/-50 nm.

- Optical density (OD).
  Another fundamental specification is the optical density, which represents the filter's ability to absorb the radiant power that pass through, blocking the light. Typical values are in the range of OD 2.0 ($< 1\%$ transmission), OD 4.0 ($< 0.01\%$ transmission) and OD 6.0 ($< 0.00001\%$ transmission). This property is usually correlated to the filter's transmission in the range that is not filtered. OD 2.0, 4.0 and 6.0 reaches a transmission approximately higher of 85%, 90% and 93%, respectively. M. K. Quinn (2018) [20] suggests to use optical filters with an OD = 3.0 - 4.0, ideal for binary PSP eperiments. M. Bitter (2016) [16] used an OD of 6.0 in combination to Binary FIB.

- Diameter size.
  As mentioned in the previous paragraph, the optical filters must have a minimum diameter size of 25 mm.

The choice of the filter will be discussed later, after the assessment of the real emission spectrum of the PSP through the spectrometry analysis, in combination to the available optical filters on the market, their cost, and the available filters present at VKI.

4.2.6 Design of the setup assembly in the facility

The use of binary PSP requires the use of two grayscale cameras with different filters that should acquire images contemporary. In order to reduce image misalignment, the two cameras should be placed close to each other. M. Bitter et al.(2016) [4] [16] set a similar setup, where the LED were positioned on the top of the detection system, shown in Figure 4.8.

Another fundamental consideration is represented by the inclination of the excitation and emission light between the painted surface model and the detection-illumination system. However, S. Li et al.

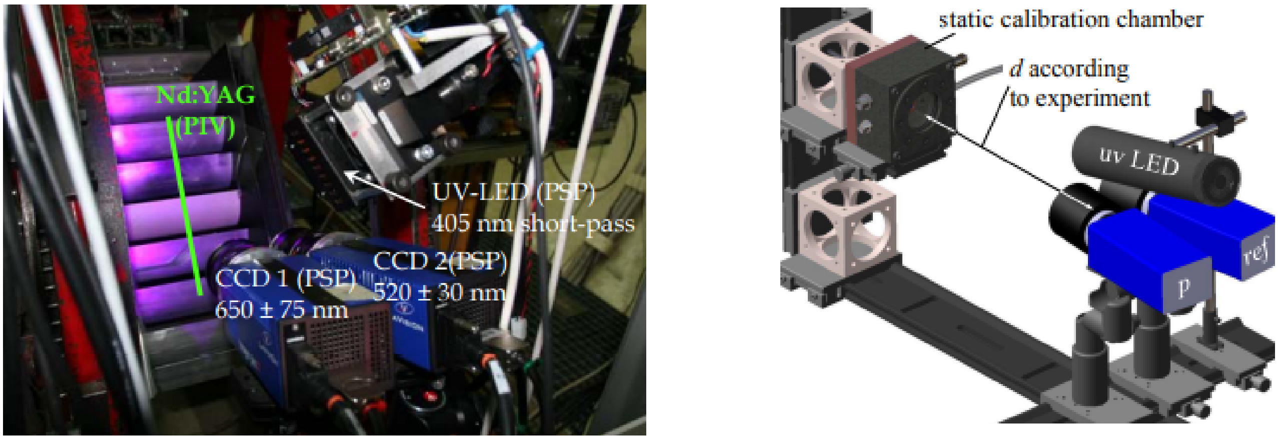

(a) **(b)**

Figure 4.8: Experimental setup for PSP - M.Bitter et al. (2016) (a). Calibration setup for PSP - M.Bitter et al. (2016) (b)

(2016) [28] studied the influence of the angle effect assessing the insensitivity of PSP measurements to camera-inclined angles, as presented in Figure 4.9.

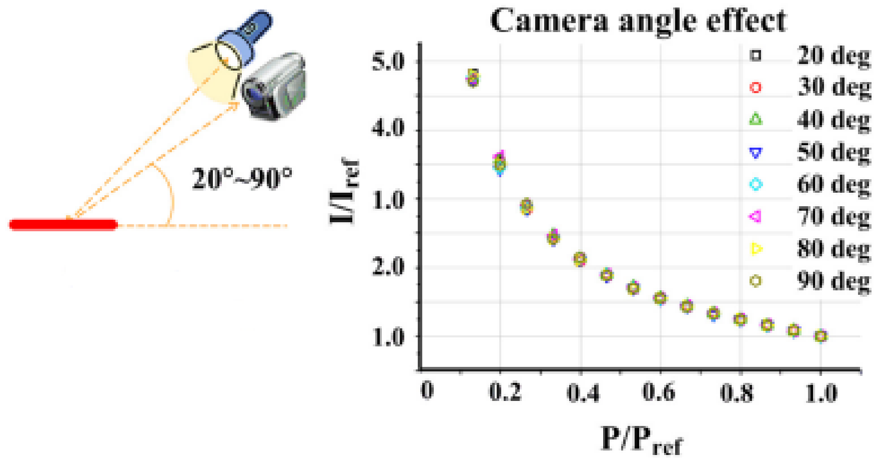

Figure 4.9: Influence of the camera-inclined angle to PSP measurements - S.Li et al. (2016)

For this reason, the use of optical *Access 2* does not represent an issue in terms of the relation between PSP results and inclination towards the blade surface.

Because of the non-availability of two identical camera lenses at VKI with a focal distance of 70 mm, and also to simplify the setup and data-processing (image registration), the implementation of a single SpeedSense M310 Camera with optical lens were designed. A support for the optical filters were 3D printed in order to rapidly change the two filters in front of the camera between the two sets of acquired images. The small time delay does not represent a problem because of steady-state measurements in S/1-C, and the processed (averaged) data pressure mapping onto the surface model is expected not to vary sensitively in a small time interval at fixed nominal conditions of the facility. The two LED chip arrays were designed to be placed at the two sides of the camera for a better illumination uniformity and symmetry. The use of a single camera and two small LEDs fits the space of the optical windows, which is large enough. The experimental apparatus includes also the two aluminum heat sinks connected to a water supply by a piping system. This setup can be also used for the in-situ data correction, where a comparison between the pressure distribution by PSP and the experimental data from the pressure taps is carried out. Figure 4.10 shows a sketch of the setup for PSP measurements in the test section.

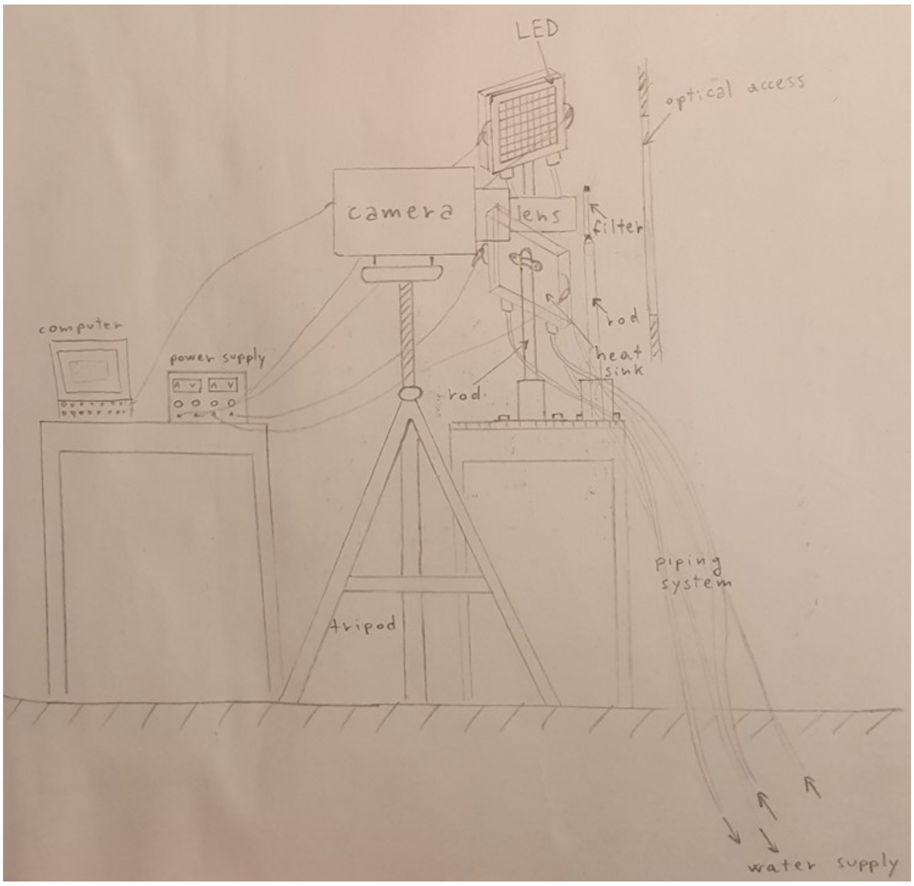

Figure 4.10: Sketch of the setup for PSP measurements in S/1-C

4.3 Calibration setup

The a-priori or ex-situ calibration is fundamental for the determination of the calibration curve for PSP. The output is the knowledge of the relation between the intensity ratio and the pressure ratio at different temperatures, such that the acquired intensity data from the detection system, mapped onto the surface model, can be translated into pressure distribution. However, the setup of the a-priori calibration is more complex than the setup shown in Figure 4.10. Moreover, the determination of the calibration curve requires additional intermediate calibrations, described in detail in Chapter 5. A (60 x 60 x 60) mm test cell was used as a calibration chamber. The chamber and a similar setup was used for the ex-situ calibration of a TSP by C. Martin (2019) [3] and (2020) [2] in VKI (see Figure 4.11).

The setup was slightly modified in order to adjust it to the scope of the PSP experiment and the available instrumentation. The chamber is constituted of three quartz side windows: two of them are the optical accesses for the two LEDs, while the other one were covered by black tape. The top surface were missing. Although a quartz or cast acrylic top window with a transmission

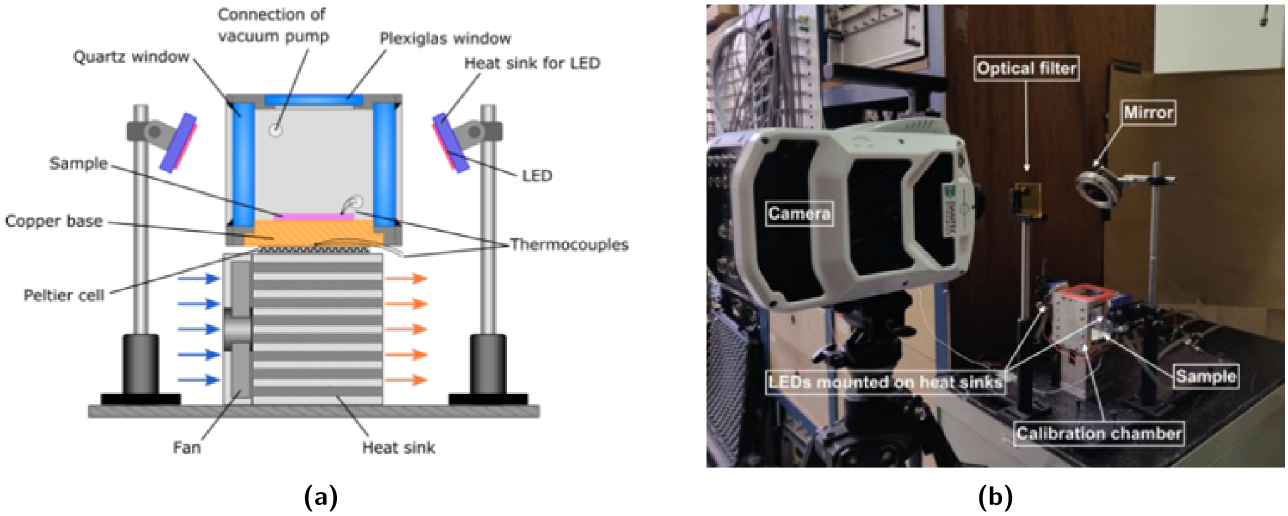

Figure 4.11: Sketch of the calibration setup - C.Martin (2019-2020) (a). A-priori calibration - C.Martin (2019-2020) (b)

higher than 90% in the two luminescent spectra would have been preferred, a plexiglass window were manufactured in VKI for simplicity. Anyway, the lower transmission of the emission light through the plexiglass does not represent a severe problem in the ex-situ calibration because the averaged lower intensity of the images would be normalized with respect to the reference intensity when computing the intensity ratio. The top window was covered at the borders with insulating tape to reduce the heat and pressure transfer with the external environment. The bottom surface of the test cell is constituted of a copper plate sealed by silicone for a better insulation with the ambient air. A type-K thermocouple is inserted in the lower central area of the copper base. Inside the chamber, a (50 x 50) mm aluminum sample is placed on the copper. The choice of the sample's material, different from the two surface materials of the blade and the bottom endwall insert in the cascade, is not fundamental because of the use of basecoat below the active PSP layer which provides optical uniformity. A Peltier cell is used to heat up the copper base (accordingly, the sample in the chamber) by a power supply. To enhance the heat extraction from the cold side of the Peltier cell, an integrated system composed of a fan and a heat sink is used. In order to allow the cold air flux, two metal supports were manufactured in VKI keeping the overall system raised off the table. The heat conduction from the Peltier cell to the copper base and the fan system is increased using conductive paste. Two telescopic bars are mounted at the sides with the supports for the LEDs and water cooling blocks connected to the water supply by a piping system. In order to allow a more uniform illumination and to avoid direct illumination towards the detection system, the LEDs were covered by two cardboard cubes. Finally, the chamber is directly connected to a vacuum pump to vary the pressure level in the box. A pressure calibrator (GE Druck DPI 610) measured the instantaneous value of relative static pressure. Plasticine and teflon were used around the junctions and the window to minimize pressure leakages. The type-K thermocouple voltage signal is transferred to a computer by means of an amplifier and an A/D converter connected in series. In a first stage, a 45° mirror support system were designed and manufactured which aimed to simplify the setup and the position of the camera and filter. Nevertheless, to increase the intensity output signal, the mirror was removed and the camera was mounted over the chamber directly pointing the plexiglass window. A fast-switching support for the optical filters was designed in VKI and supported by an optical rod system. Finally, the location in a full dark room of the whole calibration setup aims at reducing as much as possible the ambient lighting which affects both the detected images and the PSP degradation over the sample. Figure 4.12 is a schematic representation of the calibration setup. Figures 4.13 and 4.14 show the real assembly of the setup. The drawings of all the supports designed and manufactured/3D printed in VKI are shown in Appendix C.

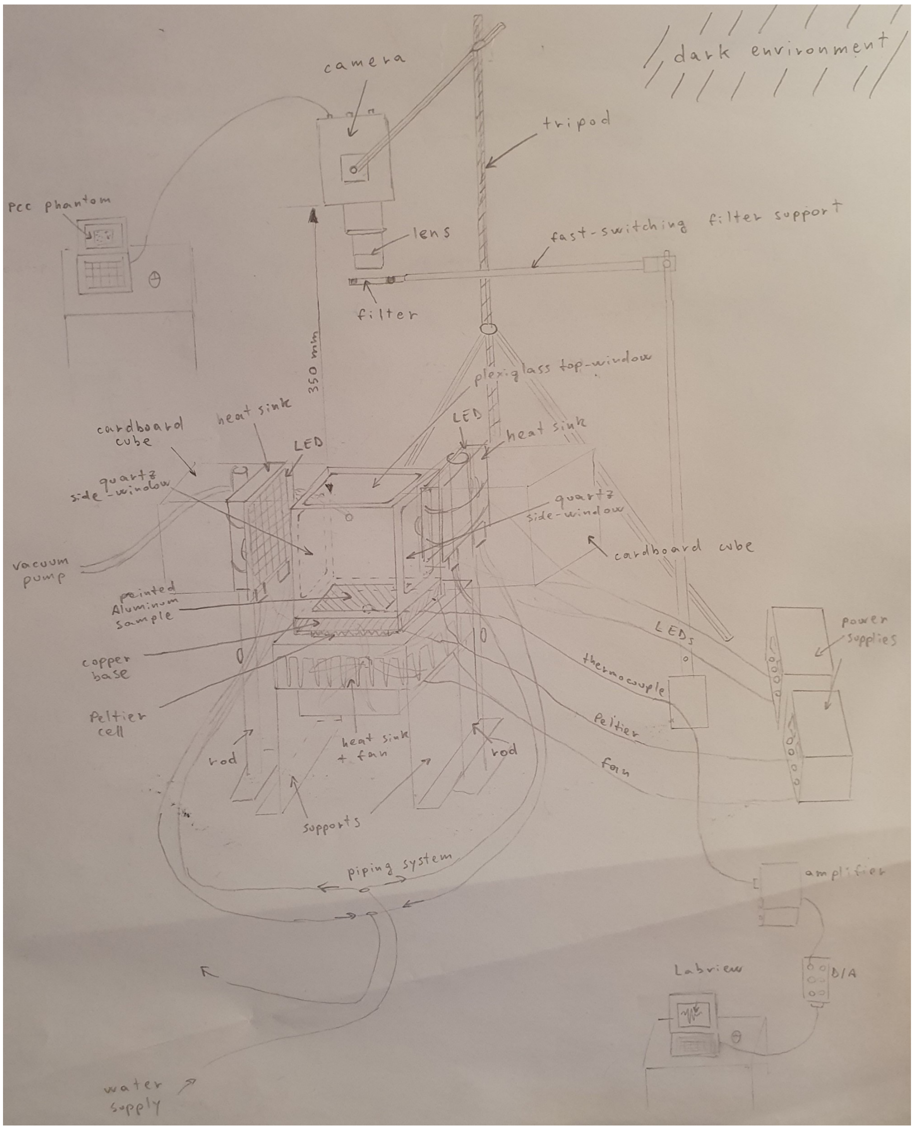

Figure 4.12: Sketch of the setup for PSP calibration

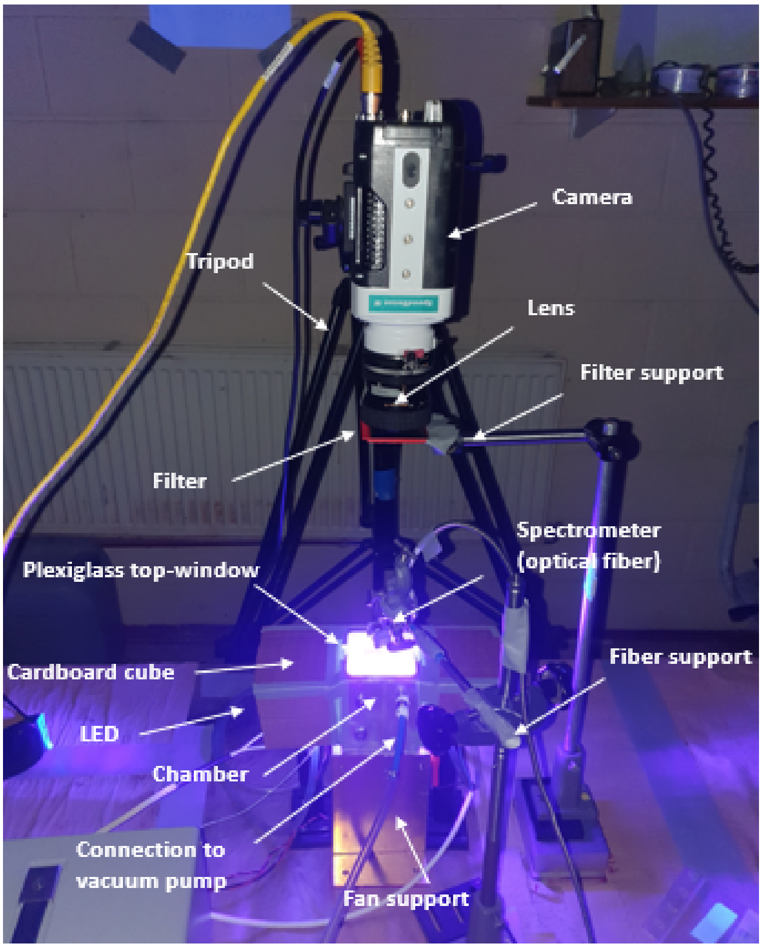

Figure 4.13: Assembly of the setup for PSP spectrometry and calibration

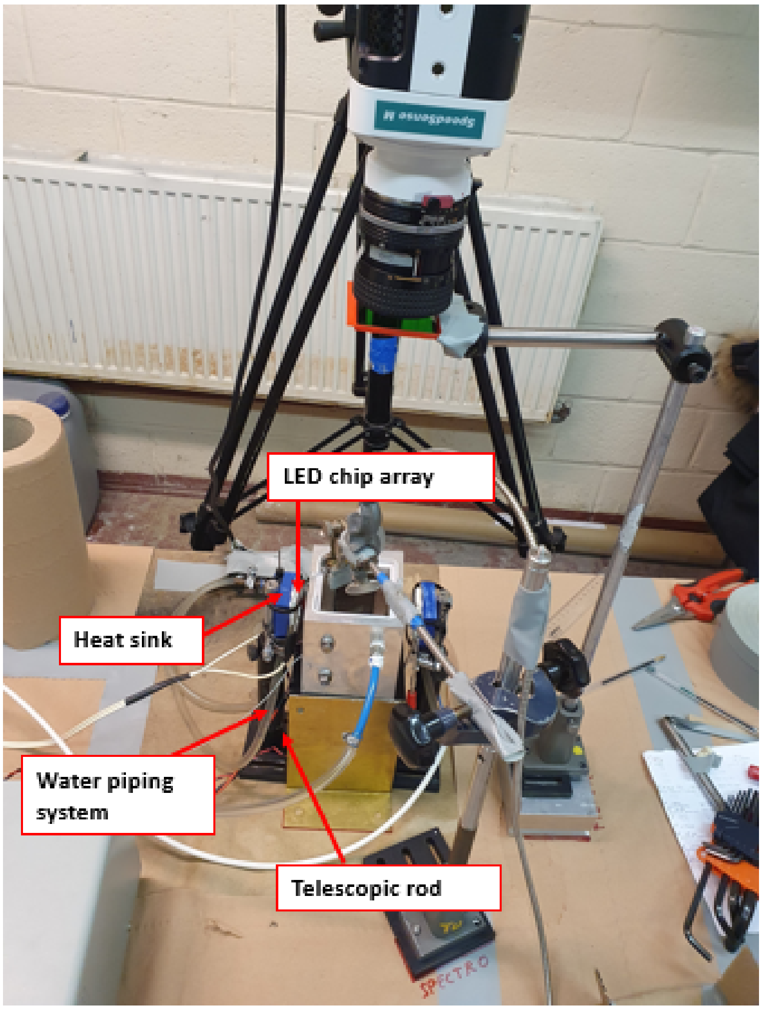

Figure 4.14: Detail of the illumination system - Assembly of the setup for PSP spectrometry and calibration

Chapter 5

Preparation and Experimental Testing

In this chapter the implementation of the setups and the several testing procedures are presented. Two intermediate calibrations are firstly needed to correlate the temperature of the model to the external power conditions. This stage includes several tests and the homogeneity of the temperature over the sample is confirmed by an infrared optical analysis. Once the paint has been applied on the sample (which requires a detailed safety procedure), two spectrometric analyses in combination with the final calibration of the PSP can be carried out. Finally, a theoretical design of the next steps for the conclusion of the rig measurement chains of PSP measurements in S-1/C is briefly discussed.

5.1 Intermediate calibrations

Before moving to the a-priori calibration, which is fundamental for the knowledge of the Stern-Volmer curve between intensity and pressure at different temperature levels, two intermediate calibrations must be carried out. In a first stage, the thermocouple underneath the copper base of the test cell was calibrated. Afterwards, an experimental procedure was performed in order to find the relation between the power supplied to the Peltier cell and the temperature of the sample in the test chamber.

5.1.1 Calibration of the thermocouple

The output of this study is the determination of the calibration curve between the voltage signal supplied by the thermocouple and the temperature of the sensor placed in the copper plate. The 'Seeback effect' is a thermoelectric effect involved in the temperature - electric voltage coversion via the thermocouple. The thermocouple is composed of two junctions (hot and cold) at the ends of the device. The difference of temperature between the hot and the cold junction generates a voltage proportional to this temperature variation. For the calibration of this electrical device, an industrial oven was used. The copper base (with the 'hot' junction inside) was placed on a wooden block inside the oven. The cable was passed through a hole located on the top surface of the oven, properly insulating form the external environment by a polystyrene cap. The 'cold' junction of the thermocouple was connected to an amplifier and then to an A/D converter before reaching the computer. The digital electric signal was acquired via the software Labview and finally processed in

Matlab. A reference thermocouple was used to measure the air temperature in the oven directly, for making the comparison with the voltage signal. The sensor was positioned vertically and close to the top surface of the copper base. Figure 5.1 depicts the physical setup for the calibration of the thermocouple.

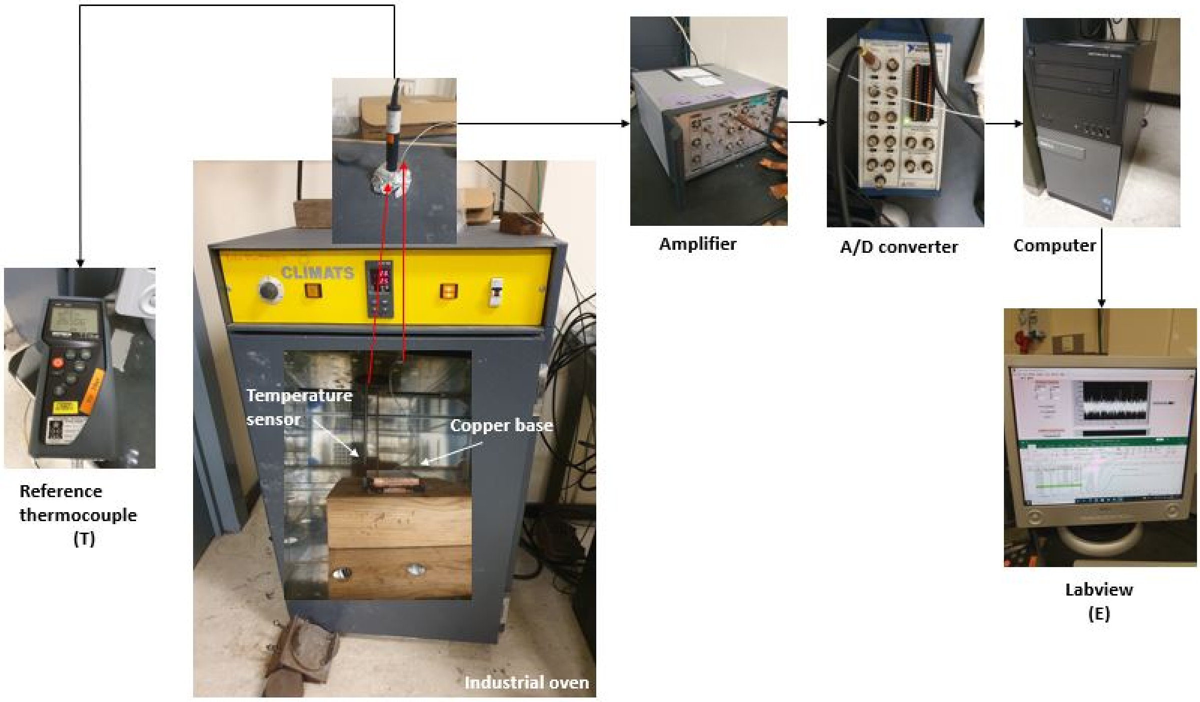

Figure 5.1: Schematic of the setup for the calibration of the thermocouple

The following list describes the assumptions made in the calibration.

- The temperature homogeneity of the copper plate is reached after two working hours of the oven at fixed temperature (set by the oven). The electic signal history processed in Excel via Labview showed a plateau region after 1.5 hours for each point (variations of the mean voltage signal below 0.02 V).
- After each two hours (at fixed temperature) for each point of the calibration curve, the thermal equilibrium between the the copper plate and the portion of the above air is reached.
- Oven ventilation effects were neglected. The fan was placed relatively far from the measurement area and the ventilation power was relatively low.

For each point, a 5-second acquisition was made, involving 5000 samples in the measurement with a frequency of 1000 Hz. Figures 5.2 and 5.3 show the data and reference temperature history, respectively. Data processing and the fitting of the output calibration curve are discussed in Chapter 6.

5.1.2 Calibration of the Peltier cell

The purpose of this calibration is the determination of the relation between the power supplied to the Peltier cell and the temperature of the sample inside the chamber. A similar setup described in

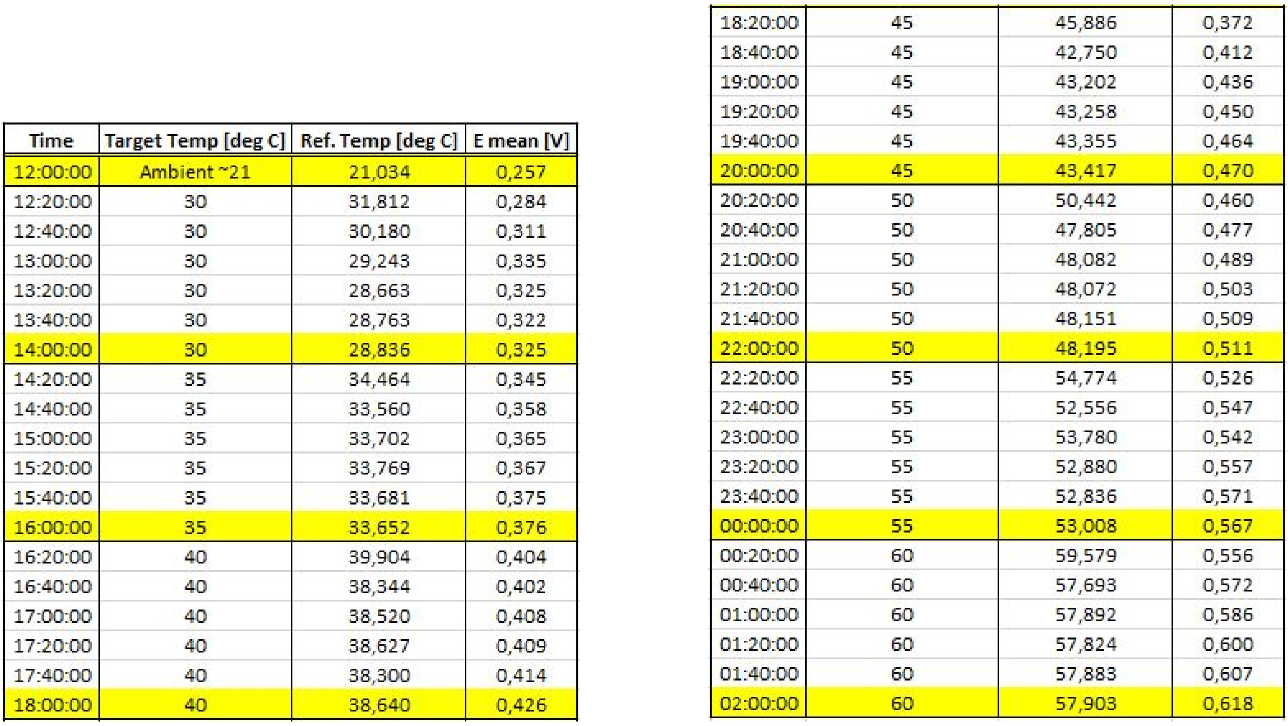

Time	Target Temp [deg C]	Ref. Temp [deg C]	E mean [V]
12:00:00	Ambient ~21	21,034	0,257
12:20:00	30	31,812	0,284
12:40:00	30	30,180	0,311
13:00:00	30	29,243	0,335
13:20:00	30	28,663	0,325
13:40:00	30	28,763	0,322
14:00:00	30	28,836	0,325
14:20:00	35	34,464	0,345
14:40:00	35	33,560	0,358
15:00:00	35	33,702	0,365
15:20:00	35	33,769	0,367
15:40:00	35	33,681	0,375
16:00:00	35	33,652	0,376
16:20:00	40	39,904	0,404
16:40:00	40	38,344	0,402
17:00:00	40	38,520	0,408
17:20:00	40	38,627	0,409
17:40:00	40	38,300	0,414
18:00:00	40	38,640	0,426
18:20:00	45	45,886	0,372
18:40:00	45	42,750	0,412
19:00:00	45	43,202	0,436
19:20:00	45	43,258	0,450
19:40:00	45	43,355	0,464
20:00:00	45	43,417	0,470
20:20:00	50	50,442	0,460
20:40:00	50	47,805	0,477
21:00:00	50	48,082	0,489
21:20:00	50	48,072	0,503
21:40:00	50	48,151	0,509
22:00:00	50	48,195	0,511
22:20:00	55	54,774	0,526
22:40:00	55	52,556	0,547
23:00:00	55	53,780	0,542
23:20:00	55	52,880	0,557
23:40:00	55	52,836	0,571
00:00:00	55	53,008	0,567
00:20:00	60	59,579	0,556
00:40:00	60	57,693	0,572
01:00:00	60	57,892	0,586
01:20:00	60	57,824	0,600
01:40:00	60	57,883	0,607
02:00:00	60	57,903	0,618

Figure 5.2: History of data for the calibration of the thermocouple. Target temperature points at ambient, 30°C, 35°C, 40°C, 45°C, 50°C, 55°C, 60°C. Two hours between consecutive points

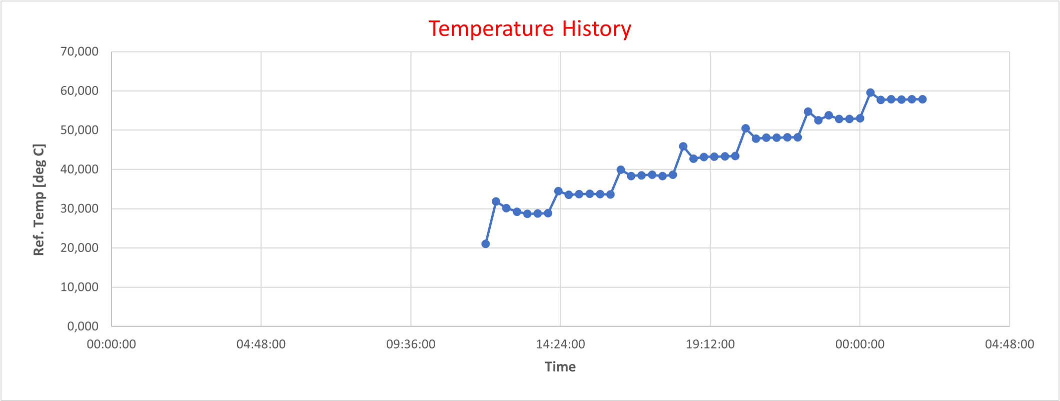

Figure 5.3: Reference temperature history

paragraph 4.3 was implemented. The Peltier cell is a thermoelectric device. It is basically a solid small plate heat pump. When a current passes through the electric conductors of the Peltier cell, one surface becomes cold and the opposite one becomes hot. This devise exploits the 'Seebeck effect' in a reverse way with respect to the thermocouple: the input voltage is now translated into temperature difference between the two surfaces. The hot side was attached to the copper base using a conductive paste. On the cold side, a fan + heat sink system was used to help the heat extraction, so as not to burn the Peltier. Conductive paste was used on both of the Peltier surfaces, in addition an insulating silicone paste was applied at the corners of the copper base to seal it from the external air. The thermocouple in the copper was connected to the system described in paragraph 5.1.1 for monitoring the voltage signal, hence the temperature. Inside the chamber, an aluminum sample with dimensions (50 x 50 x 2) mm was placed over the copper base. The hole for the vacuum pump access to the chamber was covered by insulating tape. The top plexiglass window was properly sealed with tape to reduce the heat exchange with the environment, and a hole in the middle of the top window was created to insert the temperature sensor of the reference thermocouple touching the aluminum surface. Figure 5.4 shows the setup scheme for the calibration of the Peltier cell.

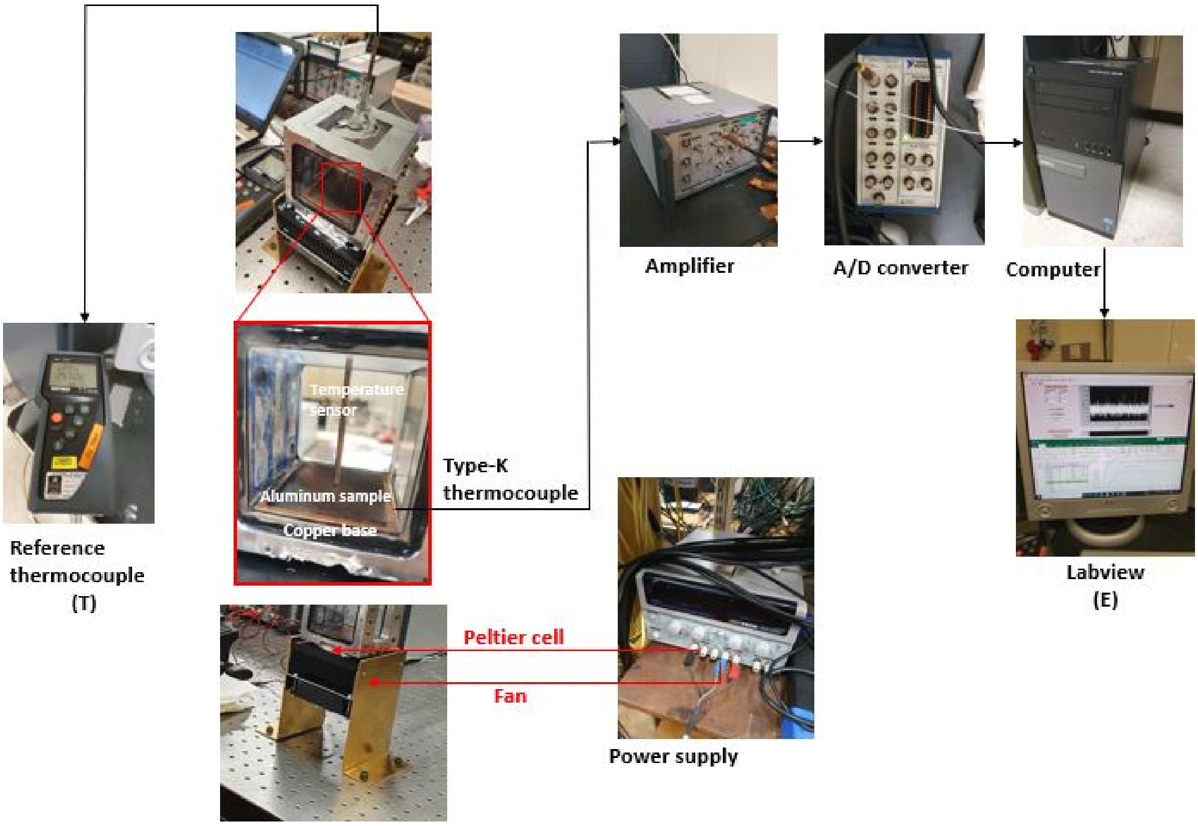

Figure 5.4: Schematic of the setup for the calibration of the Peltier cell

The voltage to the fun was fixed at 12 V, while the voltage supplied to the Peltier cell was varied between 0 to 10 V. The current knob was turned fully open so that the current value was autonomously adjusted by the electric circuit. The thermal stability of the of the type-K thermocouple was approximately reached after 1 hour at fixed power supply conditions (variations below 0.02 V of the voltage signal). Similarly to the thermocouple calibration in the industrial oven, for each point, a 5-second acquisition was made, involving 5000 samples in the measurement with a frequency of 1000 Hz. Figures 5.5 and 5.6 present the history of data for the calibration of the Peltier cell.

The analysis of data and the interpretation of the results are discussed in Chapter 6. Two additional tests were carried out to verify the validity of the results.

- Evaluation of temperature over the aluminum sample via an additional type-K thermocouple mounted on the model surface and insulated from the air in the chamber using tape. Thanks to this test, it was possible to verify the thermal stability between the copper plate and the aluminum sample by conduction, reducing the convective effects of the air inside the chamber (dominant in the previous calibration with the vertical sensor of the reference thermocouple)
- Evaluation of the air temperature inside the chamber using the vertical sensor of the reference

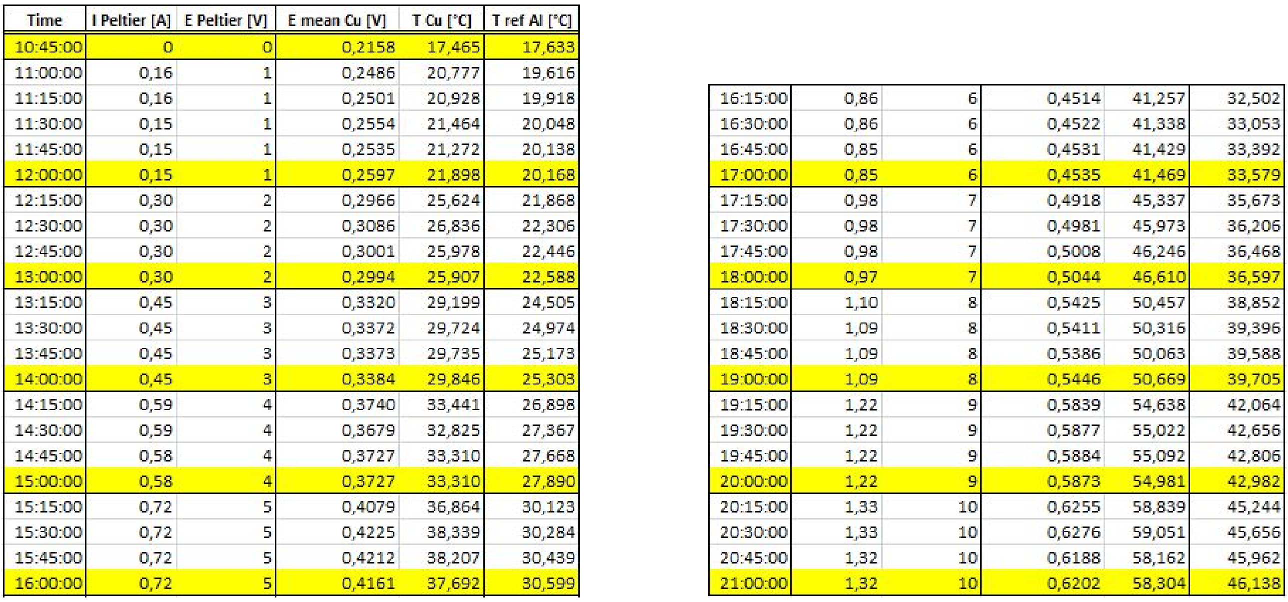

Time	I Peltier [A]	E Peltier [V]	E mean Cu [V]	T Cu [°C]	T ref Al [°C]
10:45:00	0	0	0,2158	17,465	17,633
11:00:00	0,16	1	0,2486	20,777	19,616
11:15:00	0,16	1	0,2501	20,928	19,918
11:30:00	0,15	1	0,2554	21,464	20,048
11:45:00	0,15	1	0,2535	21,272	20,138
12:00:00	0,15	1	0,2597	21,898	20,168
12:15:00	0,30	2	0,2966	25,624	21,868
12:30:00	0,30	2	0,3086	26,836	22,306
12:45:00	0,30	2	0,3001	25,978	22,446
13:00:00	0,30	2	0,2994	25,907	22,588
13:15:00	0,45	3	0,3320	29,199	24,505
13:30:00	0,45	3	0,3372	29,724	24,974
13:45:00	0,45	3	0,3373	29,735	25,173
14:00:00	0,45	3	0,3384	29,846	25,303
14:15:00	0,59	4	0,3740	33,441	26,898
14:30:00	0,59	4	0,3679	32,825	27,367
14:45:00	0,58	4	0,3727	33,310	27,668
15:00:00	0,58	4	0,3727	33,310	27,890
15:15:00	0,72	5	0,4079	36,864	30,123
15:30:00	0,72	5	0,4225	38,339	30,284
15:45:00	0,72	5	0,4212	38,207	30,439
16:00:00	0,72	5	0,4161	37,692	30,599
16:15:00	0,86	6	0,4514	41,257	32,502
16:30:00	0,86	6	0,4522	41,338	33,053
16:45:00	0,85	6	0,4531	41,429	33,392
17:00:00	0,85	6	0,4535	41,469	33,579
17:15:00	0,98	7	0,4918	45,337	35,673
17:30:00	0,98	7	0,4981	45,973	36,206
17:45:00	0,98	7	0,5008	46,246	36,468
18:00:00	0,97	7	0,5044	46,610	36,597
18:15:00	1,10	8	0,5425	50,457	38,852
18:30:00	1,09	8	0,5411	50,316	39,396
18:45:00	1,09	8	0,5386	50,063	39,588
19:00:00	1,09	8	0,5446	50,669	39,705
19:15:00	1,22	9	0,5839	54,638	42,064
19:30:00	1,22	9	0,5877	55,022	42,656
19:45:00	1,22	9	0,5884	55,092	42,806
20:00:00	1,22	9	0,5873	54,981	42,982
20:15:00	1,33	10	0,6255	58,839	45,244
20:30:00	1,33	10	0,6276	59,051	45,656
20:45:00	1,32	10	0,6188	58,162	45,962
21:00:00	1,32	10	0,6202	58,304	46,138

Figure 5.5: History of data for the calibration of the Peltier cell. Voltage supplied from 0 to 10 V. One hour between consecutive points

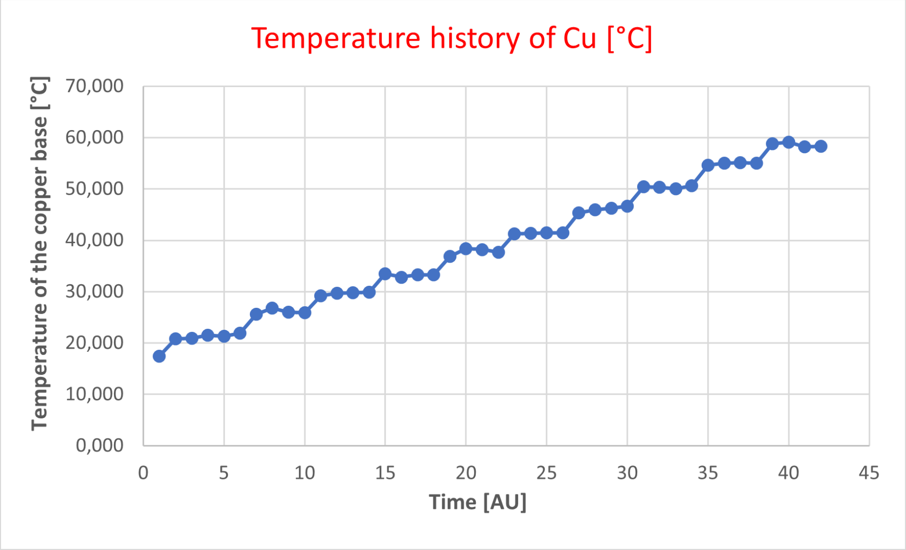

Figure 5.6: Temperature history of the copper base

thermocouple close to the aluminum sample. In this test the convection between the sensor bar and the surrounding air is dominant, and the thermal equilibrium is not reached before several hours at fixed power conditions.

5.2 Infrared analysis

An IR camera was used to verify the homogeneity of temperature of the whole aluminum top surface after one hour at fixed power conditions by the Peltier cell. The setup was similar to that one of the Peltier cell calibration. The infrared camera FLIR SC3000 was placed over the chamber pointing downwards to the aluminum sample via a tripod. The minimum focusing distance of 300 mm allowed to obtain max resolution images. Due to operation condition at low temperatures, the metal surface was evenly painted by a black paint with high conductivity. However, the use of a black paint with high emissivity, which was not present at VKI, would have been necessary to reduce ambient light reflections for more accurate results. The mirror, firstly designed, was decided to remove because of the unknown transmission properties in the infrared spectrum. For each data point, the plexiglass window was removed, which otherwise would have absorbed the infrared light. Due to this approximations, it was not possible to use the infrared analysis as a means to evaluate precisely the temperature of the sample in each point, but it was implemented for the investigation of temperature homogeneity through an object signal (OS) of the IR camera in each pixel of the detected images, which is proportional to the irradiance. The thermocamera acquired 10 images for each measurement with a frequency of 0.5 Hz. Image-processing and scatter of results are discussed in Chapter 6.

Figure 5.7: View of the setup for IR analysis (the image does not represent the real implementation of the setup, but it shows only a qualitative view)

5.3 Paint application procedure

Because of the solvent toxicity of the paint, a special safety procedure for the application over the sample must be followed. As discussed in Paragraph 2.4.3, the safety equipment must include a filtered mask, safety eyewear, safety suit, gloves, and additional tools. In particular, the equipment used for the spraying of the sample is listed below.

- Filtered mask: 3M Reusable Half Mask with filter 6055
- Safety eyewear: uvex i-works, anti-fog/scratch coating
- Safety suit: Asatex Chemical Protective Overall, Category III
- Gloves: nitrile powder free

The paint application procedure consists of three phases: the preparation of the setup, the application of the paint (both basecoat and active layer), and the post-painting. The painting was performed in a specific equipped laboratory, which has an intake duct to suck the spray gun fumes, an air compressor which was necessary to set the right pressure to the spray gun, and all the windows were covered by dark plastic sheeting aims at reducing the ambient light which otherwise would enhance the photo-degradation of the PSP. The spray gun and the aluminum sample were firstly cleaned with acetone, and the 'painting area' was properly covered using paper, cardboard and a large transparent plastic sheeting was used to divide the painter from the toxic emissions (see Figure 5.8). Before pouring the needed quantity of basecoat/PSP into the spray gun, the cans were shaken thoroughly for several minutes. The instructions for the application of the paint provided by ISSI were considered for the settings regulation of the spray gun.

- Air pressure at 0.5 bar
- Fluid control knob almost full open to get a sheet pattern which yields more uniform results over a square sample

Figure 5.8: View of the 'painting area'

The gun was kept 30 cm away from the sample while spraying. According to the dimensions of the aluminum sample of (50 x 50) mm, 2-6 cross light coats were sprayed for each coat. The number of coats, instead, varied according to the coverage obtained. For this paint application, 8-10 for the basecoat and 12-14 for the PSP were considered sufficient to reach a good uniformity. The paint was allowed to dry between coats (around 10 s, recommended by the instructions).
The post-painting included the disposal of the remaining paint into the gun, cleaning the gun with acetone and throwing away all dirty objects. The hands was washed thoroughly with soap and water after each paint application. The sample was left to dry for at least one hour in a dark ventilated area (both after the application of the basecoat and the PSP). Finally, the dried sample, which was no longer toxic because of the evaporation of the solvent, was moved into a dark box to avoid ambient light and heat cured at 75°C for two hours in a ventilated industrial oven.

5.4 Spectrometric analysis

The aim of the spectrometric analysis is the verification of the emission spectrum of the PSP, when excited by the LEDs. The final purpose is twofold: a static spectrometry shows the two emission wavelength ranges necessary for the best selection of the optical filters; while a more detailed analysis verifies the PSP behavior under different pressure and temperature conditions inside the chamber. The Spectrometer Ocean Optics HR4000CG-UV-NIR was used in combination with an optical fiber. Data were acquired via the software OceanView, saved as text file and sent to Matlab for post-processing. The setup for both the spectrometric analyses is shown in Figures 5.9 and 4.13.

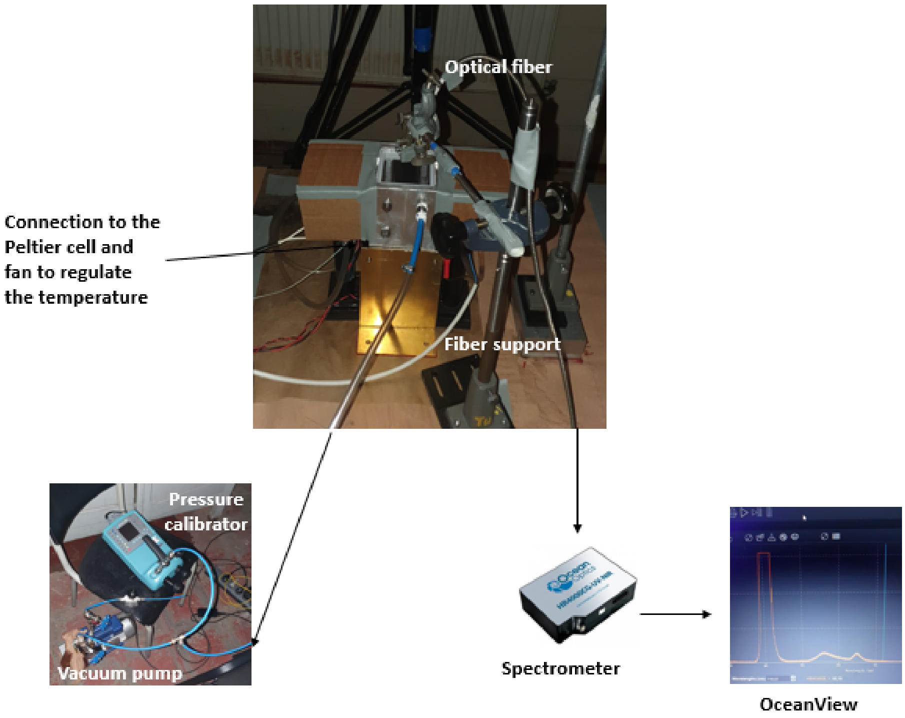

Figure 5.9: Schematic of the setup for the spectrometry

5.4.1 Static spectrometry

The plexiglass window did not influence significantly the intensity of the spectro-graph. The optical fiber and the two LED chip arrays was positioned as close as possible to the model surface, supported by an optical rod system. This enhanced the SNR of the spectrometer. A good compromise between high emission intensity recorded and background noise determined an integration time of 1 s, and only one scan at a time was acquired to reduce the photodegradation time of the PSP while under illumination. An option in the acquisition software was selected to subtract autonomously the dark electric noise of the spectrometer from the data. The testing procedure for the static spectrometric analysis is listed below.

- A first reference dark scan was acquired while all the ambient lights were switched off.
- The water circuit and the LEDs were switched on
- Another scan was acquired with no filters between the plexiglass top-window and the fiber
- The water circuit and the LEDs were switched off

The post-processing and result of this analysis is shown in Chapter 6. Based on the emission spectrum, a few filters (red and green - pass) were analyzed among the ones available at VKI. A similar static procedure was repeated to assess the validity of the chosen filters. Therefore, the filters were placed between the plexiglass window and the optical fiber. The use of filters reduces the SNR of the photodetector, especially when they have a low transmission in the 'pass' range. For this reason the integration time was increased to 10 s (the background noise increased accordingly).

5.4.2 Temperature-pressure dependent spectrometry

A similar setup was prepared for the temperature-pressure dependent spectrometric analysis. In this case, both the temperature and pressure were varied in order to detect the differences in the emission spectrum of the PSP. The relative pressure (subtracted from the environment) of the chamber was varied among 7 fixed values. Data interpolation was performed by firstly decreasing the pressure every fixed interval, and then increasing the pressure level again covering the mid points of the intervals. The maximum and minimum relative pressure reached by vacuum the pump was -630.0 mbar and -900.0 mbar, respectively. The temperature variation was analyzed for three levels changing the voltage supplied to the Peltier cell (0 V, 2 V, 4 V), which was previously calibrated to determine the temperature value. For each 'temperature set', a new reading of the ambient pressure was needed to know the absolute pressure inside the chamber. The following table shows the matrix of the measurement points.

This analysis presents the same settings of the static spectrometry in terms of integration time, scans to average, position of the optical fiber, elimination of the dark current noise and no filters between the chamber top-window and the fiber. The procedure for the acquisition of the emission spectra under different conditions is herein described.

$T - T_{ambient}$ [°C]	0	8.523	16.047
P_0 [kPa]	99.95	100.08	100.08
P_1 [kPa]	35.05	34.98	34.98
P_2 [kPa]	30.05	29.98	29.98
P_2 [kPa]	25.05	24.98	24.98
P_2 [kPa]	20.05	19.98	19.98
P_2 [kPa]	15.05	14.98	14.98
P_2 [kPa]	10.95	10.78	10.78

Table 5.1: Matrix of the measurement points. Temperature of the sample - Absolute pressure in the chamber

- A first reference dark scan was acquired while all the ambient lights were switched off.
- The water circuit and the LEDs were switched on
- A scan was acquired (ambient pressure P_0)
- The LEDs were switched off
- Ventilation of the room was activated to remove the fumes from the vacuum pump
- The vacuum pump was switched on
- The reading of the ambient pressure was recorded and consequently the vacuum pump reference pressure was set to zero
- The chamber pressure was regulated to the desired value from the pump and read on the pressure calibrator
- The LEDs were switched on
- A scan was acquired
- The LEDs were switched off
- The process continued until the last desired pressure value
- The vacuum pump and the room ventilation were switched off

This list represents the acquisition procedure for a single temperature set. The voltage supplied to the Peltier cell was then varied to the desired value. After approximately one hour, once the thermal equilibrium was reached, the same procedure was repeated for a new temperature set.

5.5 Calibration testing of the PSP

The output of the calibration of the paint is the determination of the Stern-Volmer equation. The setup, similar to the spectrometric analysis, is presented in Figures 4.12, 4.13 and 4.14. The same temperature and pressure points of the matrix shown in Table 5.1 were followed. The painted aluminum sample was placed inside the calibration chamber using the gloves and carefully touching only the borders. A pair of pliers was then needed to position it precisely over the copper base. The settings of the camera adjusted via PCC Phantom are presented in the following table.

Resolution [px]	1280 x 800
Sample rate [fps]	50
Exposure time [μs]	2000
Number of acquired images per set [-]	10
Bit depth [bit]	16

Table 5.2: Camera settings from PCC Phantom used during the calibration

This specifications were selected in order to maximize the quality of the steady-state images in terms of spatial resolution, color intensity and brightness, while not saturating the intensity (especially at the minimum pressure level) and reducing the file dimensions. The procedure for the acquisition of the images is listed as follows.

- Firstly, two sets of reference dark frames with the green and red filter were acquired while all the ambient lights were switched off.
- The water circuit and the LEDs were switched on
- A set of images were captured with the green filter on (ambient pressure P_0)
- The LEDs were switched off
- The filter was rapidly changed to red
- The LEDs were switched on to record the same set of images with the red filter, then the LEDs were switched off again
- The same procedure presented during the spectrometric analysis was followed for the use of the vacuum pump and the regulation of the pressure inside the chamber
- For all the pressure levels, the LEDs were switched on to acquire a new set of images, and then they were switched off again (twice: using the green filter and the red filter at each pressure point)
- The whole procedure was repeated for a new temperature point. The calibration ended when all the images of the temperature sets were recorded

The images were saved as Phantom cine files in 16-bit quality and then transferred to Matlab for post-processing (Chapter 6).

5.6 Design of the procedure for testing in S-1/C

In order to minimize the the final measurement uncertainty an in-situ calibration should be carried out. It is basically a correction of the raw a-priori calibration in which the image intensity are directly compared to the readings from the pressure taps. The temperature effect can be compensated by acquiring the model temperature inside the facility using either temperature sensors, combined use of TSP, infrared analysis or an estimation via numerical simulation. Considering the implementation in S-1/C, the easiest way to measure the surface temperature of the model can be performed by the following two ways:

- Infrared analysis.
  This analysis gives the most accurate results. However, the thermocamera must be properly a-priori calibrated to determine the correlation between OS and temperature. The limitation is the application at low temperature, close to ambient, which reduces the SNR of the camera. Moreover, a high-emission black paint should be evenly applied on the model surface to reduce the ambient light reflections, and the glass window of the optical access needs to reach a high transmission in the infrared wavelength spectrum.

- Numerical simulation.
  The static surface temperature can be estimated by applying the adiabatic wall model, knowing the recovery factor of the local boundary layer profile, the total temperature, the flow Mach number and the specific heat. Nevertheless, this method aims at giving only an estimation of the real surface temperature.

Once the corrected calibration curve between pressure ratio and intensity ratio at different temperatures is obtained, the measurement of the steady-state static pressure over the model surfaces under nominal flow-on conditions of the facility can start. The sketch of the setup is shown in Figure 4.10. When an optical access is used, the remaining windows need to be closed. The main points of the testing procedure are summarized below.

- The pressure inside the facility is set to the reference pressure
- Two sets of dark reference frames are captured (ambient lights off, both with the red filter and the green filter)
- The water circuit for cooling down the illumination system is activated
- Two sets of wind-off images are recorded changing rapidly the filters (between each two sets, the LEDs have to be switched on and off again to reduce the photo-degradation of the PSP)
- Flow was established in the test section, reaching the nominal conditions and approximately one hour is needed to reach a fairly stable temperature to further minimize the temperature effect (see Paragraph 3.5.1)
- Two sets of wind-on images are detected using both the optical filters

- The water circuit, the facility are switched off and the setup can be moved to another optical access for a new measurement acquisition campaign (e.g., detecting the static pressure mapped onto the bottom endwall of the cascade)
- All the images and data are saved and post-processed in Matlab (Chapter 6)

Chapter 6

Data-Processing, Results and Assessment

This chapter deals with the post-processing procedures after data acquisition and with the investigation on the obtained results. Firstly, the intermediate calibration results are discussed, which include the study of the temperature variations involving the thermocouple, the Peltier cell and the sample. Two spectrometric analyses follow, which are essential for the preparation to the final calibration. The latter is finally discussed, showing the calibration curves of the PSP, the Stern-Volmer equations and a uncertainty analysis for the determination of the calibration parameters. An insight on the future post-processing design of data acquired from testing in the facility is then presented.

6.1 Calibration of the thermocouple

After having acquired the digital voltage signal from the software Labview, the data were processed in Matlab. A filtering code, presented in Appendix B, was implemented. A low-pass filter frequency of 20 Hz was selected, reducing the high-frequency background noise. For each temperature point (from ambient to 60°C), the code provides three graphs:

- Filtered vs raw signal as function of the acquisition time ($5\ \mathrm{s}$).
- Single-side amplitude spectrum of the filtered signal.
- Data dispersion by histogram which shows the occurence as function of the variation from the mean filtered value. The graph also provides the normal distribution that fits the data.

An example is shown in Figure 6.1 .The remaining graphs are reported in Figures A.1 and A.2.

The Matlab script also displays the mean voltage of the filtered and signal and its uncertainty. Table 6.1 and the plot in Figure 6.2 present the results for the fitting.

The linear equation of the fitting is the following.

$$T = 100.987201\, E_{mean} - 4.328389 \tag{6.1}$$

with a coefficient of determination $R^2 = 0.999067$.

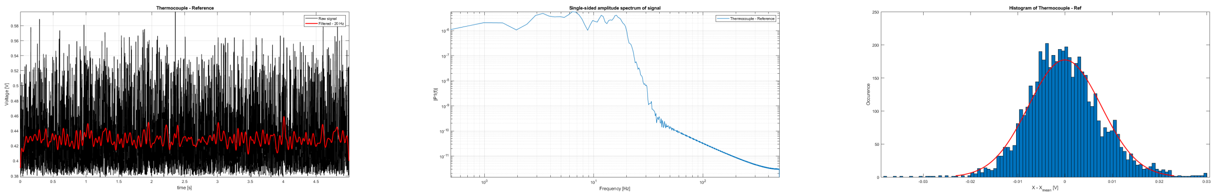

(a) **(b)** **(c)**

Figure 6.1: Calibration of the thermocouple 40°C - Raw and filtered voltage signal (left). PSD of the filtered signal (middle). Histogram of filtered data (right)

Target T [°C]	Filtered E mean [V]	Uncertainty E [$\times 10^{-5}$ V]	Ref. T [°C]
21	0.2530	10.24	21.034
30	0.3253	7.932	28.836
35	0.3760	8.692	33.652
40	0.4290	10.90	38.640
45	0.4749	12.63	43.417
50	0.5122	8.984	48.195
55	0.5703	9.702	53.008
60	0.6173	12.80	57.903

Table 6.1: Results of the calibration of the thermocouple

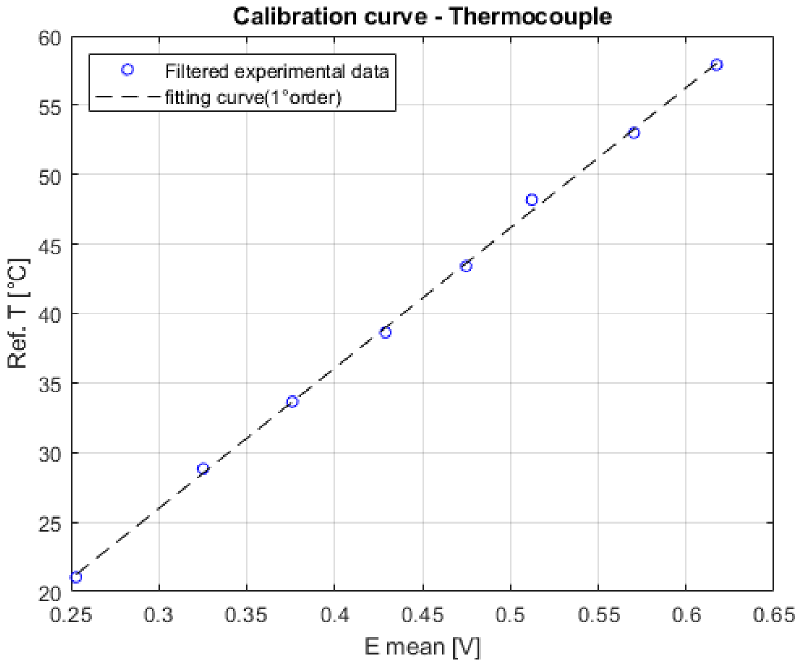

Figure 6.2: Fitting of the experimental data

6.2 Calibration of the Peltier cell

Similarly to the previous calibration, the voltage signal of the thermocouple acquired by Labview was filtered and processed in Matlab via the code in Appendix B. The statistics of filtering are reported in

Figures A.3 and A.4. The results are presented in Table 6.2 and in Figure 6.3. The determination of the copper base temperature was performed implementing the linear equation found in the previous calibration. Accordingly, the aforementioned equation was involved in the error propagation for the determination of the uncertainty of the copper temperature.

E Peltier [V]	T Cu filtered [°C]	Uncertainty T Cu [$\times 10^{-2}$ °C]	Ref. T Al [°C]
0	17.606	0.92088	17.633
1	22.049	1.5001	20.168
2	26.129	1.5528	22.588
3	30.108	1.2659	25.303
4	33.653	1.3885	27.890
5	38.177	1.4946	30.599
6	42.715	1.2019	33.579
7	46.610	1.3741	36.597
8	51.679	2.0943	39.705
9	55.466	1.4540	42.982
10	59.061	1.3151	46.138

Table 6.2: Results of the calibration of the thermocouple

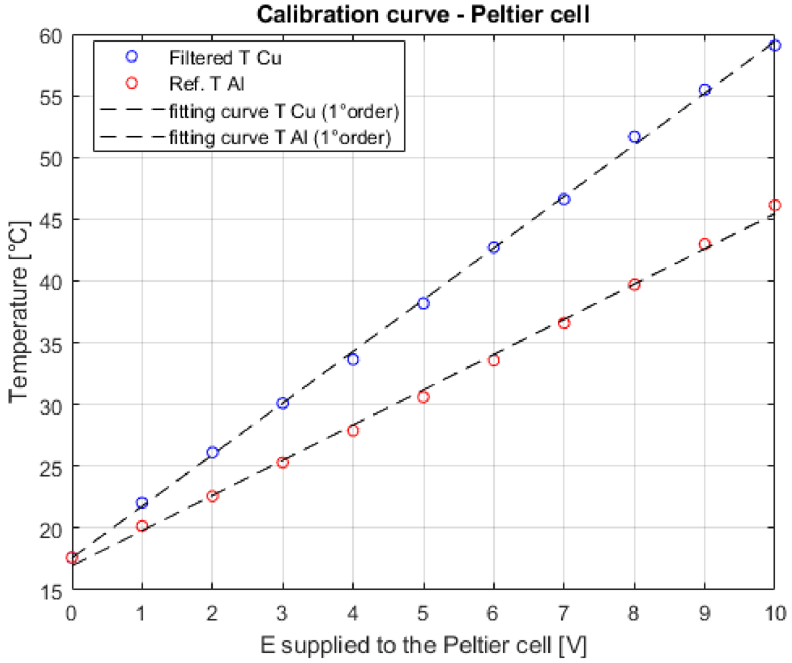

Figure 6.3: Fitting of the experimental data

As discussed in Paragraph 5.1.2, the temperature of the aluminum sample acquired by the reference thermocouple is strongly sensitive to the convective effects of the surrounding air. Therefore, the experimental data are evidently lower than the data of the copper temperature. The thermal equilibrium would have taken several hours at fixed power conditions, which is not possible when performing a 10-point calibration. Two additional assessments were carried out to verify this assumption.

- Verification of the top surface temperature of the aluminum sample by an additional type-K thermocouple. The air convection effects were reduced covering the sensor over the aluminum plate by insulating tape, and the thermal stability by convection between the two metals was reached before one hour at fixed power conditions. The voltage signal was filtered and translated into temperature by a previous static calibration. After one hour for each point of the curve, the maximum temperature difference between the copper and the aluminum plates was below 0.5 °C.
- Determination of the air temperature inside the calibration chamber by the reference thermocouple. The sensor was inserted vertically and positioned near the upper surface of the aluminum sample. The dominant convective effects and the non - thermal equilibrium reached in less than one hour resulted in the detection of a temperature which was even lower than the red dotted line shown in Figure 6.3.

For this reasons, only data obtained by the type-K thermocouple were considered for the calibration of the Peltier cell. The fitting linear equation (blue dotted line in Figure 6.3) is presented below.

$$T = 4.178559\, E_{supplied} + 17.583458 \tag{6.2}$$

with a coefficient of determination $R^2 = 0.999328$.

where $E_{supplied}$ is the voltage supplied to the Peltier cell (with current automatically regulated by the circuit) and T represents the copper temperature, taken as a reference for the next experiments (which is slightly higher, less than 0.5 °C, from the aluminum top surface temperature after one hour at fixed power conditions, as discussed above).

6.3 Infrared analysis

The infrared analysis was necessary for the assessment of the temperature uniformity over the aluminum surface, which was black painted to enhance its emissivity thus reducing the reflection from the ambient light especially for low-temperature measurements. The detected images by the thermocamera were sent to Matlab for post-processing. The image processing procedure (code in Appendix B) involves the following main steps.

- Averaging of the 10 images (acquired with a frequency of 0.5 Hz)
- Size reduction to the ROI of interest
- Mean and dispersion of the pixel intensity values for each image array

20 s of recording was necessary to average the small unsteady variations of the camera, because of both its high sensitivity and the reflections of the ambient light on the metal surface. The cropped image arrays had a resolution of (150x150) px, which was obtained thanks to the positioning of the

thermocamera as close as possible to the sample (at minimum focusing distance, approx. 300 mm). To reduce background noise, the borders of the aluminum sample near the copper base (not black painted and with high ambient light reflection) were discarded from the statistic analysis. Figure 6.4 shows a comparison between the full-field image and the cropped image.

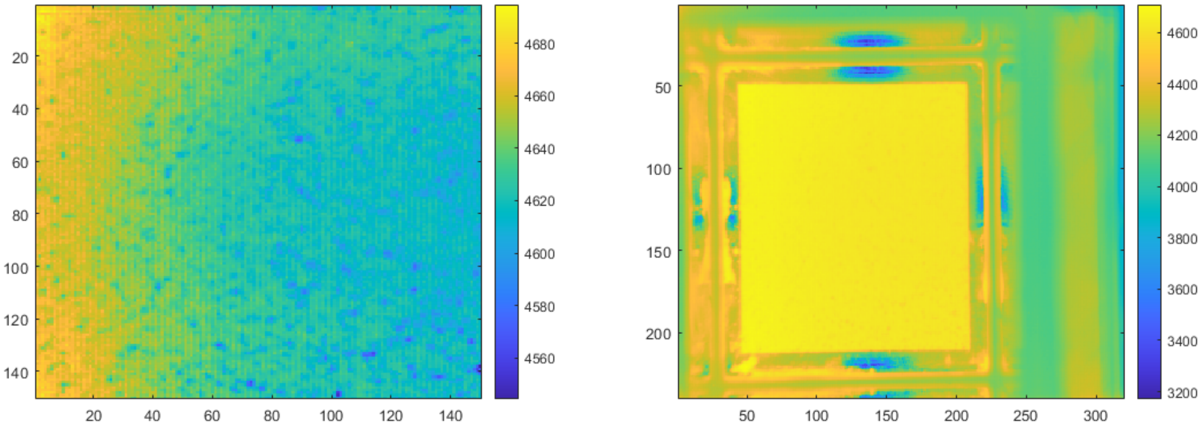

(a) **(b)**

Figure 6.4: Infrared images at 4 V (arbitrary intensity unit [OS]). Comparison between cropped image (a) and full-field image (b)

As discussed in Paragraph 5.2, the images were acquired in [OS], an arbitrary object signal determined by the camera settings and proportional to the irradiance on the pixels. Because of the low-temperatures, metal surfaces not covered by a high-emissivity black paint, the ambient light reflections, and the removal of the plexiglass top-window for each measurement, the precise acquisition of temperature could not be performed. However, the scope of the infrared analysis was only the verification of the temperature (or OS) uniformity over the sample when heated up for one hour by a Peltier cell at fixed power conditions. For this reason, a statistic analysis concerning the dispersion of the averaged pixel signal was carried out. The results are presented in Table 6.3 and in Figure 6.5.

As expected, both the mean value and the standard deviation increase at higher supplied voltage. Figure 6.6 shows a comparison between two images (1 V and 5 V). The remaining processed images are reported in Appendix A (Figures from A.5 to A.8).

The OS of the images is randomly distributed over the whole metal surface. The systematic error at the left of the images (slightly higher OS) is due to ambient light reflections. It was changing while moving the calibration chamber with respect to the thermocamera and it was not possible to eliminate. This effect can be also noted in the first infrared image at ambient temperature, in which the temperature was assumed to be homogeneous over the model surface. Figure 6.7 shows how the difference between an infrared image (5 V) and the corresponding one at 0 V supplied does not depend anymore of the systematic error.

Although the determination of the temperature field can not be obtained because of the issues presented above, a quick analysis was carried out taking into consideration the temperature calibration of the camera itself. Following the same post-processing procedure, the mean temper-

E Peltier [V]	Mean value [OS]	Standard deviation [OS]
0	3547.4	15.350
1	3814.9	16.084
2	4033.5	16.829
3	4310.7	17.404
4	4632.9	18.622
5	4933.1	19.375
6	5274.0	20.992
7	5644.9	24.808
8	6023.4	28.419
9	6390.7	29.466
10	6805.9	34.429

Table 6.3: Results of the infrared statistic analysis

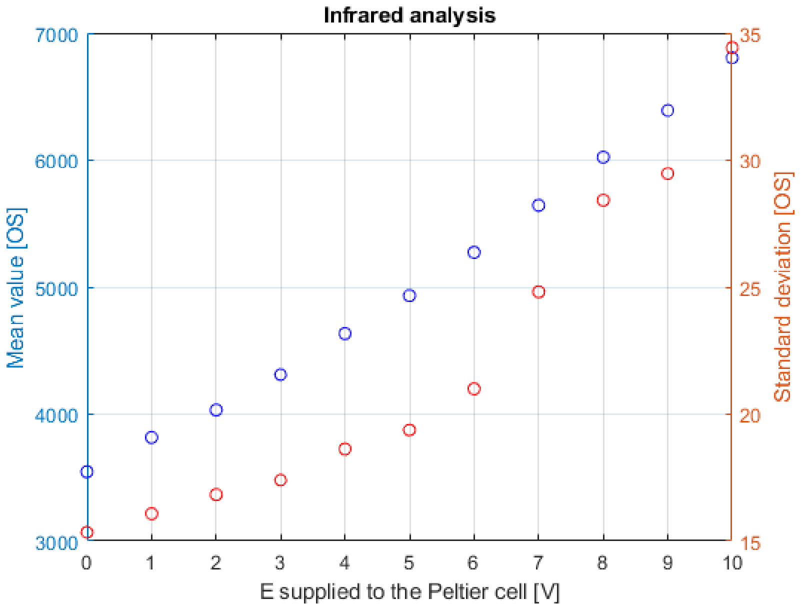

Figure 6.5: Infrared analysis. Mean value and standard deviation of the cropped images [OS]

ature values of the averaged images followed a linear relation with a coefficient of determination $R^2 = 0.999155$. The standard deviation was increasing at higher voltage supplied but kept below 0.3 °C. The absolute values of mean temperature and data dispersion does not represent the real conditions of the analysis, but the indicative value of the standard deviation combined with a direct verification of the OS dispersion through the infrared images can give an input regarding the temperature uniformity over the sample.

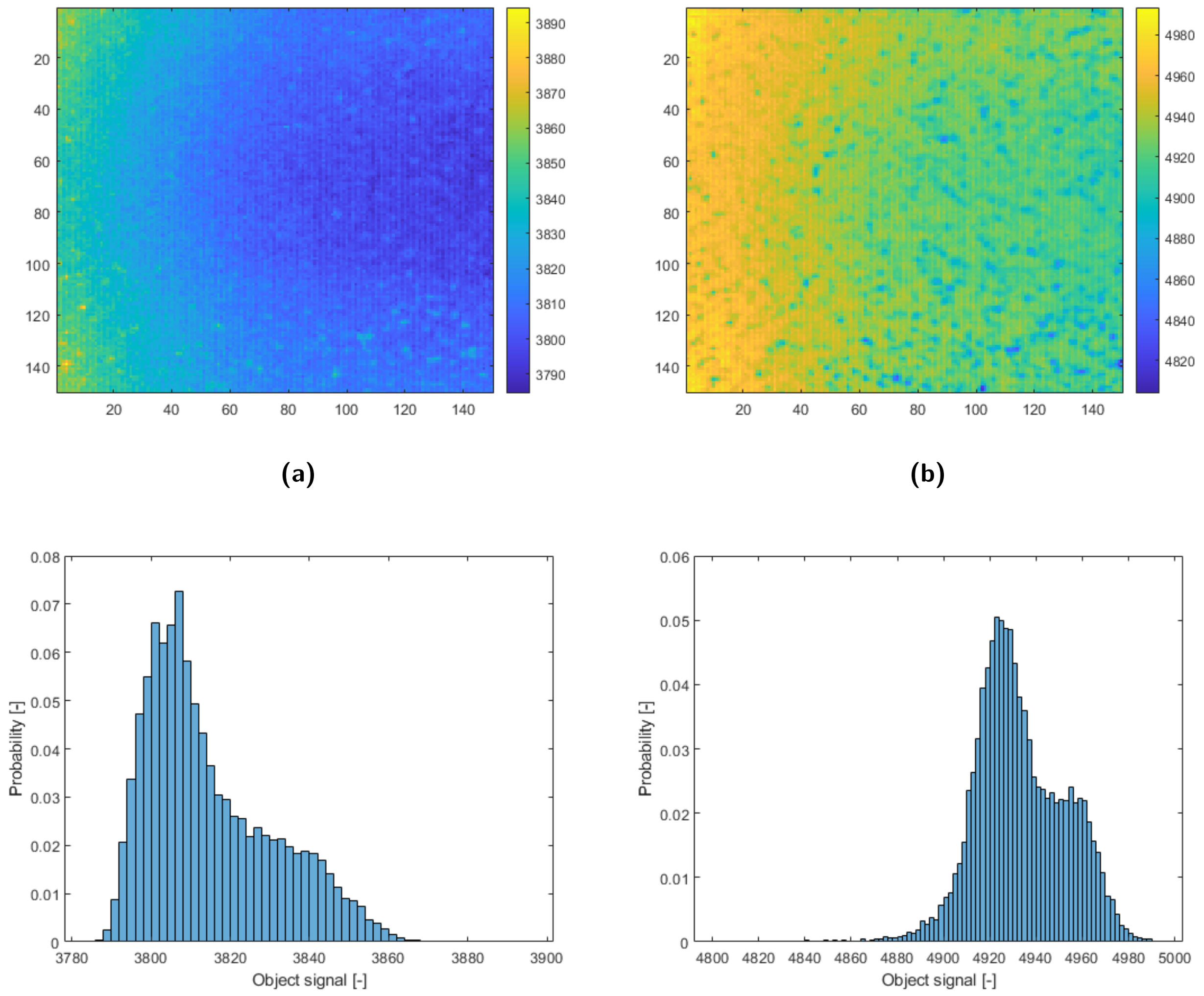

(a) **(b)**

(c) **(d)**

Figure 6.6: Scaled infrared images - 1 V (a), 5 V (b). Histogram of data - 1 V (c), 5 V (d).

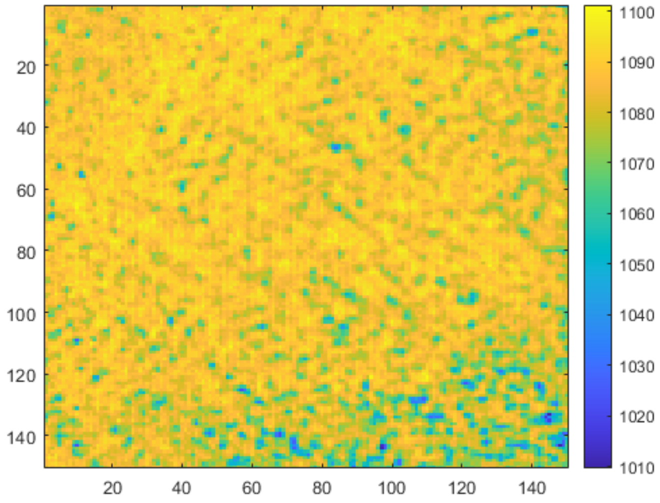

Figure 6.7: Infrared image at 5 V normalized to the reference ambient infrared image at 0 V [OS]

6.4 Spectrometric analysis

6.4.1 Static spectrometry

Before proceeding with the verification of the emission spectrum of the PSP under different temperature and pressure conditions, a first static analysis aims at verifying the wavelength ranges of the two luminophore-peaks for the choice of the optical filters. The data-processing (Appendix B) includes the elimination of the ambient background scan, acquired in a first stage. Dark current error was automatically compensated by the spectrometer when selecting the available option in OceanView. The spectral steady-state response of PSP under LED excitation at ambient pressure and temperature is shown in Figure 6.8.

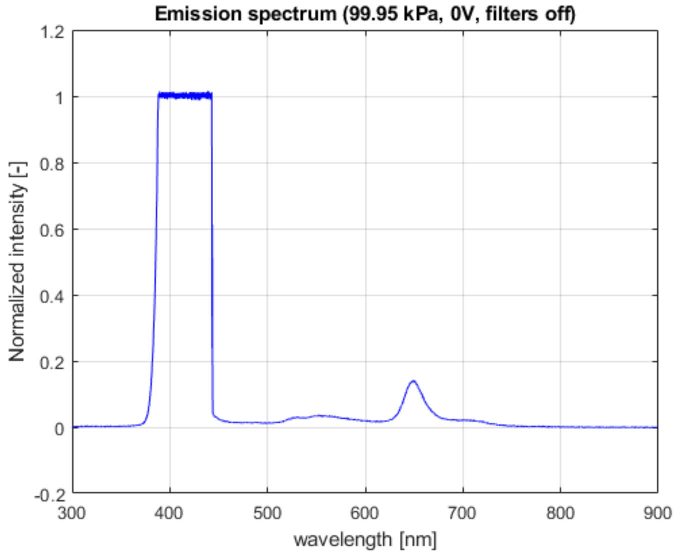

Figure 6.8: Emission spectrum at 99.95 kPa and $0\mathrm{V}$ with no optical filters

The wavelength ranges of the two luminophore responses are similar to the ones shown in Figure 4.1a by ISSI. The values of intensity mainly depend on the pressure conditions. At ambient pressure the luminescent emission is strongly quenched by the high concentration of oxygen (when compared to low-pressure conditions) and the red (top-right) peak responses with a lower intensity. Moreover, the integration time set to 1 s determines a low SNR but is more convenient for reducing the excitation time (and consequently photo-degradation time) of the PSP under illumination, which can represents an issue in a long experimental test campaign. Finally, the spectrometer was not previously calibrated, therefore the normalized intensity values of a specific spectrum peak relative to another peak is not necessarily proportional since the spectrometer can show a different sensitivity in intensity with respect to different wavelengths. However, the analysis was still useful to verify the wavelength interval of the peaks and the relative increase in intensity of the same peak under different pressure and temperature conditions, performed in the next analysis. According to the requirements specified in Paragraph 4.2.5, the best filters available in VKI for this application were chosen. Table 6.4 summarizes their properties.

The two filters were firstly tested by the spectrometer. In order to better distinguish their

Type	Size [mm]	Pass wavelengths [nm]	Max transmission [%]
Bandpass	50 x 50	650+/-10	60
Bandpass	50 x 50	540+/-50	50

Table 6.4: Specifications of the optical filters

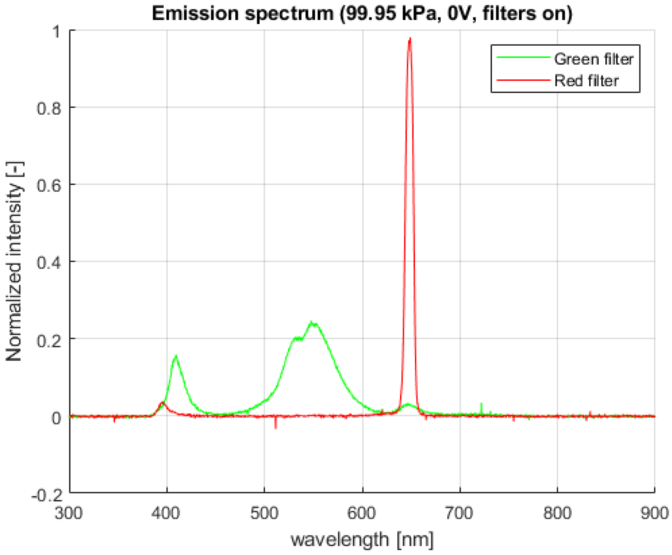

Figure 6.9: Emission spectrum at 99.95 kPa and $0\mathrm{V}$ with no optical filters

properties, an higher integration time (10 s) was selected in OceanView to enhance the SNR. Figure 6.9 presents their behavior. Both the filters have a very low maximum transmission in their pass wavelength intervals, therefore the two emission peaks are strongly reduced in terms of intensity output, consequently reducing the SNR of the camera during image acquisition. The red filter has a narrow peak (+/-10 away from the central value) compromising further the intensity output of the pressure-probe luminophore. However, it shows a decent optical density (even though a small peak around 400 nm correspondent to LED excitation is shown), especially compared to the green filter, absorbing the remaining wavelengths. The precise OD specifications were not provided. On the contrary, the green filter has a much larger pass wavelength interval and a lower OD. The excitation signal is not properly absorbed by the filter. This will influence the intensity of the images captured by the camera (they will be brighter when the green filter is on at relatively high pressure conditions), nevertheless it does not create a problem for the temperature sensitivity of the PSP. When computing the ratio of ratios between the two colors, the small excitation peaks do not depend on the increase in voltage supplied by the Peltier cell and the similar temperature dependency of the two luminophores can be divided producing a weak temperature sensitivity. Nonetheless, the small peak at approximately 650 nm in the graph when the green filter is used, means that the green filter does not absorb completely the main luminescent emission and the reference luminophore (green filter) images will not be insensitive to pressure anymore. Accordingly, the intensity ratio for the second luminophore emission is influenced by the pressure, and when computing the ratio of ratios the temperature sensitivity of the Binary PSP will even increases, strongly compromising the final results. The unavailability and the high cost for the proper filters forced the use of available filters in VKI, anyway the errors shown after the final calibration will be discussed and analyzed.

6.4.2 Temperature-pressure dependent spectrometry

This analysis was helpful to verify the behavior of the painted sample placed inside the calibration chamber, giving a larger view on the overall experiment and possibly some hints for the explanation of the final calibration results. The post-processing procedure was similar to the one used for the static spectrometry (code in Appendix B). Figure 6.10a shows how the probe luminophore was reacting at different pressures, while the reference luminophore is pressure-independent. Due to oxygen quenching, the lower is the pressure inside the calibration chamber, the higher is the intensity response of the PSP. The temperature sensitivity effect is presented in Figure 6.10b (only three values of pressure are reported for clearness of the results, however the overall trend is consistent for all the pressure points). For several values of pressure, the temperature increase results in a lower intensity output, due to thermal quenching of luminescence according to the Arrhenius relation (2.11).

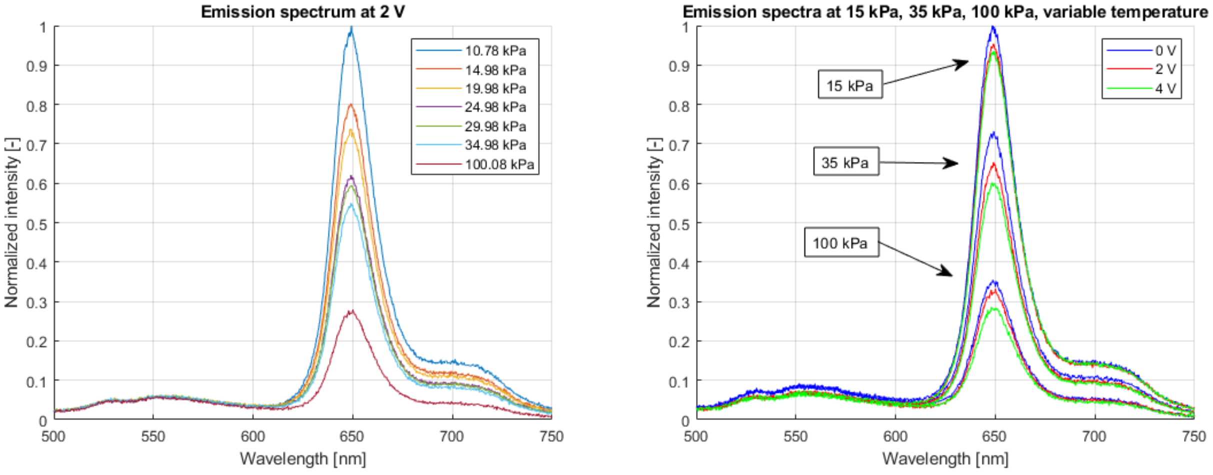

(a) **(b)**

Figure 6.10: Spectrometry - Pressure and temperature sensitivity. Emission spectrum at constant temperature (0 V) with variable pressure (a). Emission spectra at constant pressure (15 kPa, 35 kPa, 100 kPa) and variable temperature (b)

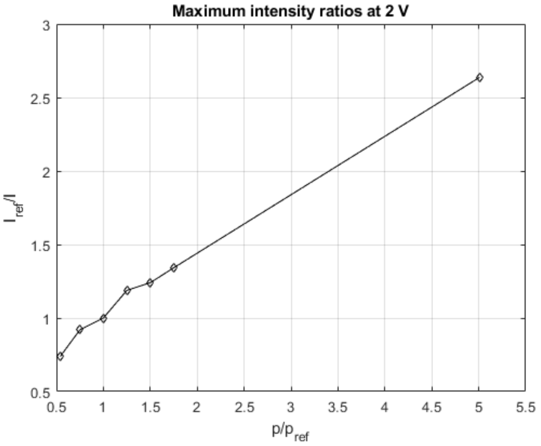

Figure 6.11: Curve of the maximum intensity ratios (probe luminophore) at constant temperature (2 V)

These results are not affected by the low quality of the optical filters. They represent the direct emissions of the painted aluminum model positioned inside the test cell. The influence of the plexiglass top-window of the chamber was verified to be negligible in the output intensity detected by the instrument. Nevertheless, the spectrometric analysis was influenced by the pressure leakages for the measuring points during which the vacuum pump was active. The error caused by the difference between the real pressure in the chamber and the measured pressure by the calibrator was dominant and it will be better displayed and discussed after the results of the final calibration. Figure 6.11 shows the trend of the intensity ratios at fixed temperature as function of the pressure ratio. The values were determined considering only the maximum points of the 'red' (probe luminophore) peaks. This gives a hint for the calibration of the PSP described in the next section.

6.5 Calibration of the PSP

The following procedure was followed for image-processing.

- File loading.
  All the images saved in 16 bit were loaded in Matlab. They were translated into 'double' format to allow for mathematical operations with frames.

- Frame cropping.
  The frames were firstly cropped, selecting the ROI for the analysis of the results. Figure 6.12 shows the passage for the selection of the processed region. The final frames have a resolution of (100 x 100) px, which corresponds to the central squared area (12 x 12) mm of the painted plate. In this case, the low resolution is not determinant for the calibration of the PSP, on the contrary smaller dimensions of the frames guarantee more reliable results. However, the magnification of magnification factor of 0.17, guaranteed a resolution of the images able to distinguish pressure differences every 0.12 mm in the two axes, which is much lower than the distance between two adjacent pressure taps in S-1/C. The cropping rate was chosen based on the variability of the average frame intensity and standard deviation. This pixel reduction determines a relative standard deviation over the average intensity less than 3.5 % among all the images, and no further cropping lowers substantially the statistic variation.

- Frame averaging.
  Every set of 10 frames were averaged.

- Ambient frame subtraction.
  Every average ambient frame were subtracted from its relative average image. This step was determinant for the elimination of the dark ambient light (although dark plastic sheeting and cardboard were used to cover all the possible ambient illumination sources, the 'calibration area' was not completely dark yet). The correction from dark current was performed automatically by the camera if selected from the software.

- Determination of the ratio of ratios.
  Since no self-illumination correction, no non-linearity correction between the exposure time

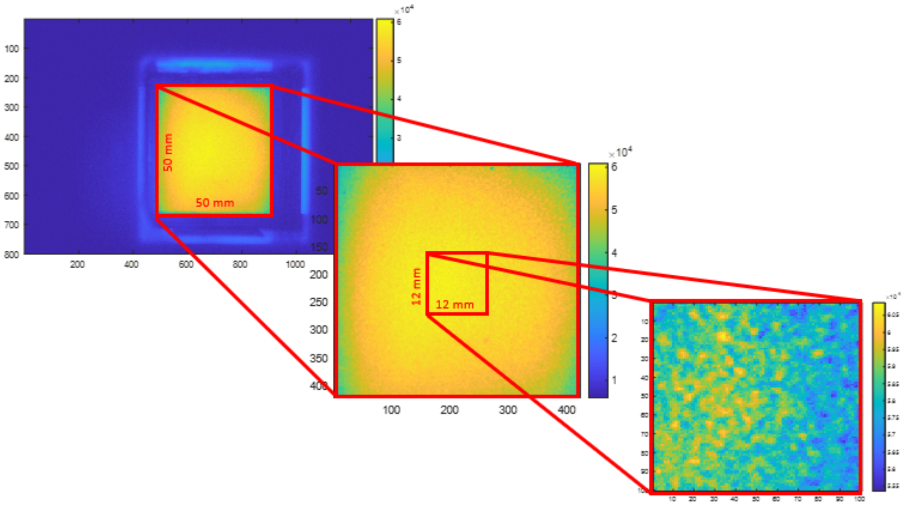

Figure 6.12: Cropping of the frame

(which was fixed) and the intensity output, and no image registration (the use of only one camera at wind-off conditions does not determine an image disalignment) were needed, the procedure can move to the computation of the intensity ratio and the plotting of the Stern-Volmer equation. The reference pressure at wind-off conditions in S-1/C is around 10 kPa, nevertheless, due to vacuum pump limitations combined to a better reading of the calibration curves, the reference pressure was set to 20 kPa. Three types of intensity ratios were analyzed (Table 6.5): the pressure luminophore intensity ratio (λ_1, red), the reference luminophore intensity ratio (λ_2, green) and their ratio (Ratio of Ratios) which compensates for the temperature effect in Binary PSP.

Equation	Dependency
$\frac{I_{\lambda 1,\, ref}}{I_{\lambda 1}}$	Dependent upon pressure, dependent upon temperature
$\frac{I_{\lambda 2,\, ref}}{I_{\lambda 2}}$	Not dependent upon pressure, dependent upon temperature
$\frac{R_{ref}}{R} = (\frac{I_{\lambda 1,\, ref}}{I_{\lambda 1}}) \,/\, (\frac{I_{\lambda 2,\, ref}}{I_{\lambda 2}})$	Dependent upon pressure, weakly dependent upon temperature

Table 6.5: Intensity ratios and characteristics

- Fitting and determination of the Stern-Volmer coefficients.
  Two equations for the interpolation of the experimental data were considered: the traditional linear Stern-Volmer equation.

$$\frac{I_{ref}}{I} = A\,(T) + B\,(T)\,\frac{p}{p_{ref}} \tag{6.3}$$

and the non-linear (qudratic polynomial) Stern-Volmer equation for a better fitting.

$$\frac{I_{ref}}{I} = A\,(T) + B\,(T)\,\frac{p}{p_{ref}} + C\,(T)\,(\frac{p}{p_{ref}})^2 \tag{6.4}$$

Figure 6.13a shows the behavior of the intensity ratios as function of the pressure ratio at fixed temperature. The 'red' and the 'blue' curves shows a very flat trend compared to the calibration

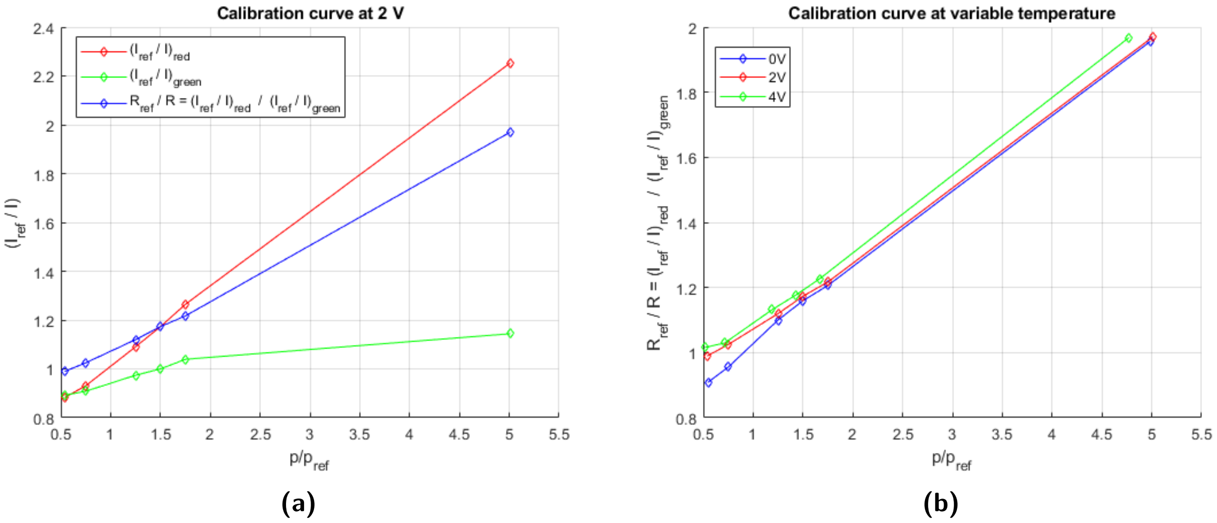

Figure 6.13: Calibration curve at 2 V (a). Ratio of ratios with variable temperature (b). Pressure range (10 kPa - 100 kPa)

curves for Binary FIB provided by the literature (Figures 2.4 and 4.1b). This effect is due to the pressure leakages experienced at the connection between the vacuum tube and the chamber. When the vacuum pump was on, the flow leakages determined a difference between the real depressurization (smaller) inside the chamber and the measured depressurization (larger) by the calibrator. The average intensity of the detected frames was therefore lower with respect to the theoretical intensity the frames should have at the measured depressurization. A lower intensity means a higher intensity ratio in the calibration curve. The larger is the depressurization supplied by the vacuum pump, the larger are the pressure leakages. Hence, the lower is the pressure ratio, the larger is this error, which tends to flatten the overall calibration curve. A forced lock of the pipes and junctions combined with the use of teflon and plasticine did not bring much improvement. The point at ambient pressure was determined with the vacuum pump off, accordingly it does not depend on this effect. To be consistent with the analysis of the results, the ambient pressure point was removed. An other error is dominant for the interpretation of the results. The 'green' curve is not totally insensitive to pressure. The cause is the low OD of the green filter, which fails to absorb 'completely' the pressure probe peak (Figure 6.9). This effect influences the ratio of ratios and its pressure sensitivity derived from the curve.

Figure 6.13b displays the ratio of ratios as function of pressure ratio with variable temperature. The higher the temperature, the more is the thermal quenching which determines a lower intensity, hence a higher intensity ratio. The effect was already verified during spectrometry in Figure 6.10b.

Figure 6.14 present the results after removing the point at ambient pressure. However the calibration curve ('blue') is almost flat because of the pressure leakage effect. Linear and quadratic polynomials representing the Stern-Volmer equations fit the experimental data. All the remaining graphs are reported in Figures A.9 and A.10 in the Appendix. The temperature dependency is not fully compensated after computing the ratio of ratios. Comparing the graphs of the intensity ratio of both the two luminophore separately, it can be noted how the green optical filter affects these results. Table 6.6 displays the Stern-Volmer coefficients and the coefficient of determination of the

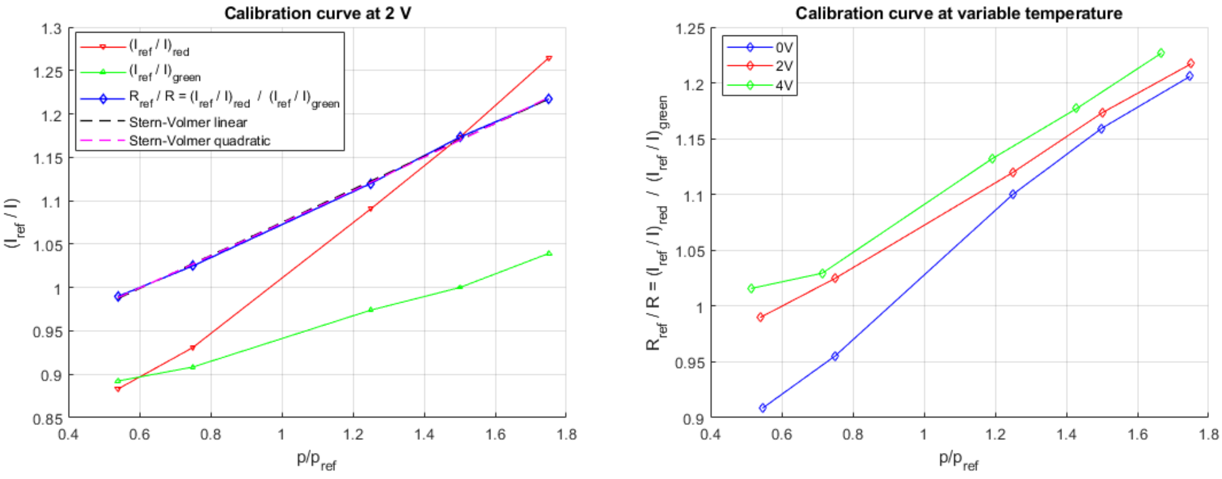

(a) **(b)**

Figure 6.14: Calibration curve and Stern-Volmer relation at 2 V (a). Ratio of ratios with variable temperature (b). Pressure range (10 kPa - 35 kPa)

fitting. Although the R^2 coefficient is slightly closer to the unity for the non-linear interpolations, the calibration curves can be well approximated by the classical linear Stern-Volmer equation. Anyway, the influence of the errors due to pressure leakages and low quality of the optical filters are much larger than the error due the linear fitting.

T level [V]	S-V equation	A [-]	B [-]	C [-]	R^2 [-]
0	linear	0.7698	0.2555		0.9953
0	quadratic	0.7226	0.3545	-0.0437	0.9980
2	linear	0.8847	0.1902		0.9992
2	quadratic	0.8922	0.1742	0.0071	0.9994
4	linear	0.9071	0.1896		0.9908
4	quadratic	0.9432	0.1098	0.0370	0.9941

Table 6.6: Stern-Volmer coefficients and statistics of the fitting

The measured pressure and temperature sensitivity are compared to the values from the ISSI Binary FIB datasheet in Table 6.7. The measured pressure sensitivity is larger than the value provided by the PSP manufacturers because of the pressure leakages that make the curve flatter and steeper, overestimating the value. The measured temperature sensitivity is slightly larger than the quoted value. The cause is mainly the implementation of the low quality optical filters, in particular the green filter allows for a not negligible pressure dependence in the reference intensity ratio, which negatively affects the ratio of ratios and the compensation for temperature-sensitivity effect.

6.5.1 Uncertainty analysis

The following analysis aims to quantify the uncertainty in the measurement chain for the determination of the Stern-Volmer coefficients. The uncertainty evaluation carried out by M. Quinn (2018)

	ISSI datasheet	Measured
P_{sens} [% / kPa @ 20 °C]	0.6	0.12
T_{sens} [% / °C @ 100 kPa]	0.03	0.09

Table 6.7: Comparison of measured pressure and temperature sensitivity with datasheet from ISSI

in [20] was taken as a reference. The analysis takes into consideration the combined effects of the averaged frame intensity ratios captured by the photodetector, the pressure and temperature uncertainties, and the sensitivity of the Stern-Volmer coefficients to temperature.

The maximum standard deviation of the averaged cropped frames divided by the reference averaged cropped images at p_{ref} was computed for each temperature point and it is displayed in Table 6.8. The maximum value among the three temperature sets was considered for the analysis.

T level [V]	σ_{max} [-]
0	0.0246
2	0.0227
4	0.0130

Table 6.8: Maximum standard deviation of the processed frame ratios

The uncertainty of the pressure measurement depends upon the accuracy of the pressure calibrator. 0.025 % FS (Full Scale) including combined non-linearity, hysteresis and repeatability was specified on the manufacturer's datasheet for the pressure range involved in the calibration, which corresponds to an absolute uncertainty of 18 Pa. The maximum relative uncertainty is calculated considering the lower absolute pressure experienced during the calibration (10 kPa). Due to difficulties for the estimation of the pressure leakages, this error was not included in this analysis. Uncertainty in temperature control of the painted plate includes three effects separately. The absolute uncertainty was below 0.5 °C for the temperature control of the thermocouple inside the copper base supplied by the Peltier cell in the range 0 V - 4 V. In the same span, the maximum absolute error between the copper base and aluminum sample was less than 3 °C. Finally, the infrared analysis gave a standard deviation below 0.2 °C. of the cropped images that assessed the temperature uniformity. The maximum absolute error is determined as the sum of this uncertainties. The sensitivity of the Stern-Volmer coefficients to temperature, estimated by the least-squared linear fit of the experimental data of the calibration curves at each temperature value, was determined computing their gradient with respect to temperature. The values, shown in Table 6.9, where then multiplied by the absolute uncertainty in temperature presented above.

$\frac{\partial A}{\partial T}$ [1 / °C]	0.00856
$\frac{\partial B}{\partial T}$ [1 / °C]	0.00417

Table 6.9: Maximum sensitivity of the Stern-Volmer coefficient to temperature

The root-sum squared method (RSS) were used to estimate the final uncertainty of the Stern-Volmer coefficients, including all the relative uncertainties previously described in the following equation.

$$RSS = \sqrt{\sum_{i=1}^{n} \sigma_i^2} \tag{6.5}$$

The resulting uncertainties are herein displayed in Table 6.10. Compared to the values obtained by M. Quinn in [20], the uncertainty in the calibration parameters are one order of magnitude larger. The main cause is the large uncertainty in the temperature control. The value could be reduced by performing a direct infrared analysis to assess directly the mean value and standard deviation of temperature over the plate. However, the thermocamera needs to be properly calibrated, the top window should be changed into new optical access with high transmission in the infrared spectrum, and the sample must be painted evenly by a special black paint to strongly enhance its emissivity at low temperatures. A larger number of IR images or multiple thermocouple-Peltier calibrations and consequently averaging them, should produce the best data.

A	±0.0261
B	±0.0250

Table 6.10: Uncertainty of the Stern-Volmer coefficients

6.6 Post-processing design in S-1/C

A basic theoretical design of the procedure for post-processing the data after testing in S-1/C is now described. Figure 2.6 shows the general and more complete data-processing flowchart after image acquisition for the measurement of pressure over the model surface. Similarly to the data-processing procedure implemented for the calibration of the PSP, the sets of wind-on and wind-off frames are cropped and averaged. These images are then corrected for dark current effect directly by PCC Phantom and the averaged ambient light frames (captured when all controllable light sources are turned off) are then subtracted from the processed wind-on and wind-off images. The correction of the non-linear response to the incidence irradiance of light can slightly improve the accuracy of the measurements. The corrected wind-on images should be registered in order to compensate for the frame disalignment caused by the model deformation when subjected by aerodynamics loads. However, the use of a single camera for steady-state measurements and a a low magnification factor (typically $M < 0.1$ as stated by M. Bitter (2016) in [16]) can make a small model deformation (approximately below 0.5 mm) which is typically not noticeable on the imaging sensor because the shift is below 1 px. The same zoom-lens used during the calibration can be used during testing in the facility, and it is easy to make the magnification factor below 0.1 because of the large minimum distance between the optical window and the blade. Afterwards, the ratio of ratios can be computed and the PSP Stern-Volmer equation determined during the calibration (in-situ, which gives the most reliable results) can be applied. At this stage pressure data have to be mapped onto a 2D grid representing the model by means of an image resection technique. Self-illumination correction can be neglected for this application since no convex surfaces are included into the model surface. The final results can be compared to CFD and experimental data acquired by traditional pressure measurement techniques.

Chapter 7

Conclusions and Future Work

The thesis has presented the development of a new method for measuring the 2D steady-state pressure over the model surfaces of a linear transonic cascade. In particular the work focused on the setup design, preparation and testing for the determination of the calibration curve of a pressure sensitive painted sample, aimed at the implementation and subsequent development of the measurement technique within the S-1/C facility at von Karman Institute.

The facility was firstly analyzed to assess the possibility of the implementation of the PSP technique. The present optical accesses, the geometrical dimensions of the facility, the nominal flow conditions and the static temperature variations of the flow determined the main requirements for the selection of the instrumentation. The design of the experiments was carried out after analyzing a large variety of similar setups present in the literature, combined to the specific requirements of the project. After the detailed study for the choice of the paint, illumination source, detection system and several other components needed in the ex-situ calibrations, the experimental phase was started. The obtaining of the a-priori calibration coefficients required several intermediate steps. The calibration of the thermocouple in the oven and the subsequent relation between the power supplied by the Peltier cell and the temperature experienced by the sample inside the calibration chamber were combined to an optic infrared analysis for the verification of the temperature uniformity over the sample. One hour was sufficient to reach a stable thermal equilibrium at each point of the curve. The use of an additional type-K thermocouple was helpful to assess the small temperature difference after one hour between the copper base and the aluminum sample. Due to PSP toxic emissions while spraying, the design of an adequate safety procedure for the application of the paint on the samples has been of major importance. The spectrometric analyses aimed to asses the validity of the optical filters and the behavior of the painted model under different temperature and pressure conditions. Nevertheless, the spectrometry showed a low quality of the filters, which was considered in the explanation of the final calibration results. The goal of the final experimental test campaign was the a-priori calibration of the PSP applied on the model surface. After image-processing, the calibration curves at variable temperature were studied. In particular, the contemporary study of the three intensity ratios of the Binary PSP helped the understanding of the results. Errors due to pressure leakages in the vacuum piping system and low optical density of the filters were explained by analyzing the obtained curves. The pressure and temperature sensibility of the PSP in the calibration chamber was found similar to the specification of the manufacturer, anyway the differences were analyzed in the frame of the calibration setup errors. The least-squared fit of the experimental data was needed for the estimation of the Stern-Volmer coefficients. A final uncertainty analysis aimed at quantifying the uncertainty in the calibration parameters considering the influence of the overall measurement chain. The entire work has been done in order to lay the foundations towards the measurement test campaign in the facility. A constant attention was applied to correlate the calibration of the painted sample with the implementation inside the wind-tunnel. In addition, a brief discussion on the design of the in-situ and testing analyses has been treated within the thesis.

Future developments of the work should include the substitution of the two optical filters with high OD filters which properly fit the wavelength intervals of the two emissions and guarantee high transmission in those ranges. For easiness of the setup, post-processing and best quality of results, a RGB camera could be considered, removing the problem of separation of the two color emissions and the uncertainty in the switch of the filter at the base. Further consideration might be related to the design of a new calibration chamber or to an improvement of the existing one. The main issue is represented by the pressure leakages experienced at the connection to the piping system. The possibilities are either the realization of a new insert to the chamber or the redesign of a wall side to create a hole for the insertion of a static pressure transducer which allows for direct pressure measurements inside the chamber. In order to reduce the uncertainty in the control temperature, a single infrared analysis should be sufficient to assess the mean value and the standard deviation of the absolute temperature over the painted plate. Nevertheless, the thermocamera has to be properly calibrated and a redesign of the cell top-window is necessary to both substitute the material which is inappropriate for high infrared transmission and to better isolate the air in the chamber from the external environment (a screwed metal plate at the borders with a central glass window insert could be the best). The use of high emissivity black paint and a larger amount of frames to average can give the best results. Once the new ex-situ calibration curve is obtained, the in-situ correction should be considered. The test article must be instrumented by pressure taps and the infrared camera aims to measure the surface temperature from the new optical accesses of the facility. These results will be then used after image acquisition over the blade and bottom-endwall of the cascade to build the pressure mapping.

Appendix A

Graphs and Images

Signal-filtering of the thermocouple. Calibration in the oven

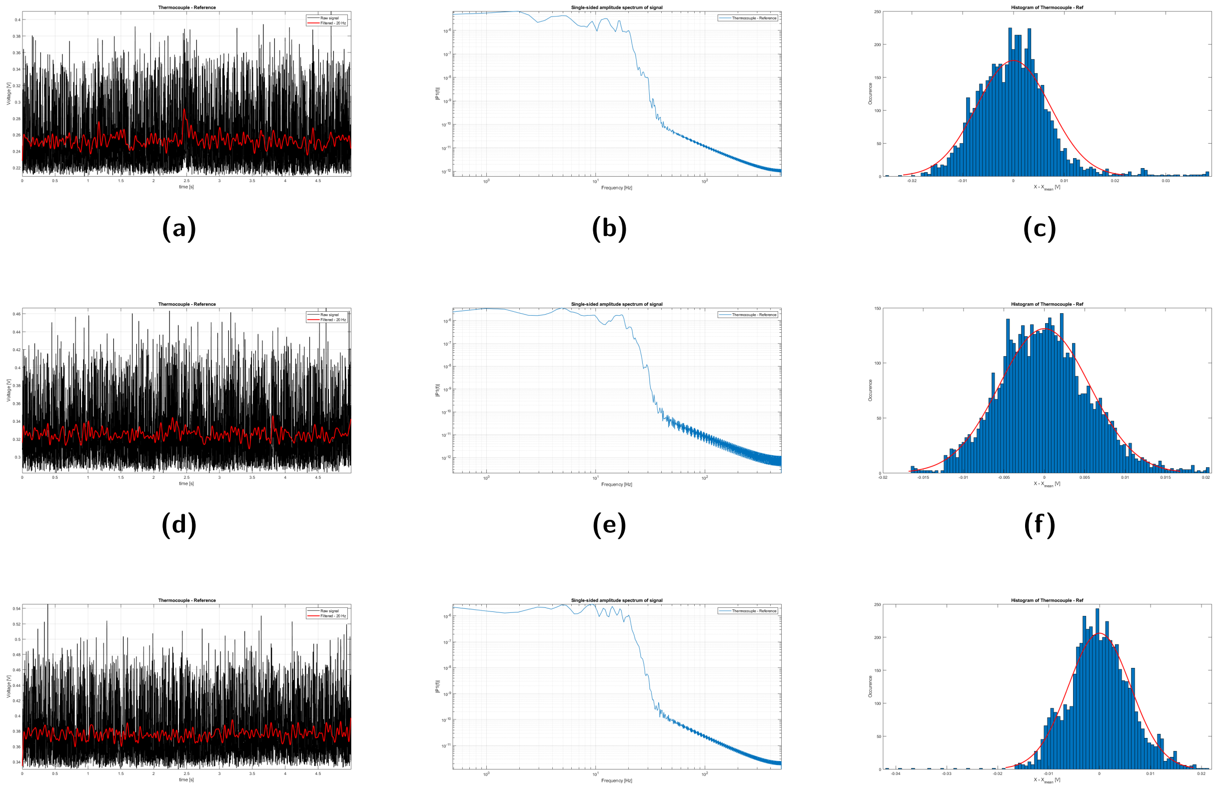

(a) (b) (c)

(d) (e) (f)

(g) (h) (i)

Figure A.1: Calibration of the thermocouple 21°C, 30°C, 35°C - Raw and filtered voltage signal (left). PSD of the filtered signal (middle). Histogram of filtered data (right)

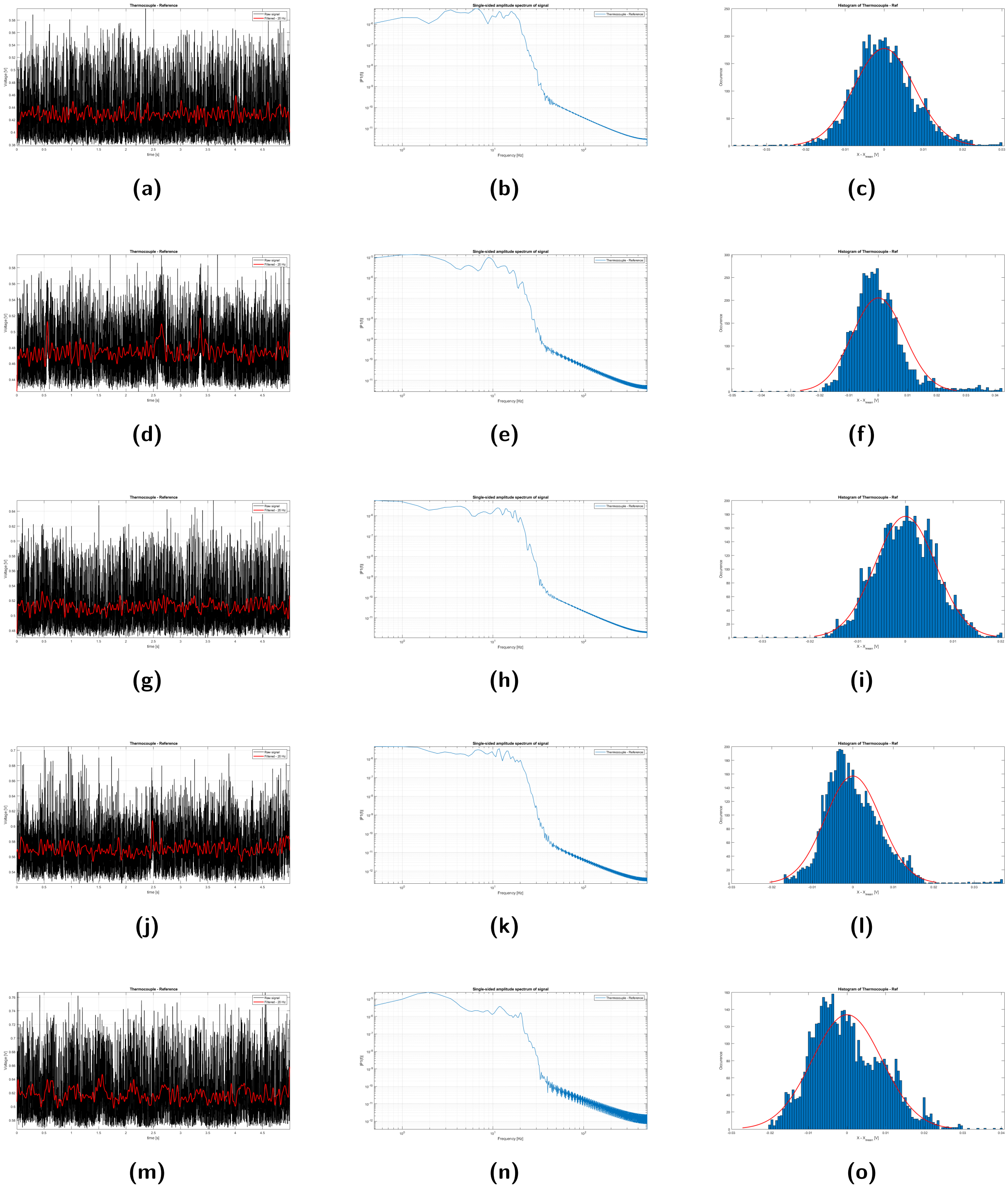

(a) **(b)** **(c)**

(d) **(e)** **(f)**

(g) **(h)** **(i)**

(j) **(k)** **(l)**

(m) **(n)** **(o)**

Figure A.2: Calibration of the thermocouple 40°C, 45°C, 50°C, 55°C, 60°C - Raw and filtered voltage signal (left). PSD of the filtered signal (middle). Histogram of filtered data (right)

Signal-filtering of the thermocouple. Calibration of the Peltier cell

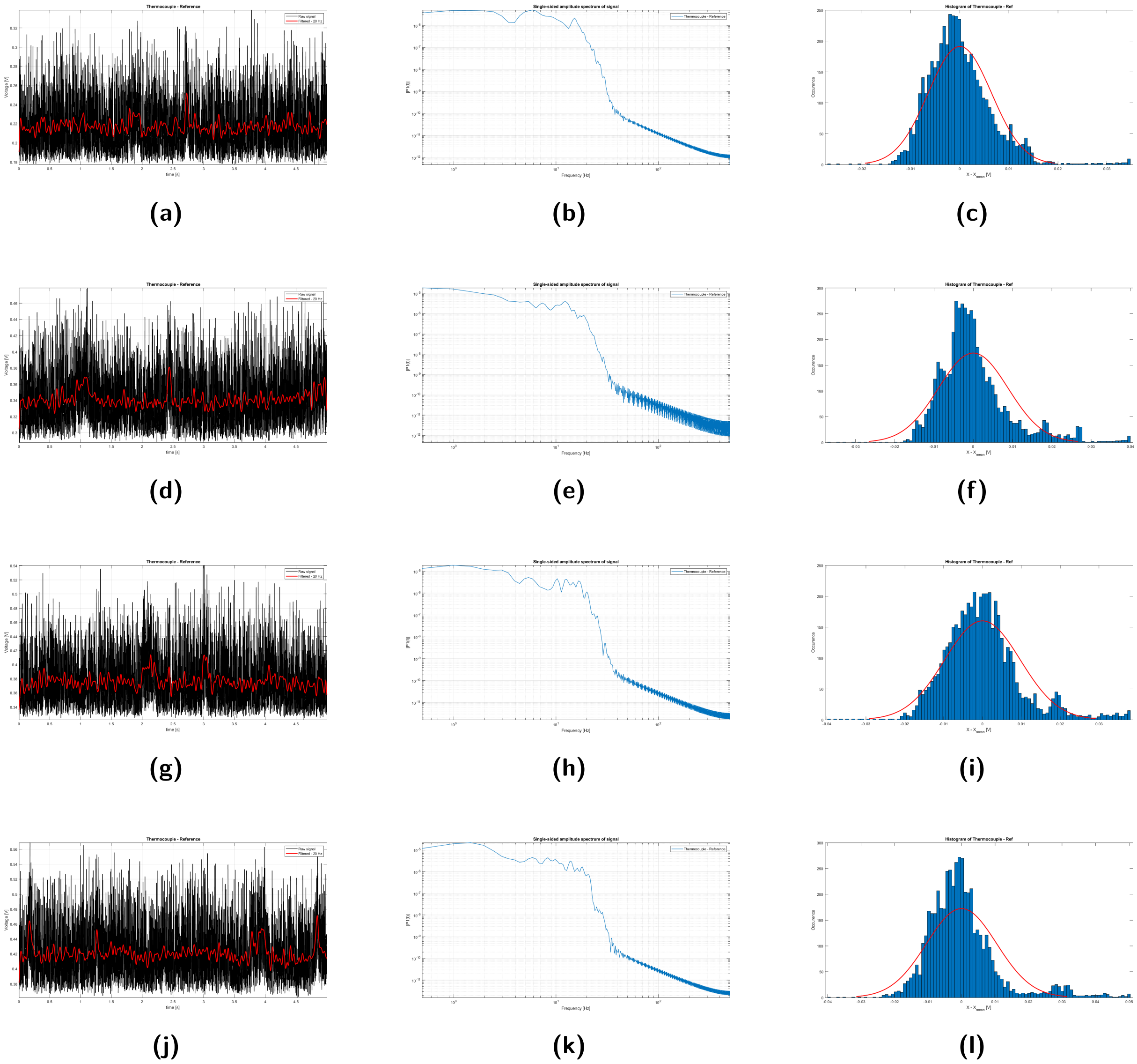

(a) (b) (c)

(d) (e) (f)

(g) (h) (i)

(j) (k) (l)

Figure A.3: Calibration of the Peltier cell 0-5 V - Raw and filtered voltage signal (left). PSD of the filtered signal (middle). Histogram of filtered data (right)

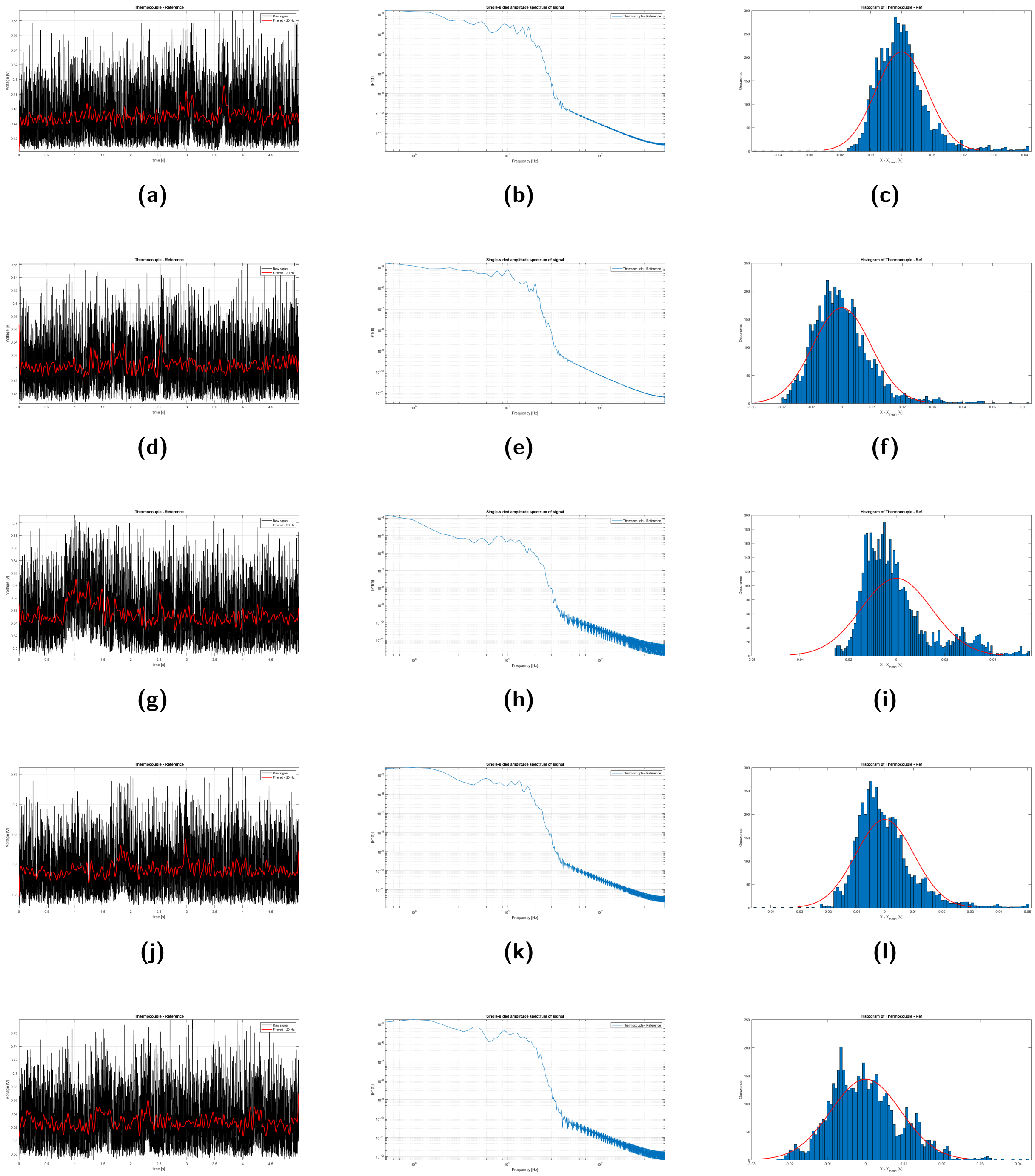

(a) **(b)** **(c)**

(d) **(e)** **(f)**

(g) **(h)** **(i)**

(j) **(k)** **(l)**

(m) **(n)** **(o)**

Figure A.4: Calibration of the Peltier cell 5-10 V - Raw and filtered voltage signal (left). PSD of the filtered signal (middle). Histogram of filtered data (right)

Infrared images and statistical dispersion

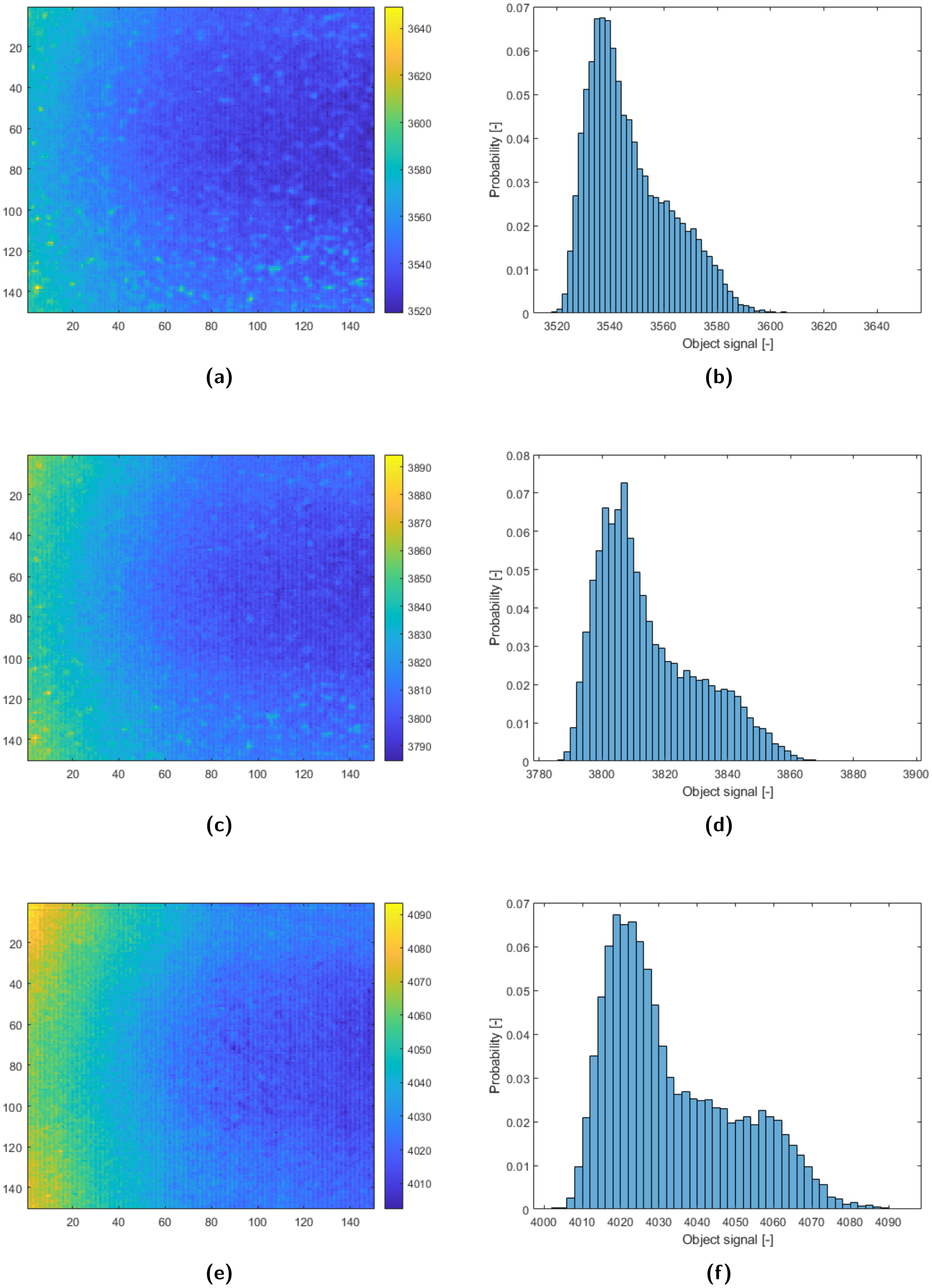

(a) **(b)**

(c) **(d)**

(e) **(f)**

Figure A.5: Infrared analysis (OS) 0V, 1V, 2V - Scaled infrared image (left). Histogram of data (right)

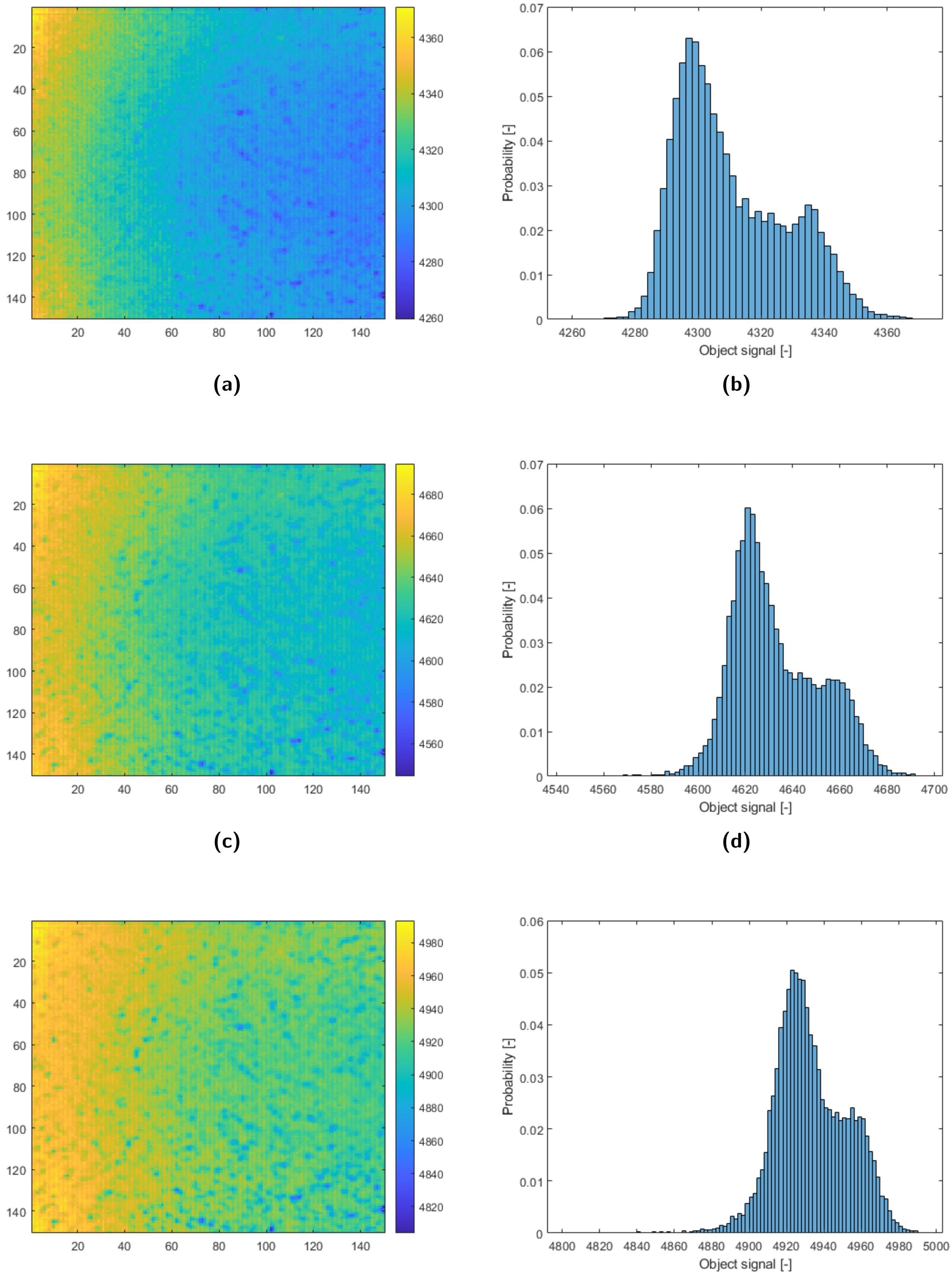

(a) **(b)**

(c) **(d)**

(e) **(f)**

Figure A.6: Infrared analysis (OS) 3V, 4V, 5V - Scaled infrared image (left). Histogram of data (right)

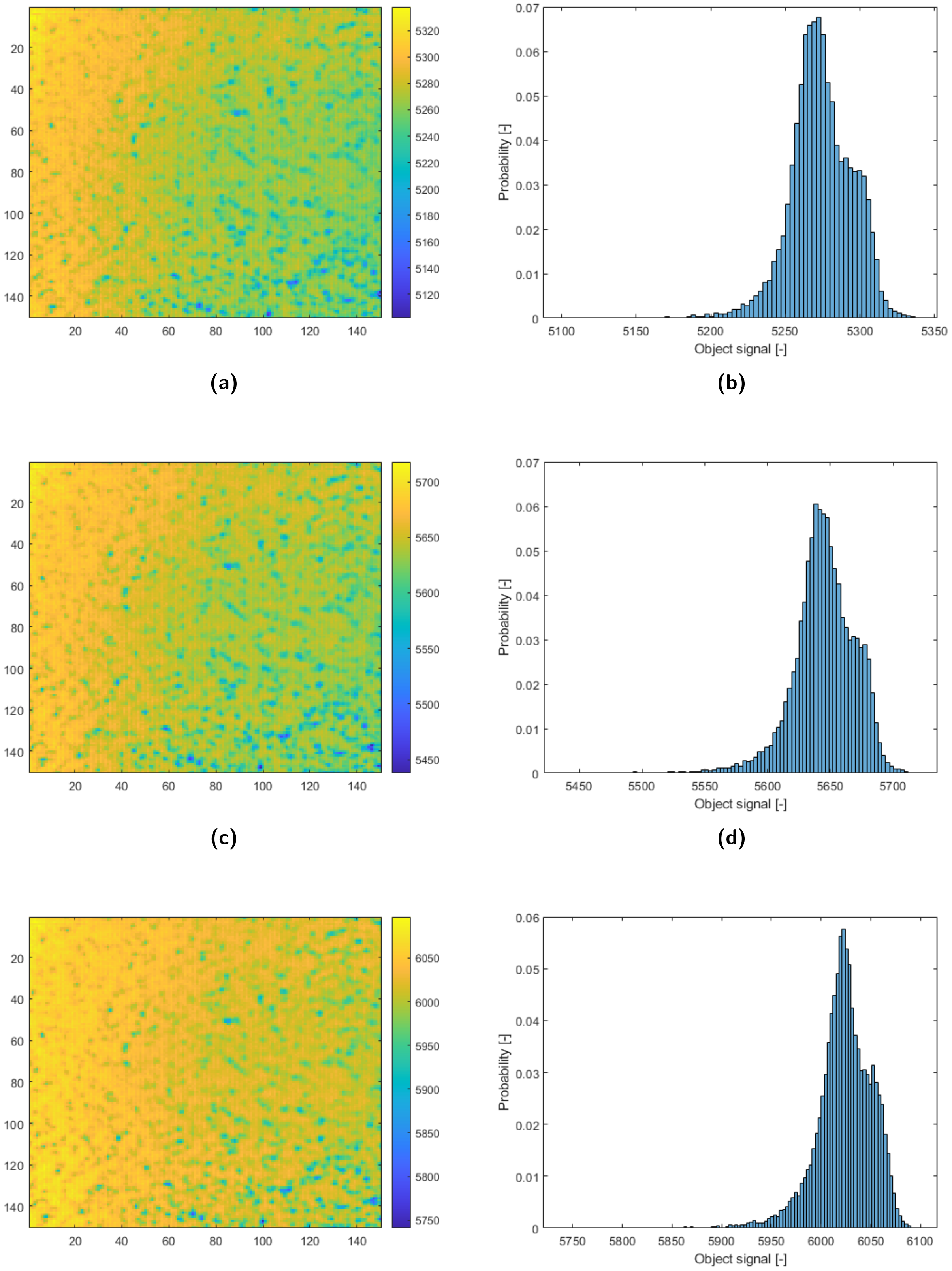

(a) **(b)**

(c) **(d)**

(e) **(f)**

Figure A.7: Infrared analysis (OS) 6V, 7V, 8V - Scaled infrared image (left). Histogram of data (right)

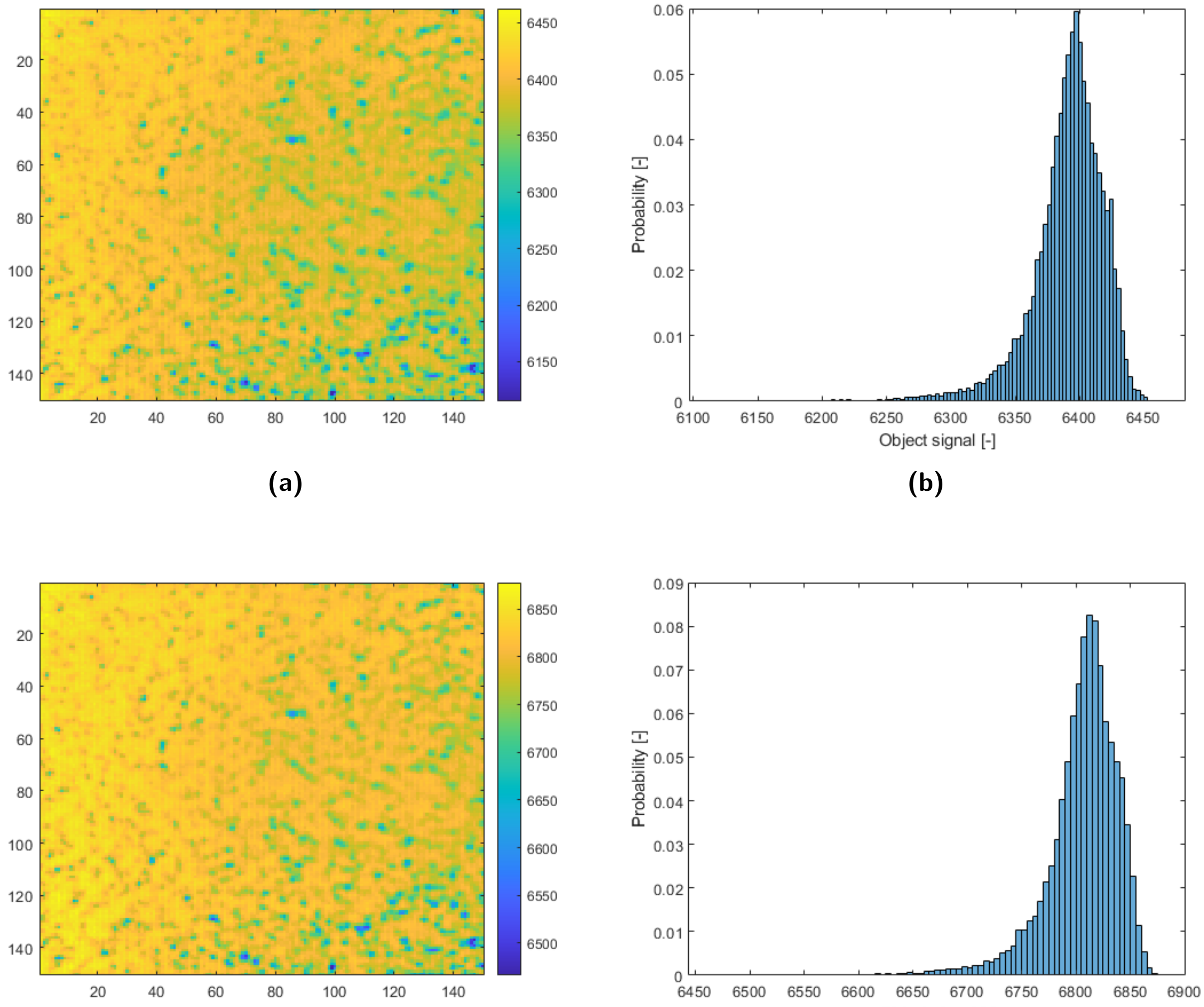

(a) **(b)**

(c) **(d)**

Figure A.8: Infrared analysis (OS) 9V, 10V - Scaled infrared image (left). Histogram of data (right)

Calibration curves and fitting

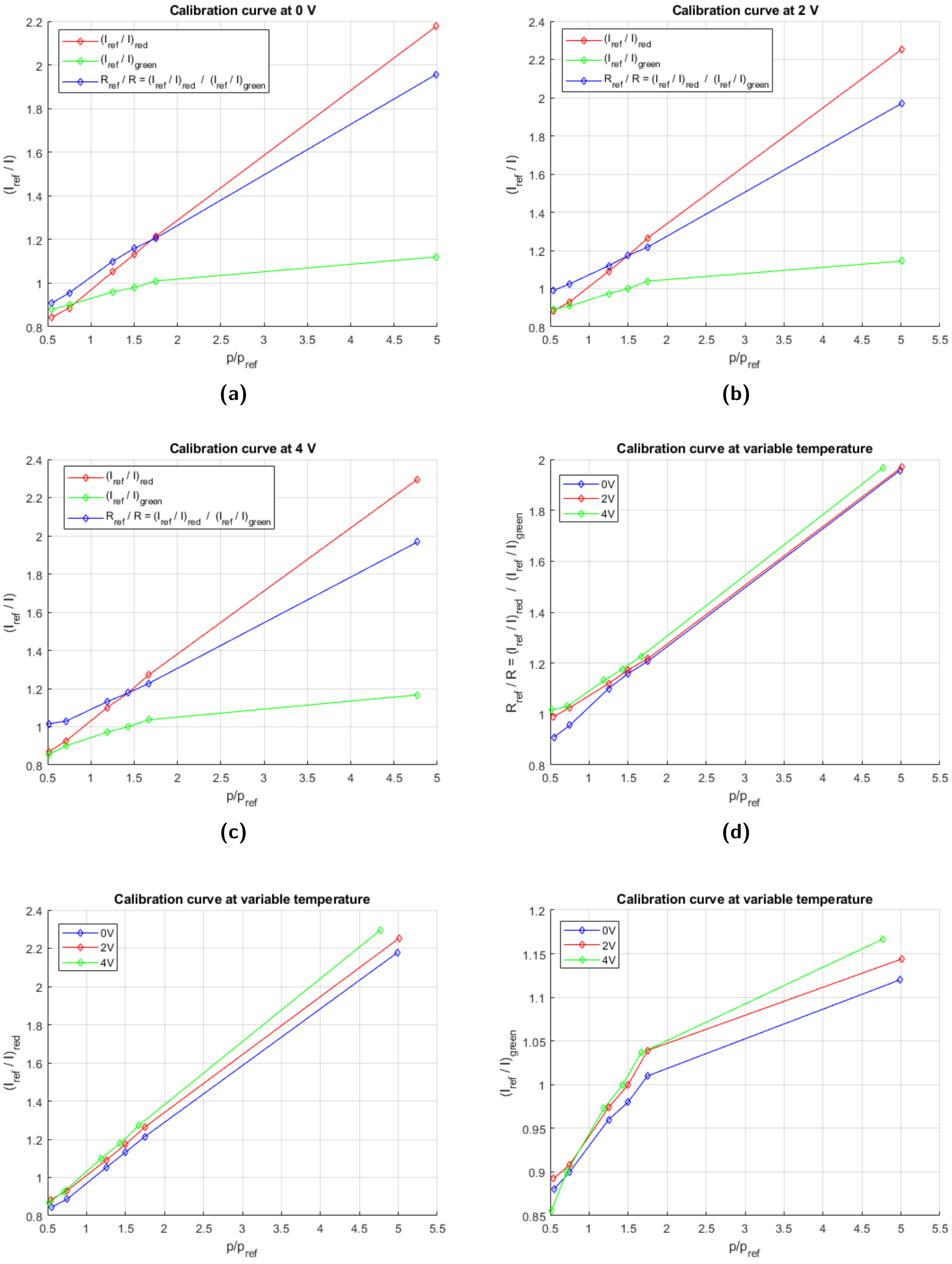

(a) (b) (c) (d) (e) (f)

Figure A.9: Calibration curve at 0 V (a), 2 V (b), 4 V (c). Calibration curve with variable temperature - ratio of ratios (d), pressure probe (e), reference probe (f). Pressure range (10 kPa - 100 kPa)

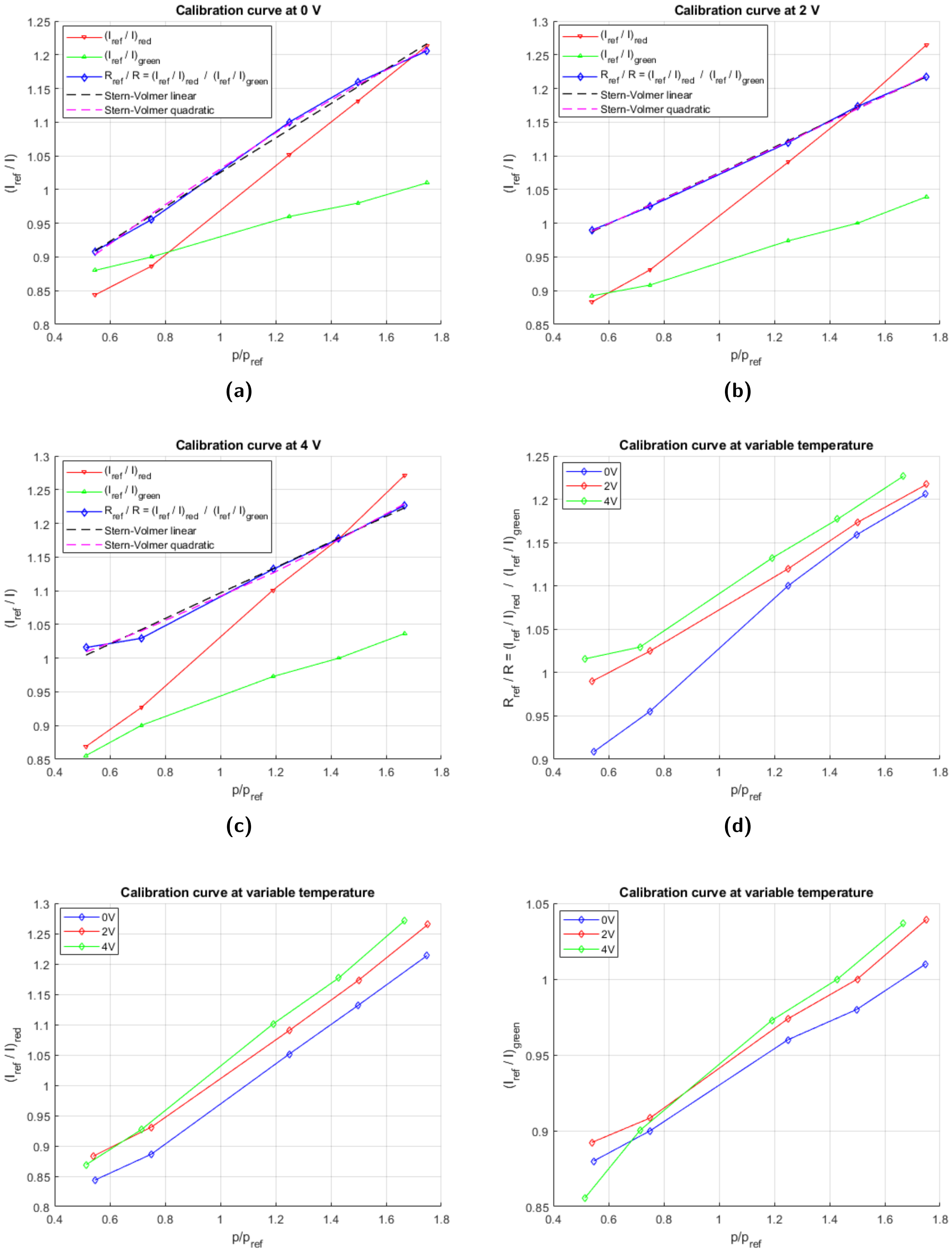

(a)

(b)

(c)

(d)

(e)

(f)

Figure A.10: Calibration curve and Stern-Volmer relation at 0 V (a), 2 V (b), 4 V (c). Calibration curve with variable temperature - ratio of ratios (d), pressure probe (e), reference probe (f). Pressure range (10 kPa - 35 kPa)

Appendix B

Codes

Data-filtering from Labview - Thermocouple calibration

```
%% code to import and process data obtained with NI-DAQ X Series

clear
close all
clc

w_dir = pwd;

%% select working directory
% work_dir = uigetdir('*.*', 'Select working directory');

%% import data

cd ..
[file, path] = uigetfile('*.*', 'Select file with raw data');
filename = fullfile(path, file);
cd(w_dir)
[t, Thermo_PSP_Cell.signal] = import_data(filename);

clear filename path file

%% determine mean values of raw data

Thermo_PSP_Cell.mean_raw = mean(Thermo_PSP_Cell.signal);

%% Filter signal

```

```
order  = 4;               % Order of filter
cutoff = 20;
hpf = 2*cutoff/(round(length(t)/t(end)));              % Half power frequency

if round(length(t)/t(end)) == 1000 && t(end) > 1
    d = designfilt('lowpassiir', ...
        'FilterOrder', order, ...
        'HalfPowerFrequency', hpf, ...
        'DesignMethod', 'butter');
else
    d = designfilt('lowpassiir', ...
        'FilterOrder', order, ...
        'HalfPowerFrequency', hpf, ...
        'DesignMethod', 'butter');
end

Thermo_PSP_Cell.filter = filtfilt(d, Thermo_PSP_Cell.signal);

%% Remove outliers in raw data
%
% [Thermo_PSP_Cell.outliers, Thermo_PSP_Cell.ind_outliers] = rmoutliers(Thermo_PSP_Cell.signal);
% [Thermo_traverse.outliers, Thermo_traverse.ind_outliers] = rmoutliers(Thermo_traverse.signal);
% [Thermo_injection.outliers, Thermo_injection.ind_outliers] = rmoutliers(Thermo_injection.signal);
%
% % pre-allocate arrays
% Thermo_PSP_Cell.time = [];
% Thermo_traverse.time = [];
% Thermo_injection.time = [];
%
% for ii = 1:length(t)
%     if Thermo_PSP_Cell.ind_outliers(ii) == 0
%         temp = t(ii);
%         Thermo_PSP_Cell.time = [Thermo_PSP_Cell.time; temp];
%     end
%
%     if Thermo_traverse.ind_outliers(ii) == 0
%         temp = t(ii);
%         Thermo_traverse.time = [Thermo_traverse.time; temp];
```

```
%       end
%
%       if Thermo_injection.ind_outliers(ii) == 0
%           temp = t(ii);
%           Thermo_injection.time = [Thermo_injection.time; temp];
%       end
% end
%
% clear temp

%% determine mean values of low pass filtered data

Thermo_PSP_Cell.mean_filt = mean( Thermo_PSP_Cell.filter( ...
    0.01 * length( Thermo_PSP_Cell.filter ) : ...
    0.99 * length( Thermo_PSP_Cell.filter ) ) );


%% plot data

figure
set(gcf,'Renderer','painters')
frame_h = get(handle(gcf),'JavaFrame');
set(frame_h,'Maximized',1);
plot(t, Thermo_PSP_Cell.signal, 'k', 'linewidth', 1)
hold on
plot(t, Thermo_PSP_Cell.filter, 'r', 'linewidth', 2)
% plot configuration
xlabel('time [s]')
ylabel('Voltage [V]')
legend('Raw signal', 'Filtered - 20 Hz', ...
    'location', 'northeast')
title('\bf Thermocouple - Reference')
grid on
axis tight

%% FFT analysis

% amplitude
[Thermo_PSP_Cell.P1, Thermo_PSP_Cell.f] = pwelch(Thermo_PSP_Cell.filter - mean(Thermo_PSP_Cell.filter), [], [], [], ...
    round( length( Thermo_PSP_Cell.filter ) / t( end ) ) );

```

```
% plot fast Fourier transforms
figure
set(gcf,'Renderer','painters')
frame_h = get(handle(gcf), 'JavaFrame');
set(frame_h,'Maximized',1);
loglog(Thermo_PSP_Cell.f, Thermo_PSP_Cell.P1, 'linewidth', 1)
xlabel('Frequency [Hz]')
ylabel('|P1(f)|')
title('Single-sided amplitude spectrum of signal')
legend('Thermocouple - Reference', 'Thermocouple - Traverse', ...
    'Thermocouple - Injection','location', 'northeast')
grid on
axis tight

clear ii

%% random uncertainty

% determination of random uncertainty
Thermo_PSP_Cell.S_Xmean = random_standard_uncertainty(
    Thermo_PSP_Cell.filter);

% determination of skewness
Thermo_PSP_Cell.skew = skewness(Thermo_PSP_Cell.filter);

% determination of kurtosis
Thermo_PSP_Cell.kurt = kurtosis(Thermo_PSP_Cell.filter);

% plot histogram of data
figure
set(gcf,'Renderer','painters')
frame_h = get(handle(gcf),'JavaFrame');
set(frame_h,'Maximized',1);
Thermo_PSP_Cell.pd = histfit(Thermo_PSP_Cell.filter - mean(
    Thermo_PSP_Cell.filter), 100, 'normal');
xlabel('X - X_{mean} [V]')
ylabel('Occurence')
title('Histogram of Thermocouple - Ref')

%% create lazy array

vector = [Thermo_PSP_Cell.mean_filt , Thermo_PSP_Cell.S_Xmean];
```

```

vector2 = [Thermo_PSP_Cell.mean_raw];
```

Image-processing from Infrared camera

```
%data-processing of images from InfraRed Camera Flir SC3000%

f=0.5; %image acquisition frequency [Hz]
time=20; %acquisition time [s]
n=f*time; %numer of images acquired [-]

%loading all the .MAT files manually

%averaged image
im=(seq00011+seq00012+seq00013+seq00014+seq00015...
+seq00016+seq00017+seq00018+seq00019+seq000110)/n;

%reduced size of the image to detect only the aluminum sample
imr=im(50:199,50:199);

%mean value of the averaged image array (T: temperature or OS: object signal)
mu=mean(imr,'all');
%standard deviation of the averaged image array
sigma=std2(imr);
%max and min values of the averaged image array
clear max
clear min
max=max(imr,[],'all');
min=min(imr,[],'all');

% %x-axis vector between min and max values
% x=linspace(min,max);
% %normal distribution
% y=normpdf(x,mu,sigma);

%%%graphs%%%
hold off
figure(1)
title('scaled image');
imagesc(imr)
colorbar

figure(2)
```

```
title ('data distribution');
%histogram of the frequency distribution
histogram(imr,'Normalization','probability')
% hold on
%ideal normal distribution that fits the discrete data distribution
%plot(x,y)
%xlabel('Temperature [K]');
xlabel('Object signal [-]');
ylabel('Probability [-]');

output=[mu,sigma];
display(output)
```

Data-processing from OceanView - Static spectrometry

```
%reading data from excel file
data1=xlsread('C:\Users\Scala\Desktop\spectrometry_static.xlsx','A393:E2747'); %filters_10s
data2=xlsread('C:\Users\Scala\Desktop\spectrometry_static.xlsx','F393:G2747'); %nofilters_1s

x=data1(:,1); %replacing the x vector (wavelength)
n=2;
s=zeros(2355,n);

close all
figure(1)
grid on
title('Emission spectrum (99.95 kPa, 0V, filters on)')
xlabel('wavelength [nm]')
ylabel('Normalized intensity [-]')
for i=1:n
    s(:,i)=(data1(:,i+3)-data1(:,i+1))/max(data1,[],'all'); % subtracting the background noise (ambient lighting)
   % and normalization to 1
    hold on
    if i==1
        plot(x,s(:,i),'g') %green filter signal
    else
        plot(x,s(:,i),'r') %red filter signal
    end
    i=i+1;
```

```
end
legend('Green filter','Red filter')

figure(2)
z=(data2(:,2)-data2(:,1))/max(data2,[],'all');
plot(x,z,'b')
grid on
title('Emission spectrum (99.95 kPa, 0V, filters off)')
xlabel('wavelength [nm]')
ylabel('Normalized intensity [-]')
```

Data-processing from OceanView - Temperature-pressure dependent spectrometry

```
%reading data from excel file
data=xlsread('C:\Users\Scala\Desktop\spectrometry_data_excel.xlsx','A393:Y2747');
N=25-4;
n=7; %number of pressure levels
s=zeros(2355,N);
m=zeros(1,N); %array of the max values (red peak)
x=data(:,1); %replacing the x vector (wavelength)
e=765:1748;
xr=x(e); %wavelengths from 500 to 750 nm
close all

%0V
figure(1)
for i=1:n
    s(:,i)=(data(:,i+2)-data(:,2))/max(data,[],'all'); %subtracting the background noise (ambient lighting)
    % and normalization to 1
    %m(i)=max(s(800:end,i));
    i=i+1;
end
hold on
plot(x,s(:,5),x,s(:,6),x,s(:,4),x,s(:,7),x,s(:,3),x,s(:,2),x,s(:,1))
grid on
title('Emission spectrum at 0 V')
legend('10.95 kPa','15.05 kPa','20.05 kPa','25.05 kPa','30.05 kPa','35.05 kPa','99.95 kPa')
xlabel('Wavelength [nm]')
ylabel ('Normalized intensity [-]')

%2V
figure(2)
%determination of max for intensity normalization
M0=max(data(e,n+8)-data(e,n+3));
for i=n+1:2*n
    s(e,i)=(data(e,i+3)-data(e,n+3))/M0; %subtracting the background noise (ambient lighting)
    m(i)=max(s(e,i));
```

```
    i=i+1;
end
hold on
plot(xr,s(e,n+5),xr,s(e,n+6),xr,s(e,n+4),xr,s(e,n+7),xr,s(e,n+3),xr,s(e,n+2),xr,s(e,n+1))
grid on
title('Emission spectrum at 2 V')
legend('10.78 kPa','14.98 kPa','19.98 kPa','24.98 kPa','29.98 kPa','34.98 kPa','100.08 kPa')
xlabel('Wavelength [nm]')
ylabel ('Normalized intensity [-]')

%4V
figure(3)
for i=2*n+1:3*n
    s(:,i)=(data(:,i+4)-data(:,2*n+4))/max(data,[],'all'); % subtracting the background noise (ambient lighting)
    i=i+1;
end
hold on
plot(x,s(:,2*n+5),x,s(:,2*n+6),x,s(:,2*n+4),x,s(:,2*n+7),x,s(:,2*n+3),x,s(:,2*n+2),x,s(:,2*n+1))
grid on
title('Emission spectrum at 4 V')
legend('10.78 kPa','14.98 kPa','19.98 kPa','24.98 kPa','29.98 kPa','34.98 kPa','100.08 kPa')
xlabel('Wavelength [nm]')
ylabel ('Normalized intensity [-]')


%Temperature-dependency (all pressure levels)
figure(4)
for i=1:n
    s(:,i)=(data(:,i+2)-data(:,2))/max(data,[],'all'); %subtracting the background noise (ambient lighting)
   % and normalization to 1
    hold on
    plot(x,s(:,i),'b')
    grid on
    i=i+1;
end
xlabel('Wavelength [nm]')
```

```
ylabel ('Normalized intensity [-]')

for i=n+1:2*n
    s(:,i)=(data(:,i+3)-data(:,n+3))/max(data,[],'all'); % subtracting the background noise (ambient lighting)
    hold on
    plot(x,s(:,i),'r')
    grid on
    i=i+1;
end

for i=2*n+1:3*n
    s(:,i)=(data(:,i+4)-data(:,2*n+4))/max(data,[],'all'); % subtracting the background noise (ambient lighting)
    hold on
    plot(x,s(:,i),'g')
    grid on
    i=i+1;
end

%temperature dependency 0V-2V-4V at 100 kPa
f=6; %15 kPa
figure(5)
grid on
%determination of max for intensity normalization
M0=max(data(e,f+2)-data(e,2));
for f=[1 2 6] %100,35,15 kPa
y0=(data(e,f+2)-data(e,2))/M0; %0V
y2=(data(e,n+f+3)-data(e,n+3))/M0; %2V
y4=(data(e,2*n+f+4)-data(e,2*n+4))/M0; %4V
hold on
plot(xr,y0,'b')
plot(xr,y2,'r')
plot(xr,y4,'g')
legend('0 V','2 V','4 V')
end
xlabel('Wavelength [nm]')
ylabel ('Normalized intensity [-]')
title('Emission spectra at 15 kPa, 35 kPa, 100 kPa, variable temperature')

hold off
```

```
% max at 0V
% ref=3;
% p=[10.95 15.05 20.05 25.05 30.05 35.05 99.95];
% pr=p/p(ref);
% int=[m(5) m(6) m(4) m(7) m(3) m(2) m(1)];
% intratio=(int(ref)*ones(1,n))./int;
% figure(7)
% plot(pr,intratio,'-o')
% grid on

%max at 2V
ref=3; %19.98 kPa
p=[10.78 14.98 19.98 24.98 29.98 34.98 100.08];
pr=p/p(ref);
int=[m(5+n) m(6+n) m(4+n) m(7+n) m(3+n) m(2+n) m(1+n)];
intratio=(int(ref)*ones(1,n))./int;
figure(6)
plot(pr,intratio,'-o')
title('Maximum intensity ratios at 2 V')
xlabel('p/p_{ref}')
ylabel('I_{ref}/I')
grid on
```

Appendix C

Drawings

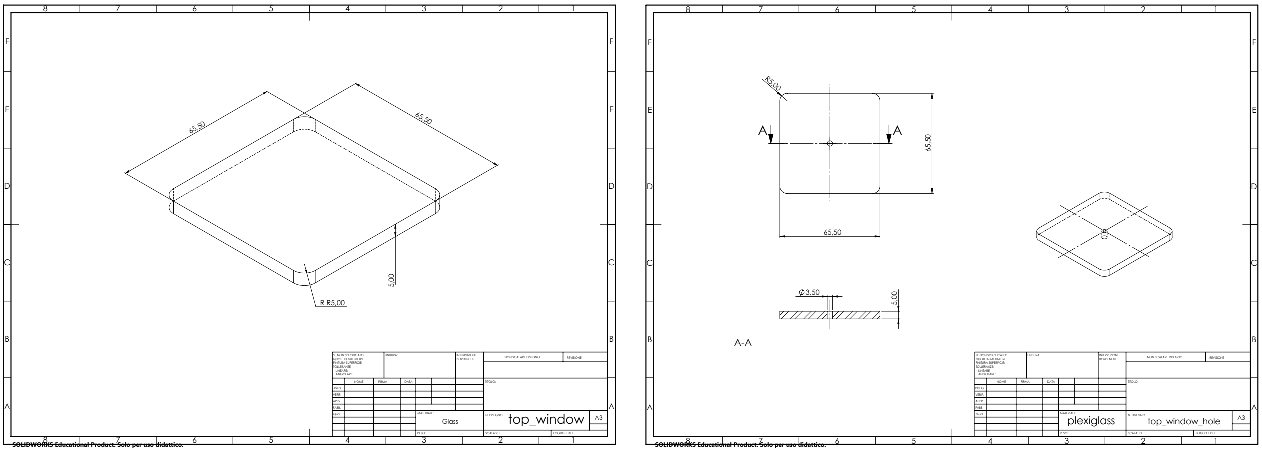

(a) **(b)**

Figure C.1: Top window of the calibration chamber (a). Top windoe of the calibration chamber with central hole (b)

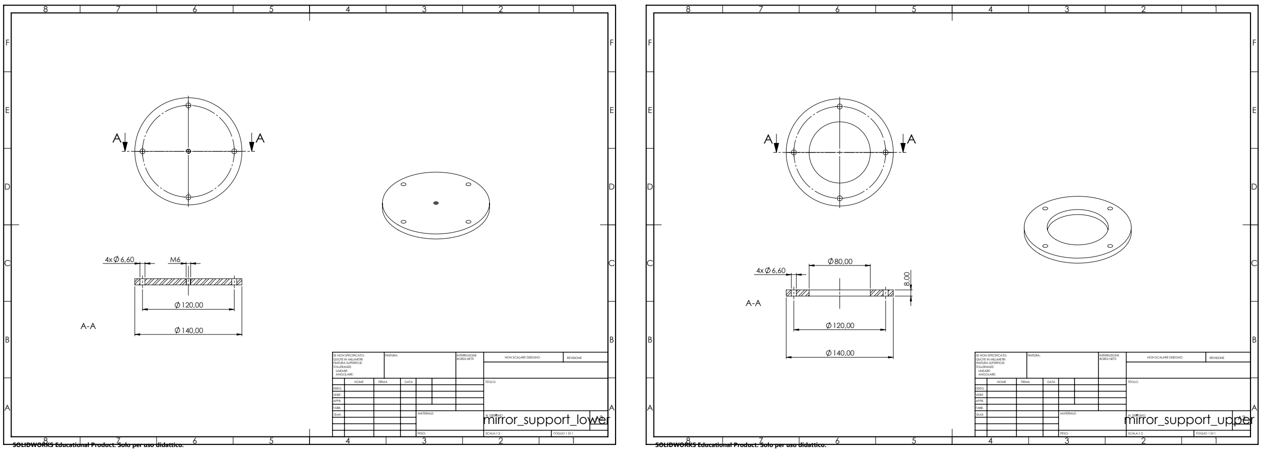

(a) **(b)**

Figure C.2: Lower support for the round mirror - 3D printed (a). Upper support for the round mirror - 3D printed (b)

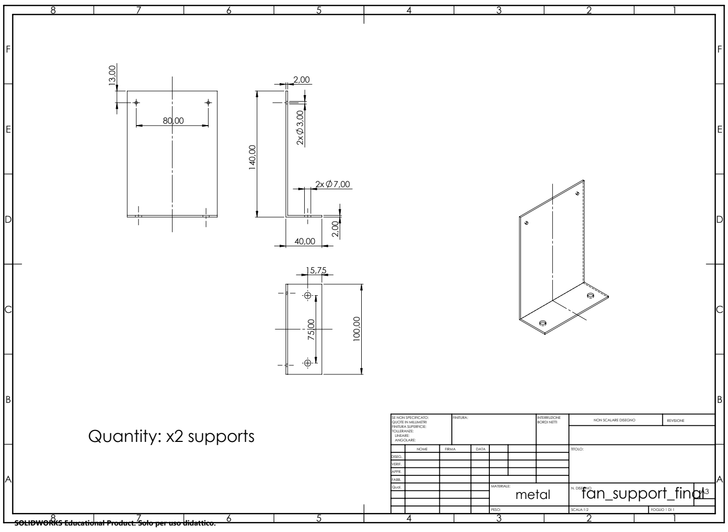

Figure C.3: Supports for the fan - heat sink system

Appendix D

Literature setup analysis

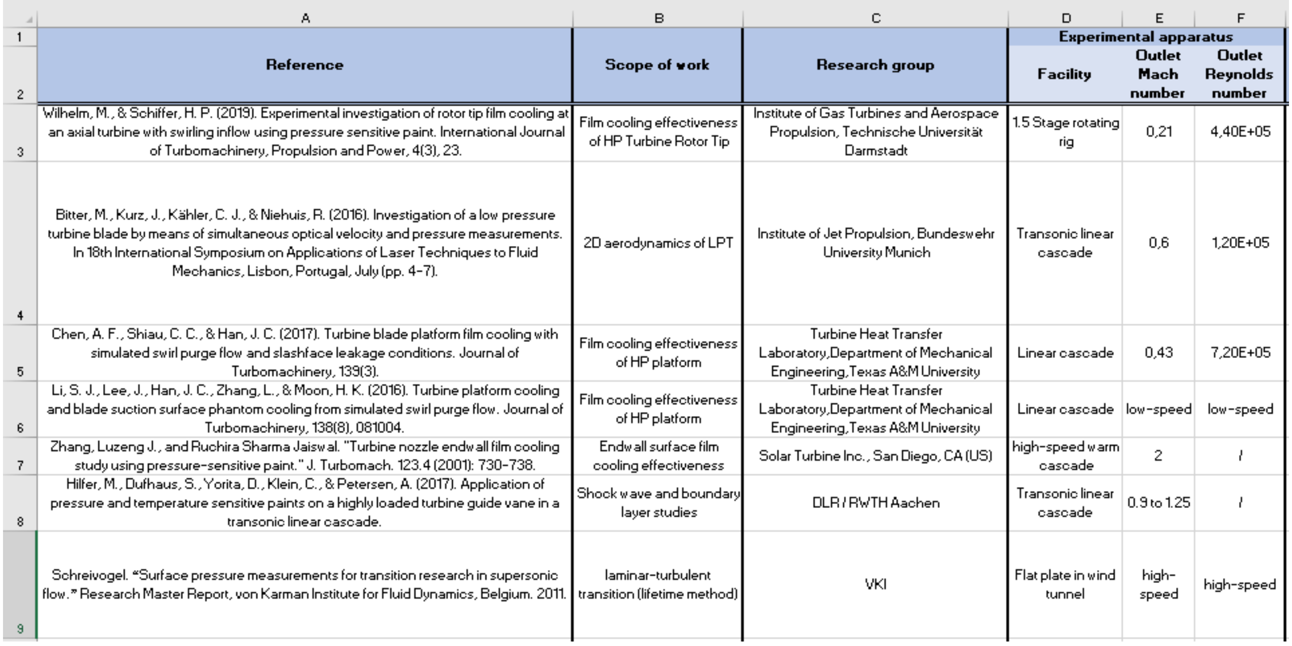

	A	B	C	D	E	F
1	**Reference**	**Scope of work**	**Research group**	**Experimental apparatus**		
2				**Facility**	**Outlet Mach number**	**Outlet Reynolds number**
3	Wilhelm, M., & Schiffer, H. P. (2019). Experimental investigation of rotor tip film cooling at an axial turbine with swirling inflow using pressure sensitive paint. International Journal of Turbomachinery, Propulsion and Power, 4(3), 23.	Film cooling effectiveness of HP Turbine Rotor Tip	Institute of Gas Turbines and Aerospace Propulsion, Technische Universität Darmstadt	1.5 Stage rotating rig	0,21	4,40E+05
4	Bitter, M., Kurz, J., Kähler, C. J., & Niehuis, R. (2016). Investigation of a low pressure turbine blade by means of simultaneous optical velocity and pressure measurements. In 18th International Symposium on Applications of Laser Techniques to Fluid Mechanics, Lisbon, Portugal, July (pp. 4-7).	2D aerodynamics of LPT	Institute of Jet Propulsion, Bundeswehr University Munich	Transonic linear cascade	0,6	1,20E+05
5	Chen, A. F., Shiau, C. C., & Han, J. C. (2017). Turbine blade platform film cooling with simulated swirl purge flow and slashface leakage conditions. Journal of Turbomachinery, 139(3).	Film cooling effectiveness of HP platform	Turbine Heat Transfer Laboratory,Department of Mechanical Engineering,Texas A&M University	Linear cascade	0,43	7,20E+05
6	Li, S. J., Lee, J., Han, J. C., Zhang, L., & Moon, H. K. (2016). Turbine platform cooling and blade suction surface phantom cooling from simulated swirl purge flow. Journal of Turbomachinery, 138(8), 081004.	Film cooling effectiveness of HP platform	Turbine Heat Transfer Laboratory,Department of Mechanical Engineering,Texas A&M University	Linear cascade	low-speed	low-speed
7	Zhang, Luzeng J., and Ruchira Sharma Jaiswal. "Turbine nozzle endwall film cooling study using pressure-sensitive paint." J. Turbomach. 123.4 (2001): 730-738.	Endwall surface film cooling effectiveness	Solar Turbine Inc., San Diego, CA (US)	high-speed warm cascade	2	/
8	Hilfer, M., Dufhaus, S., Yorita, D., Klein, C., & Petersen, A. (2017). Application of pressure and temperature sensitive paints on a highly loaded turbine guide vane in a transonic linear cascade.	Shock wave and boundary layer studies	DLR / RWTH Aachen	Transonic linear cascade	0.9 to 1.25	/
9	Schreivogel. "Surface pressure measurements for transition research in supersonic flow." Research Master Report, von Karman Institute for Fluid Dynamics, Belgium. 2011.	laminar-turbulent transition (lifetime method)	VKI	Flat plate in wind tunnel	high-speed	high-speed

Figure D.1: Literature setup analysis (a)

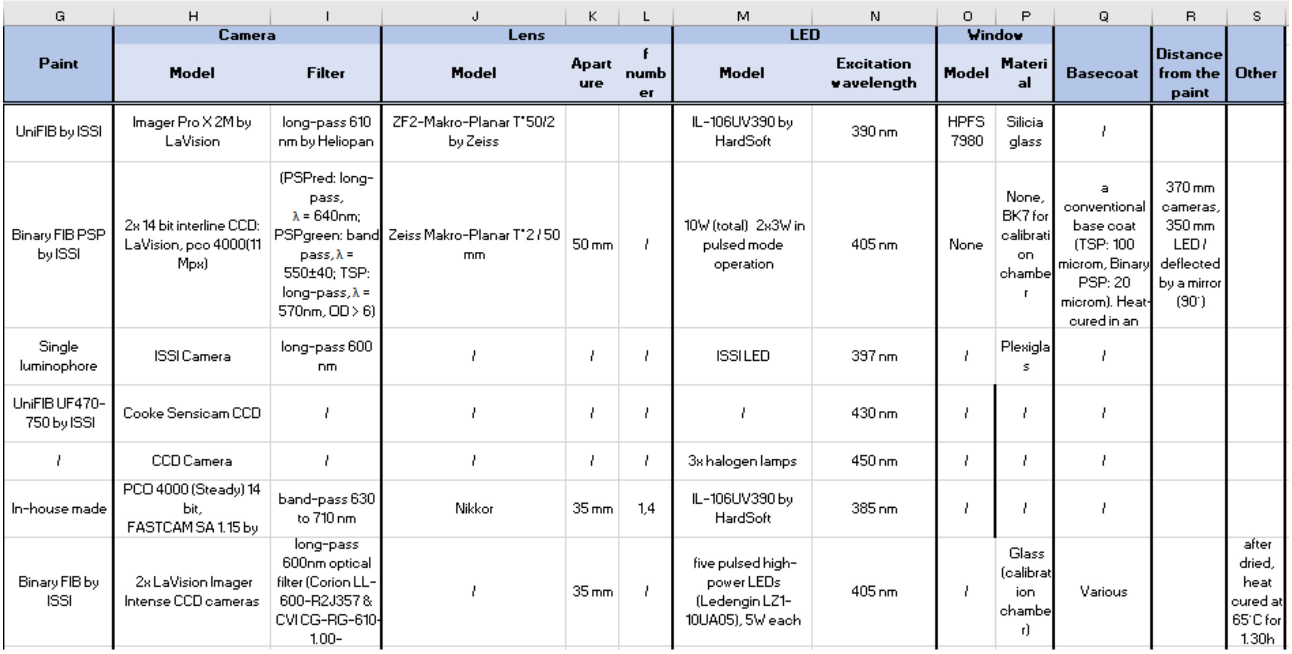

G	H	I	J	K	L	M	N	O	P	Q	R	S
Paint	**Camera**		**Lens**			**LED**		**Window**		**Basecoat**	**Distance from the paint**	**Other**
	Model	**Filter**	**Model**	**Aparture**	**f number**	**Model**	**Excitation wavelength**	**Model**	**Material**			
UniFIB by ISSI	Imager Pro X 2M by LaVision	long-pass 610 nm by Heliopan	ZF2-Makro-Planar T*50/2 by Zeiss			IL-106UV390 by HardSoft	390 nm	HPFS 7980	Silicia glass	/		
Binary FIB PSP by ISSI	2x 14 bit interline CCD: LaVision, pco 4000(11 Mpx)	(PSPred: long-pass, λ = 640nm; PSPgreen: band pass, λ = 550±40; TSP: long-pass, λ = 570nm, OD > 6)	Zeiss Makro-Planar T*2 / 50 mm	50 mm	/	10W (total) 2x3W in pulsed mode operation	405 nm	None	None, BK7 for calibration chamber	a conventional base coat (TSP: 100 microm, Binary PSP: 20 microm). Heat-cured in an	370 mm cameras, 350 mm LED / deflected by a mirror (90°)	
Single luminophore	ISSI Camera	long-pass 600 nm	/	/	/	ISSI LED	397 nm	/	Plexiglas	/		
UniFIB UF470-750 by ISSI	Cooke Sensicam CCD	/	/	/	/	/	430 nm	/	/	/		
/	CCD Camera	/	/	/	/	3x halogen lamps	450 nm	/	/	/		
In-house made	PCO 4000 (Steady) 14 bit, FASTCAM SA 1.15 by	band-pass 630 to 710 nm	Nikkor	35 mm	1,4	IL-106UV390 by HardSoft	385 nm	/	/	/		
Binary FIB by ISSI	2x LaVision Imager Intense CCD cameras	long-pass 600nm optical filter (Corion LL-600-R2J357 & CVI CG-RG-610-1.00-	/	35 mm	/	five pulsed high-power LEDs (Ledengin LZ1-10UA05), 5W each	405 nm	/	Glass (calibration chamber)	Various		after dried, heat cured at 65°C for 1.30h

Figure D.2: Literature setup analysis (b)

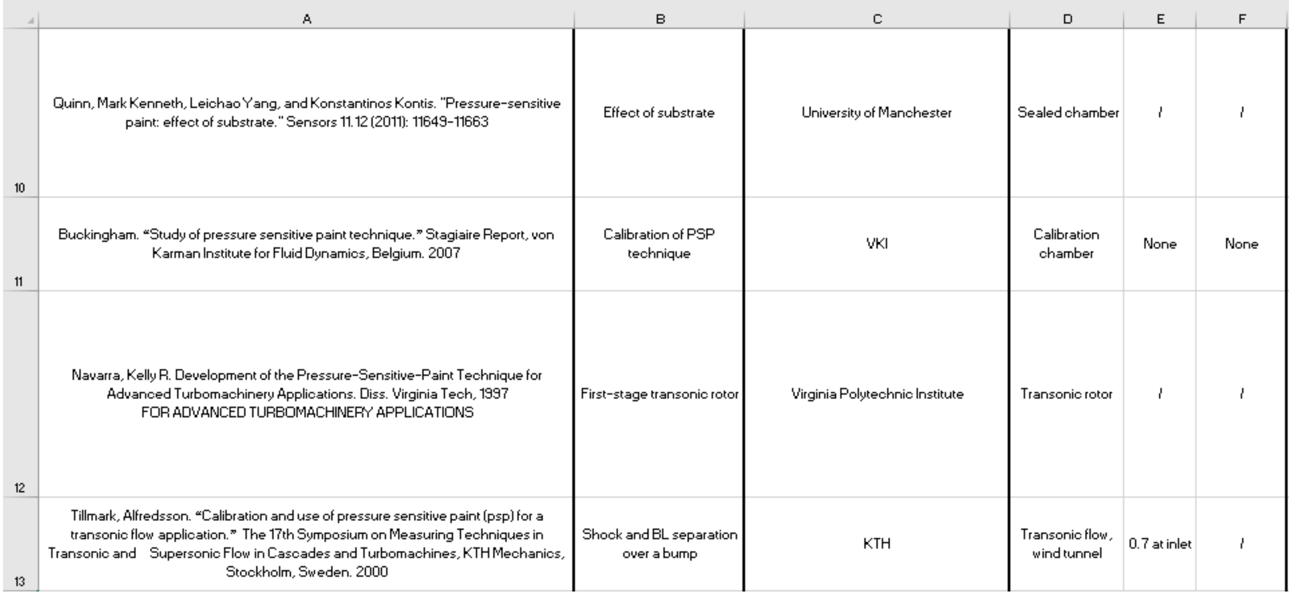

	A	B	C	D	E	F
10	Quinn, Mark Kenneth, Leichao Yang, and Konstantinos Kontis. "Pressure-sensitive paint: effect of substrate." Sensors 11.12 (2011): 11649-11663	Effect of substrate	University of Manchester	Sealed chamber	/	/
11	Buckingham. "Study of pressure sensitive paint technique." Stagiaire Report, von Karman Institute for Fluid Dynamics, Belgium. 2007	Calibration of PSP technique	VKI	Calibration chamber	None	None
12	Navarra, Kelly R. Development of the Pressure-Sensitive-Paint Technique for Advanced Turbomachinery Applications. Diss. Virginia Tech, 1997 FOR ADVANCED TURBOMACHINERY APPLICATIONS	First-stage transonic rotor	Virginia Polytechnic Institute	Transonic rotor	/	/
13	Tillmark, Alfredsson. "Calibration and use of pressure sensitive paint (psp) for a transonic flow application." The 17th Symposium on Measuring Techniques in Transonic and Supersonic Flow in Cascades and Turbomachines, KTH Mechanics, Stockholm, Sweden. 2000	Shock and BL separation over a bump	KTH	Transonic flow, wind tunnel	0.7 at inlet	/

Figure D.3: Literature setup analysis (c)

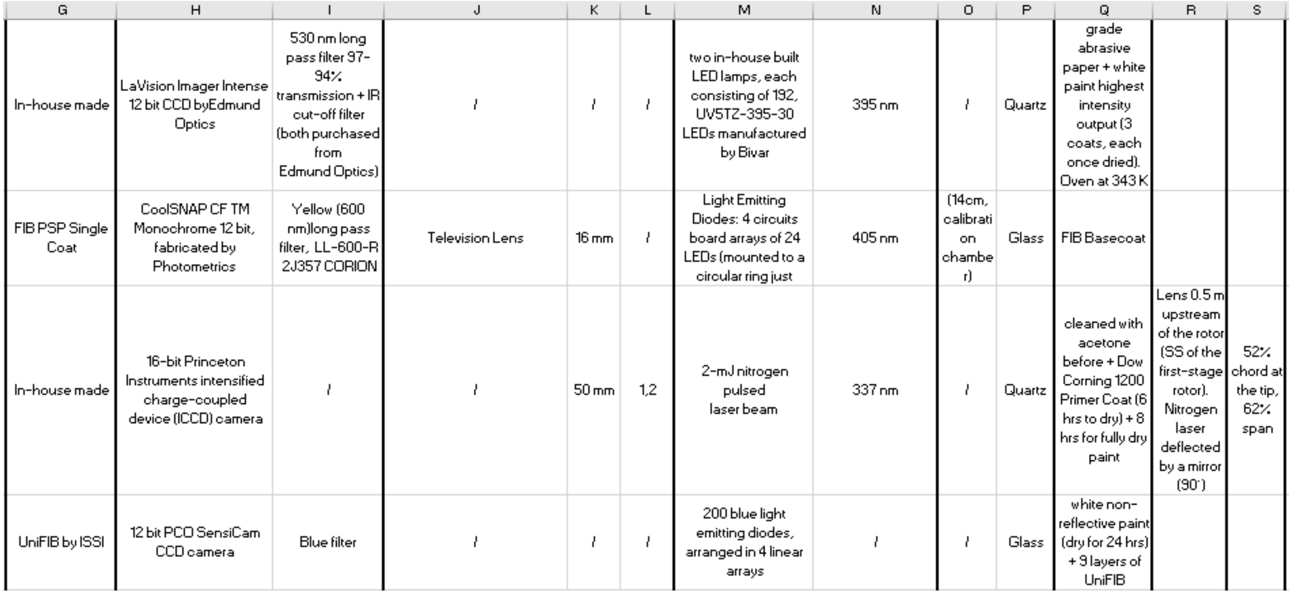

G	H	I	J	K	L	M	N	O	P	Q	R	S
In-house made	LaVision Imager Intense 12 bit CCD byEdmund Optics	530 nm long pass filter 97-94% transmission + IR cut-off filter (both purchased from Edmund Optics)	/	/	/	two in-house built LED lamps, each consisting of 192, UV5TZ-395-30 LEDs manufactured by Bivar	395 nm	/	Quartz	grade abrasive paper + white paint highest intensity output (3 coats, each once dried). Oven at 343 K		
FIB PSP Single Coat	CoolSNAP CF TM Monochrome 12 bit, fabricated by Photometrics	Yellow (600 nm)long pass filter, LL-600-R 2J357 CORION	Television Lens	16 mm	/	Light Emitting Diodes: 4 circuits board arrays of 24 LEDs (mounted to a circular ring just	405 nm	(14cm, calibration chamber)	Glass	FIB Basecoat		
In-house made	16-bit Princeton Instruments intensified charge-coupled device (ICCD) camera	/	/	50 mm	1,2	2-mJ nitrogen pulsed laser beam	337 nm	/	Quartz	cleaned with acetone before + Dow Corning 1200 Primer Coat (6 hrs to dry) + 8 hrs for fully dry paint	Lens 0.5 m upstream of the rotor (SS of the first-stage rotor). Nitrogen laser deflected by a mirror (90°)	52% chord at the tip, 62% span
UniFIB by ISSI	12 bit PCO SensiCam CCD camera	Blue filter	/	/	/	200 blue light emitting diodes, arranged in 4 linear arrays	/	/	Glass	white non-reflective paint (dry for 24 hrs) + 9 layers of UniFIB		

Figure D.4: Literature setup analysis (d)

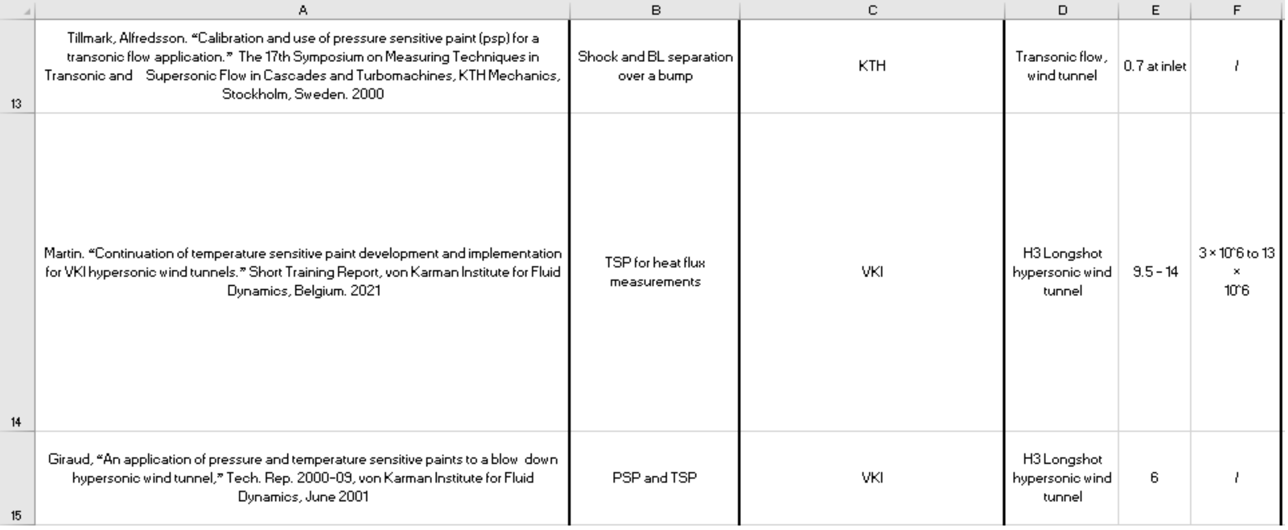

	A	B	C	D	E	F
13	Tillmark, Alfredsson. "Calibration and use of pressure sensitive paint (psp) for a transonic flow application." The 17th Symposium on Measuring Techniques in Transonic and Supersonic Flow in Cascades and Turbomachines, KTH Mechanics, Stockholm, Sweden. 2000	Shock and BL separation over a bump	KTH	Transonic flow, wind tunnel	0.7 at inlet	/
14	Martin. "Continuation of temperature sensitive paint development and implementation for VKI hypersonic wind tunnels." Short Training Report, von Karman Institute for Fluid Dynamics, Belgium. 2021	TSP for heat flux measurements	VKI	H3 Longshot hypersonic wind tunnel	9.5 - 14	3 × 10^6 to 13 × 10^6
15	Giraud, "An application of pressure and temperature sensitive paints to a blow down hypersonic wind tunnel," Tech. Rep. 2000-09, von Karman Institute for Fluid Dynamics, June 2001	PSP and TSP	VKI	H3 Longshot hypersonic wind tunnel	6	/

Figure D.5: Literature setup analysis (e)

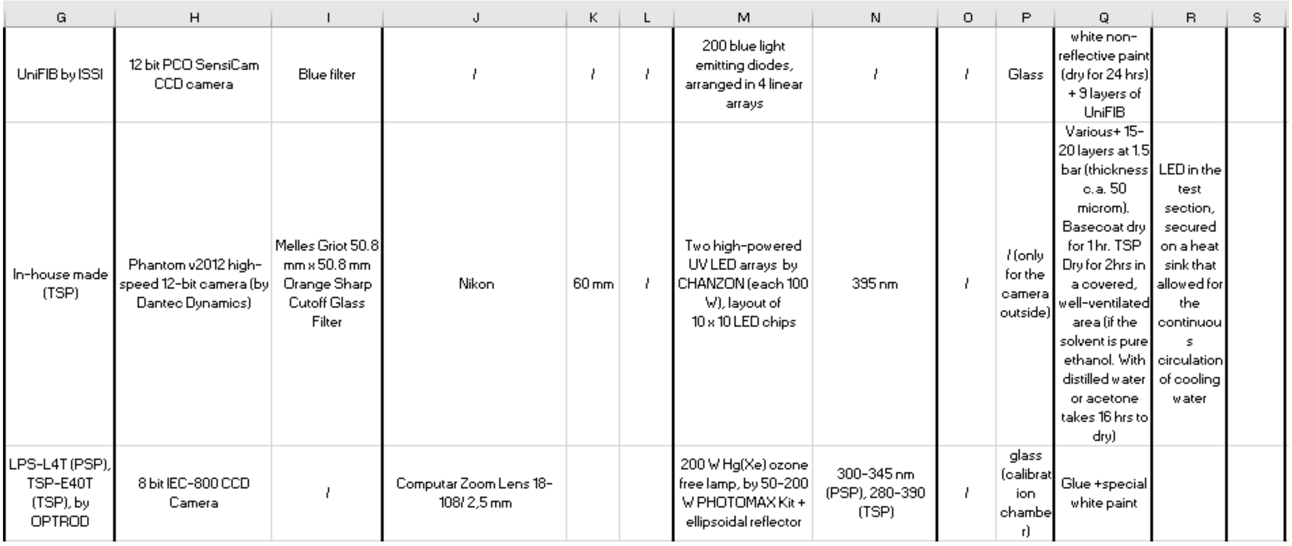

G	H	I	J	K	L	M	N	O	P	Q	R	S
UniFIB by ISSI	12 bit PCO SensiCam CCD camera	Blue filter	/	/	/	200 blue light emitting diodes, arranged in 4 linear arrays	/	/	Glass	white non-reflective paint (dry for 24 hrs) + 9 layers of UniFIB		
In-house made (TSP)	Phantom v2012 high-speed 12-bit camera (by Dantec Dynamics)	Melles Griot 50.8 mm x 50.8 mm Orange Sharp Cutoff Glass Filter	Nikon	60 mm	/	Two high-powered UV LED arrays by CHANZON (each 100 W), layout of 10 x 10 LED chips	395 nm	/	/ (only for the camera outside)	Various+ 15-20 layers at 1.5 bar (thickness c.a. 50 microm). Basecoat dry for 1 hr. TSP Dry for 2hrs in a covered, well-ventilated area (if the solvent is pure ethanol. With distilled water or acetone takes 16 hrs to dry)	LED in the test section, secured on a heat sink that allowed for the continuous circulation of cooling water	
LPS-L4T (PSP), TSP-E40T (TSP), by OPTROD	8 bit IEC-800 CCD Camera	/	Computar Zoom Lens 18-108/ 2,5 mm			200 W Hg(Xe) ozone free lamp, by 50-200 W PHOTOMAX Kit + ellipsoidal reflector	300-345 nm (PSP), 280-390 (TSP)	/	glass (calibration chamber)	Glue +special white paint		

Figure D.6: Literature setup analysis (f)

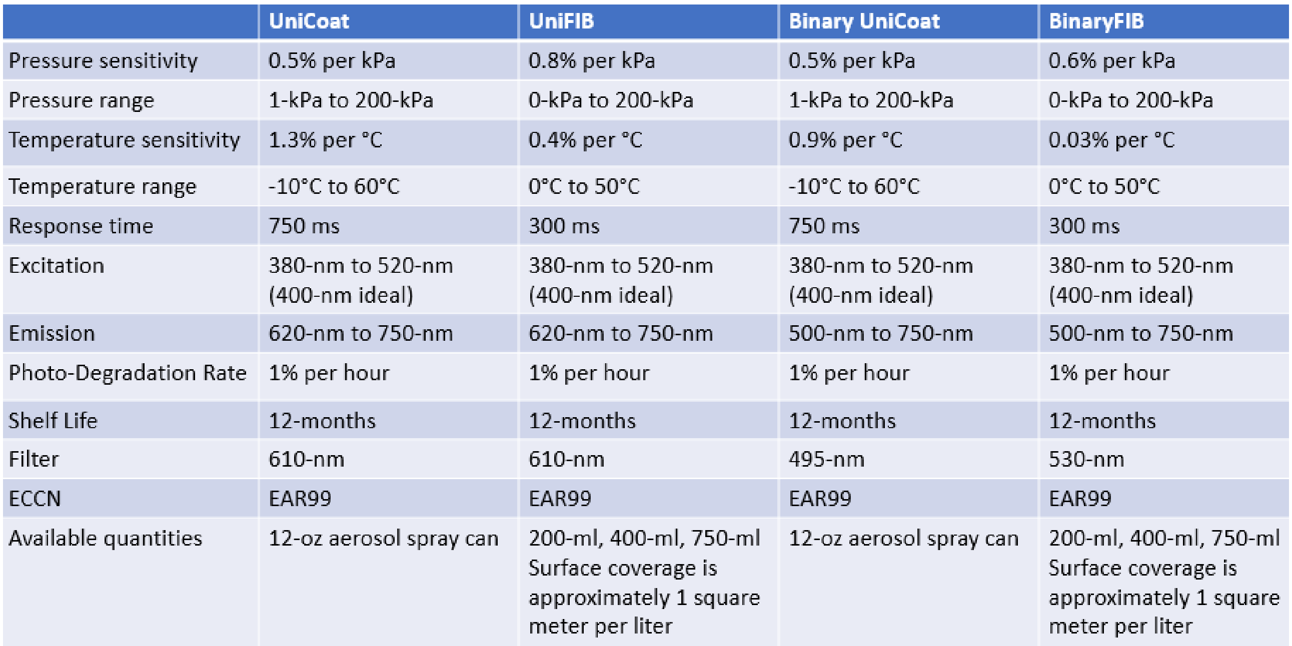

	UniCoat	UniFIB	Binary UniCoat	BinaryFIB
Pressure sensitivity	0.5% per kPa	0.8% per kPa	0.5% per kPa	0.6% per kPa
Pressure range	1-kPa to 200-kPa	0-kPa to 200-kPa	1-kPa to 200-kPa	0-kPa to 200-kPa
Temperature sensitivity	1.3% per °C	0.4% per °C	0.9% per °C	0.03% per °C
Temperature range	-10°C to 60°C	0°C to 50°C	-10°C to 60°C	0°C to 50°C
Response time	750 ms	300 ms	750 ms	300 ms
Excitation	380-nm to 520-nm (400-nm ideal)	380-nm to 520-nm (400-nm ideal)	380-nm to 520-nm (400-nm ideal)	380-nm to 520-nm (400-nm ideal)
Emission	620-nm to 750-nm	620-nm to 750-nm	500-nm to 750-nm	500-nm to 750-nm
Photo-Degradation Rate	1% per hour	1% per hour	1% per hour	1% per hour
Shelf Life	12-months	12-months	12-months	12-months
Filter	610-nm	610-nm	495-nm	530-nm
ECCN	EAR99	EAR99	EAR99	EAR99
Available quantities	12-oz aerosol spray can	200-ml, 400-ml, 750-ml Surface coverage is approximately 1 square meter per liter	12-oz aerosol spray can	200-ml, 400-ml, 750-ml Surface coverage is approximately 1 square meter per liter

Figure D.7: Comparison of technical specifications of four PSPs commercialized by ISSI (a)

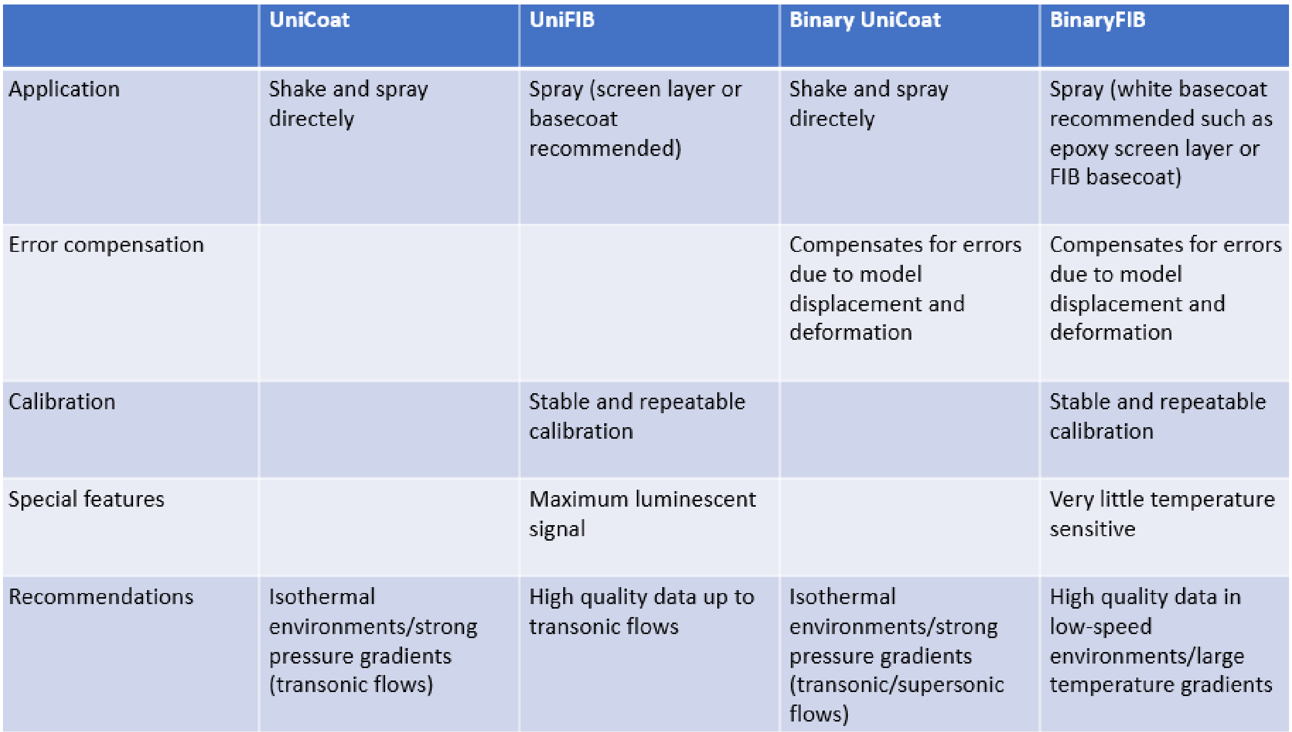

	UniCoat	UniFIB	Binary UniCoat	BinaryFIB
Application	Shake and spray directely	Spray (screen layer or basecoat recommended)	Shake and spray directely	Spray (white basecoat recommended such as epoxy screen layer or FIB basecoat)
Error compensation			Compensates for errors due to model displacement and deformation	Compensates for errors due to model displacement and deformation
Calibration		Stable and repeatable calibration		Stable and repeatable calibration
Special features		Maximum luminescent signal		Very little temperature sensitive
Recommendations	Isothermal environments/strong pressure gradients (transonic flows)	High quality data up to transonic flows	Isothermal environments/strong pressure gradients (transonic/supersonic flows)	High quality data in low-speed environments/large temperature gradients

Figure D.8: Comparison of technical specifications of four PSPs commercialized by ISSI (b)

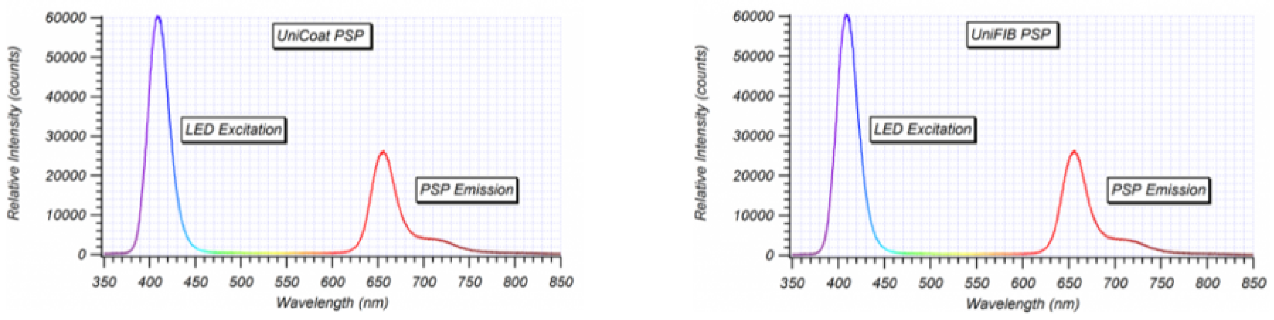

Emission spectra of UniCoat PSP Excited using LM2X-DM-400 LED

Emission spectra of UniFIB® PSP Excited using LM2X-DM-400 LED

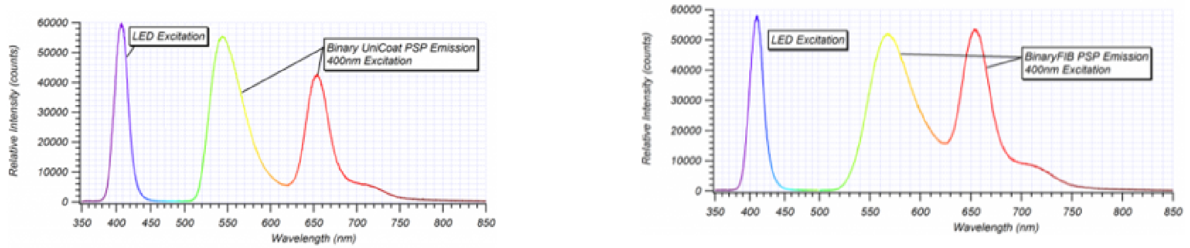

Scaled Emission Spectra of Binary UniCoat PSP Excited using LM2X-DM-400 LED

Scaled Emission Spectra of BinaryFIB® PSP Excited using LM2X-DM-400 LED

Figure D.9: Comparison of emission spectra of four PSPs commercialized by ISSI

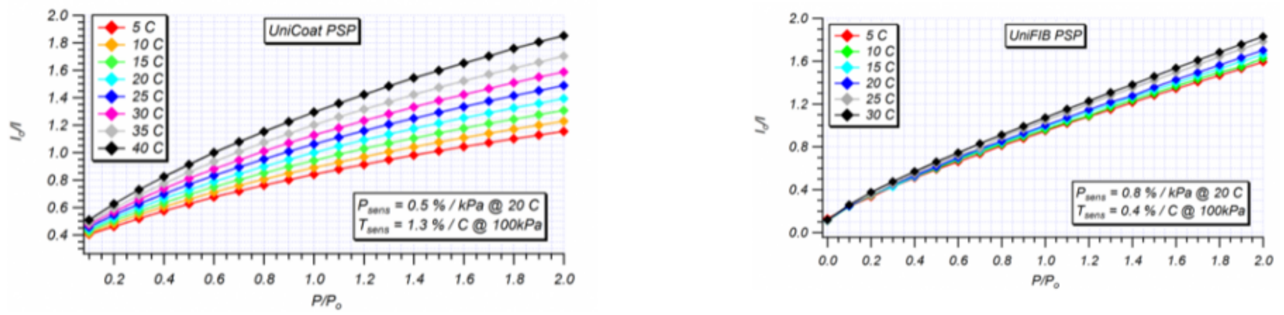

Calibration of UniCoat PSP

Calibration of UniFIB® PSP

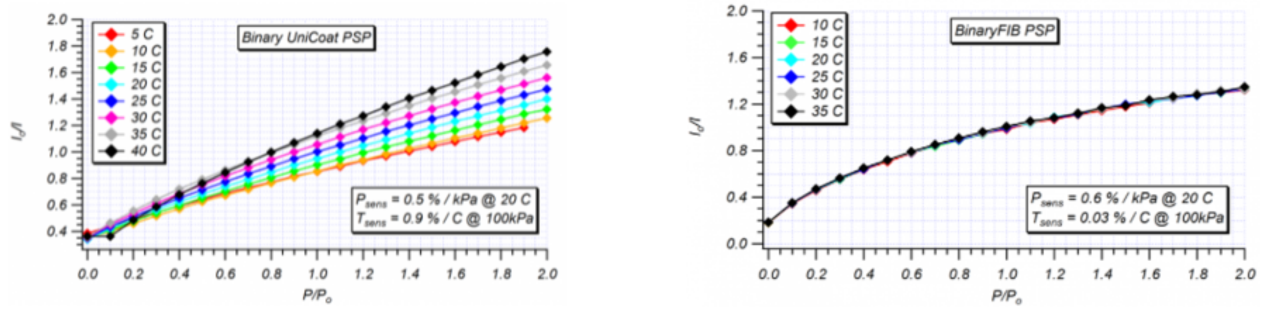

Calibration of Binary UniCoat PSP

Calibration of BinaryFIB® PSP

Figure D.10: Comparison of calibration curves of four PSPs commercialized by ISSI

Bibliography

[1] A.F.Chen, C.Shiau, and J.Han. "Turbine Blade Platform Film Cooling With Simulated Swirl Purge Flow and Slashface Leakage Conditions". In: *Journal of Turbomachinery* (2016). Vol. 139 / 031012-1. DOI: `10.1115/1.4034985`.

[2] C.Martin. *Continuation of temperature sensitive paint development and implementation for VKI hypersonic wind tunnels*. von Karman Institute for Fluid Dynamics, 2020.

[3] C.Martin. *Temperature sensitive paint development and implementation for VKI hypersonic wind tunnels*. von Karman Institute for Fluid Dynamics, 2019.

[4] D.Munday. *Investigation of pressure sensitive paint for high-speed applications*. von Karman Institute for Fluid Dynamics, 2003.

[5] von Karman Institute for Fluid Dynamics. *Continuous High Speed Cascade Wind Tunnel S-1*. URL: `https://www.vki.ac.be/index.php/research-consulting-mainmenu-107/facilities-other-menu-148/high-speed-wt-other-menu-158/66-continuous-high-speed-cascade-wind-tunnel-s-1`.

[6] von Karman Institute for Fluid Dynamics et al. *SPLEEN - Secondary and Leakage Flow Effects in High-SPeed Low-PrEssurE TurbiNes*. 2018. URL: `https://www.h2020-spleen.eu/`.

[7] G.Barigozzi et al. "Assessment of binary PSP technique for film cooling effectiveness measurement on nozzle vane cascade with cutback trailing edge". In: *Experimental Thermal and Fluid Science 97* (2018), pp. 431–443.

[8] G.Lopes et al. "Adaptation of a transonic linear cascade to test purge and sencondary flow effects on the aerodynamics of a high-speed low-pressure turbine". In: *Proceedings of 14th European Conference on Turbomachinery Fluid dynamics Thermodynamics* (2021). DOI: `ETC2021-555`.

[9] H.Kautsky and H.Hirsch. *Detection of minutest amounts of oxygen by extinction of phosphorescence*. 1935, Z Anorg Allg Chem: 222–216.

[10] ISSI. *Innovative Scientific Solutions Incorporated*. URL: `https://innssi.com`.

[11] J.I.Peterson and R.V.Fitzgerald. *New technique of surface flow visualization based on oxygen quenching of fluorescence*. 1980, Rev Sci Instrum 51(5):670–671.

[12] J.Michálek. *Feasibility study of pressure sensitive paint for use in transient facilities*. von Karman Institute for Fluid Dynamics, 2007.

[13] J.W.Gregory et al. “Fast Pressure-Sensitive Paint for Flow and Acoustic Diagnostics”. In: *The Annual Review of Fluid Mechanics* (2014), 46:303–30. DOI: `10.1146/annurev-fluid-010313-141304`.

[14] K.R.Navarra. *Development of the Pressure-Sensitive-Paint Technique for Advanced Turbomachinery Applications*. Virginia Polytechnic Institute and State University, 1997.

[15] L.J.Zhang and R.S.Jaiswal. “Turbine Nozzle Endwall Film Cooling Study Using Pressure-Sensitive Paint”. In: *Journal of Turbomachinery* (2001). Vol. 123 Õ 731. DOI: `10.1115/1.1400113`.

[16] M.Bitter. “Characterization of a turbulent separating/ reattaching flow using optical pressure and velocity measurements”. In: (2014). Genehmigte Dissertation.

[17] M.Bitter, C.J.kähler J.Kurz, and R.Niehuis. “Investigation of a low pressure turbine blade by means of simultaneous optical velocity and pressure measeurements”. In: *18th International Symposium on the Application of Laser and Imaging Techniques to Fluid Mechanics* (2016).

[18] M.Bitter, S.Stotz, and R.Niehuis. “On high-resolution pressure amplitude and phase measurements comparing fast-response pressure transducer and unsteady pressure-sensitive paint”. In: *Proceedings of ASME Turbo Expo 2020 Turbomachinery Technical Conference and Exposition* (2020). DOI: `GT2020-16194`.

[19] M.Hilfer et al. “Application of pressure- and temperature- sensitive paint on a highly loaded turbine guide vane in a transonic linear cascade”. In: *Proceedings of the 1st Global Power and Propulsion Forum GPPF* (2017). DOI: `GPPF-2017-47`.

[20] M.K.Quinn. “Binary pressure-sensitive paint measurements using miniaturised, colour, machine vision cameras”. In: *Measurement Science and Technology 29.5* (2018). DOI: `055107`.

[21] M.K.Quinn, L.Yang, and K.Kontis. “Pressure-Sensitive Paint: Effect of Substrate”. In: *Sensors* (2011). 11, 11649-11663. DOI: `10.3390/s111211649`.

[22] M.Wilhelm and H.Schiffer. “Experimental Investigation of Rotor Tip Film Cooling at an Axial Turbine with Swirling Inflow Using Pressure Sensitive Paint”. In: *International Journal of Turbomachinery Propulsion and Power* (2019). Proceedings of the European Turbomachinery Conference.

[23] N.Tillmark and P.H.Alfreddson. “Calibration and use of pressure sensitive paint (PSP) for a transonic flow application”. In: *The 17th Symposium on Measuring Techniques in Transonic and Supersonic Flow in Cascades and Turbomachines* (2000).

[24] N.Zerelli. *Layout and design of the optical system for pressure sensitive paint measurements in CT-3 & PSP property study*. von Karman Institute for Fluid Dynamics, 2007.

[25] P.Giraud. *An application of pressure and temperature paints to a blowdown hypersonic wind tunnel*. von Karman Institute for Fluid Dynamics, 2000.

[26] P.Schreivogel. *Surface pressure measurements for transition research in supersonic flow*. von Karman Institute for Fluid Dynamics, 2011.

[27] S.Buckingham. *Study of pressure sensitive paint technique*. von Karman Institute for Fluid Dynamics, 2006.

[28] S.Li et al. “Turbine Platform Cooling and Blade Suction Surface Phantom Cooling From Simulated Swirl Purge Flow”. In: *Journal of Turbomachinery* (2016). Vol. 138 / 081004-1. DOI: `10.1115/1.4032676`.

[29] T.Bencic. “Experimental Techniques: Optical surface pressure measurements using luminescent coating”. In: NASA Glenn Research Cente, 2007.

[30] T.Liu and J.P.Sullivan. *Pressure and Temperature Sensitive Paints*. Springer-Verlag GmbH, 2004.

[31] V.Ondrus. “Pressure sensitive paints - a chemical point of view”. In: Universitat Hohenheim, 2006.